8-2015

Advances in High-Throughput Analysis: Automated Radiochemical Separations and Nanopillar based Separations and Field Enhanced Spectroscopy

Jennifer Jeanne Charlton
University of Tennessee - Knoxville, jcharlt1@vols.utk.edu

To the Graduate Council:

I am submitting herewith a dissertation written by Jennifer Jeanne Charlton entitled "Advances in High-Throughput Analysis: Automated Radiochemical Separations and Nanopillar based Separations and Field Enhanced Spectroscopy." I have examined the final electronic copy of this dissertation for form and content and recommend that it be accepted in partial fulfillment of the requirements for the degree of Doctor of Philosophy, with a major in Chemistry.

Micheal J. Sepaniak, Major Professor

We have read this dissertation and recommend its acceptance:

Howard L. Hall, James A. Bradshaw, Robert N. Compton, Frank Vogt

Accepted for the Council:
Dixie L. Thompson

Vice Provost and Dean of the Graduate School

(Original signatures are on file with official student records.)

Advances in High-Throughput Analysis: Automated Radiochemical Separations and Nanopillar based Separations and Field Enhanced Spectroscopy

A Dissertation Presented for the
Doctor of Philosophy
Degree
The University of Tennessee, Knoxville

Jennifer Jeanne Charlton
August 2015

DEDICATION

I would like to dedicate this work to my daughters Zoey and Lily, you are both my source of strength and inspiration.

ACKNOWLEDGEMENTS

I would like to acknowledge my graduate research advisor Michael J. Sepaniak, the balance between letting me develop my own path and your gentle guidance and encouragement has been central in my development as a scientist and professional. You are a true professional and gentleman and I aspire to make a fraction of the positive impact that you have made inside and out of the scientific community.

Equally, I would like acknowledge my co-advisor James. A Bradshaw, (who I often refer to as my biggest champion). Through your belief in my abilities you have driven me to become a knowledgeable and skilled chemist and have pushed me to expand my skillset further than even I knew possible. Additionally, you helped to maintain a certain level of humor about my work and life. I will always remember that a chicken is not a bolt.

Additionally, I would like to acknowledge Nick Lavrik for all of your mentoring and collaboration on this work. As well as the entire exceptional staff at The Center for Nanophase Material Sciences without who much of this work would not have been possible. Craig Hanzelka for the time he spent working on sparky with me. Bob Smithwick for his inspired input of many technical areas. Nahla Hatab for being an excellent technical source and a vault of knowledge about previous work within the Sepaniak Research Group. The entire Sepaniak Research Team (Tess, Nichole, Ryan, Daniel, and Racheal) I have learned from each of you and look forward to seeing the development of your careers.

This work is also in memory of Brittany L. Skyberg, who was a bright developing chemist that was lost far too soon.

Finally, I would like to thank all of my chosen family (you know who you are) who stepped in and supported me in too many ways to list. Without you none of this would have been possible. (Cheers!)

ABSTRACT

Often the need to analyze a large number of samples coincide with critical time consternates. At such times, the implementation of high-throughput technologies is paramount. In this work we explore some viable pathways for high-throughput analysis and develop advancements in novel forms of detection of materials that are vital in the environmental, biological as well as national security arenas. Through the use of new protocols with high sensitivity and specificity as well as simplified chemical processing and sample preparation we aim to allow for improved throughput, fieldable detection, and rapid data acquisition of extensive sample sets. The methods developed in this work focus on unique platforms of the collection and analysis and combine them with automation and portability. Foremost, analytes of interest must be selectively isolated and concentrated by chemical and/or mechanical processes. Secondly, spectroscopic and physical properties are exploited and enhanced by employing viable detection platforms. Finally, automation and field portability are implemented through a combination of optimized robotics, minimized chemical preparation and/or unique lab on a chip type platforms. Presented are two sub areas of research. One focuses on the automation of a time consuming solid phase extraction process that is coupled to inductively coupled plasma mass spectrometry increasing sample throughput by orders of magnitude. The second focused on the fabrication and use of silicon nanopillars as a platform for separations and enhanced optical analysis. Each section of work focuses on the development of a practical, accessible, and deployable methods of analysis.

TABLE OF CONTENTS

LIST OF TABLES

LIST OF FIGURES

Nomenclature

APTMS	(3-aminopropyl) trimethoxysilane
BSA	Bovine serum albumin
CCD	Charged coupled device
CMPO	Octylphenyl-N,N-di-isobutyl carbamoylphosphine oxide
cps	Counts per second
d	Diameter
d_p	Particle size
DW	Dewetting
e^-	Electron
EBL	Electron beam lithography
EM	Electromagnetic
ETV	Electrothermal Vaporization
eV	Electron Volt
f	Frequency
FITC	Fluorescein isothiocyanate
g	Surface tension
g	Gap
GA	Glutaraldehyde
GC	Gas Chromotography
h	Viscosity
HBQ	Hydroxybenzo[h]quinolone
HTS	High Throughput Screening
ICP	Inductively Coupled Plasma
K	Kelvin
k	Proportionality consonant
K_0	Permeability constant
kJ/mol	KiloJoule per Mole
LC	Liquid Chromatography
LMR	Leaky mode resonances
LOD	Level of detection
LSPR	Localized plasmon resonance
m/Δm	Mass Resolution
MC	Multi-Collector
mHz	Megahertz
MS	Mass Spectromrtry
NA	Numerical aperture
Pa	Pascal the SI unit of pressure
PECVD	Plasma enhanced chemical vapor deposition
PMMA	Polymethyl methacrylate

PSO	Porous silicon oxide
QE	Quantum efficiency
QMS	Quadrpole Mass Spectrometry
r	Roughness
r_0	Half distance between rods
R6G	Rhodamine 6G
RGB	Red Green Blue
RIE	Reactive ion etching
RSD	Realative Standard Deviation
S	Singlet state
S_0	Ground state
S_1	Excited State
SEM	Scanning electron microscope
si	Surface immobilized
SNR	Signal to noise ratio
SPE	Solid Phase Extraction
t	Time
TBP	Tri-n-butyl phosphate
TE	Transverse electric
TIMS	Thermal ionization mass spectrometry
TLC	Thin-Layer Chromatography
TM	Transverse magnetic
U	Velocity profile
uHTS	Ultra High Throughput Screening
Umean	Mean velocity
V_0	Voltage
WFFM	Wide-field fluorescence microscopy
Z_f	Solvent front mitigation distance
ZMW	Zero mode waveguide
γ	Surface tension
γ_{nr}	Non-radiative decay rate
γ_r	Radiative decay rate
λ	Wavelength
μ	Viscosity
π	Pi
φ_s	Ratio of the area on top of the pillars to area of analysis
Θ	Contact angle

CHAPTER 1:
INTRODUCTION

I have not failed. I've just found 10,000 ways that won't work-Thomas A. Edison

1.1 High throughput analysis

One of the earliest examples of a comprehensive screening of material was conducted by T. Edison and co-workers between 1878 and 1880 where they screen approximately 6000 candidates for the filament to be used in the incandescent bulb.[1] Almost a century later in the 1970's Hanak[2] was the first to highlight the power of a parallel screening method. While the concept of parallel screening was introduced more than 40 years ago, the technology to implement high throughput analysis was years from being developed.[1] In the early 1990's advances in molecular biology, human genetics and functional genomics coupled with a major increases in compound collections produced by combinatorial technologies, fueled an important need for improvements in high-throughput analyses. By the mid 1990's robotics systems were capable of screening thousands of samples a day.[3] This explosion in throughput meant that reagent production had to be increased to meet the challenge. This vast consumption of reagents drove the next wave in high throughput analysis toward minimization. With the decrease in sample and platform sizes methods evolved into ultraHTS (uHTS) methods capable of 100,000 assays per day.[3] This shift from expensive and bulky instruments to miniaturized, low-cost devices allowed a pathway to automated sample processing and high throughput. Today, most pharmaceutical companies use HTS as the primary engine driving lead discovery. Initially the main drive behind increasing throughput for chemical analysis was within the pharmaceutical industries. Increasing throughput for chemical analysis is of great interest and pursued for many endeavors including biochemistry, genetics, drug discovery, proteomics, clinical chemistry and pharmacology. Other

industries soon started to take notice and today google scholar can find more than forty three thousand journal articles related to high-throughput analysis published yearly. The fields range from the biological to elemental and encompass a full gambit of instrumentation and methods.

Within the field of developing high throughput methods the broad areas that are currently being researched can sum it up in three major categories:[3] 1) methods and detection 2) sample handling and robotics 3) Process flow and information management.

In this work we address parts of all three of these categories. Each section of original work introduces the motivation behind the development of either an automated system or a novel nanoscale platform. While the individual chemical motivations may vary the overall goal of developing high-throughput sample handling and analysis systems is congruent throughout.

1.2 Organization

Chapter 2 and 4 of this work introduces basic concepts and background behind the original research presented. Chapter 3, 5, 6, and 7 introduce original research conducted in a collaboration between the University of Tennessee in Knoxville, Y-12 National Security Complex, and The Center for Nanophase Material Sciences.

1.3 References

[1] Potyrailo, R.A. and E.J. Amis, *High-throughput analysis: a tool for combinatorial materials science*. 2012: Springer Science & Business Media.

[2] Hanak, J.J., *The "multiple-sample concept" in materials research: Synthesis, compositional analysis and testing of entire multicomponent systems.* Journal of Materials Science, 1970. **5**(11): p. 964-971.

[3] Hertzberg, R.P. and A.J. Pope, *High-throughput screening: new technology for the 21st century.* Current opinion in chemical biology, 2000. **4**(4): p. 445-451.

CHAPTER 2:
INTRODUCTION TO INDUCTIVELY COUPLED PLASMA MASS SPECTROMENTRY AND SOLID PHASE EXTRACTION

2.1 Mass spectrometry

The unparalleled sensitivity, detection limits, speed, and the diversity of applications has cemented mass spectrometry (MS) as a valuable and widely utilized tool for the qualitative and quantitative analysis of compounds. The mass spectrum of a molecule is produced via a plot of relative ion abundances verses mass to charge ratio. There are a number of different MS instruments commercially available, providing a number of pros and cons for specific applications. During more than 20 years of commercialization, ICP-MS has become the most successful method in many analytical laboratories for the accurate and precise trace element and isotopic determinations in a wide variety of different applications. Generally, the inductively coupled plasma mass spectrometer can be subdivided in the following 5 parts: 1) sample introduction, 2) ion source 3) ion extraction, 4) ion separation, and 5) ion detection.[1]

2.1.1 Sample introduction

Uniform sample introduction is paramount to maintain a stable plasma. Often the liquid sample is introduced as a thermally generated vapor or via a nebulizer as finely divided droplets or micro-particulates that are carried into the plasma by the support gas flowing at a rate of about 1 mL/min.[2] Most samples are introduced into the plasma as a high volume solution which allows for automation and high sample throughput. Due to the continuous nature of the gas flow, ICP is inherently a natural couple to several separation techniques, including GC-ICP-MS and LC-ICP-MS.[3] While most samples are high volume and liquid in nature, techniques have been developed to handle small volume and solid state samples. For example, a flow injection technique is employed to handle

samples with volumes on the order of 100 µL. Electrothermal vaporization (ETV), which vaporizes a sample via flash evaporation from a filament heated by a pulse current, allows for very small volumes in the order of 10 µL or solids to be introduced to the argon flow as a vapor.[2] Additionally, solid samples may also be introduced to the plasma via laser ablation allowing for spatial rendering of a surface composition.[2] Although a variety of sample introduction devices have been coupled to an ICP-MS for gaseous, liquid or solid samples.[1] Generally, liquids are dispersed into fine aerosols using various types of nebulizers and using argon as sample carrier gas at about 1 L/min before being introduced into the ICP. A Peltier cooled, low-volume conical spray chamber fitted with a fixed impact bead and a high performance glass concentric nebulizer (Figure 2.1) is provided to enhance stability and to enable fast washout and minimum cross contamination.[4] The Peltier block is electronically controlled enabling different spray chamber temperatures to be used within an analytical method.

Common sample introduction devices used for ICP are pneumatic nebulizers and ultrasonic nebulizers. Pneumatic nebulizers used in combination with ICPs have two basic configuration, the concentric and crossflow type. In the concentric type the sample solution passes through a capillary surrounded by a high-velocity gas that flows parallel to the capillary axis.[5] The crossflow type nebulizer has a liquid-carrying capillary which is placed orthogonal to the tube carrying the high-velocity gas stream.[6] When working with ICP techniques, the concentric type remains the most commonly used device. [7]

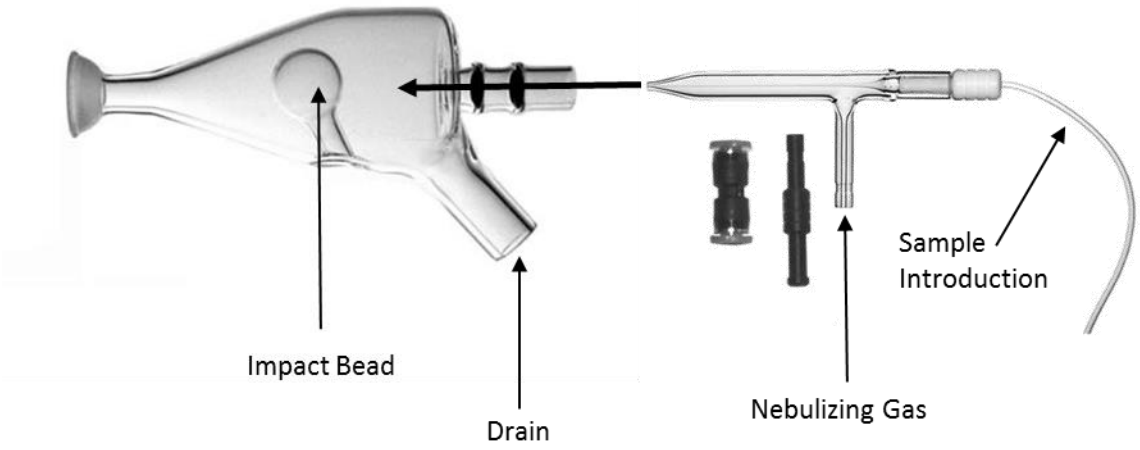

Figure 2.1. A low-volume conical spray chamber fitted with a fixed impact bead and a high performance glass concentric nebulizer.

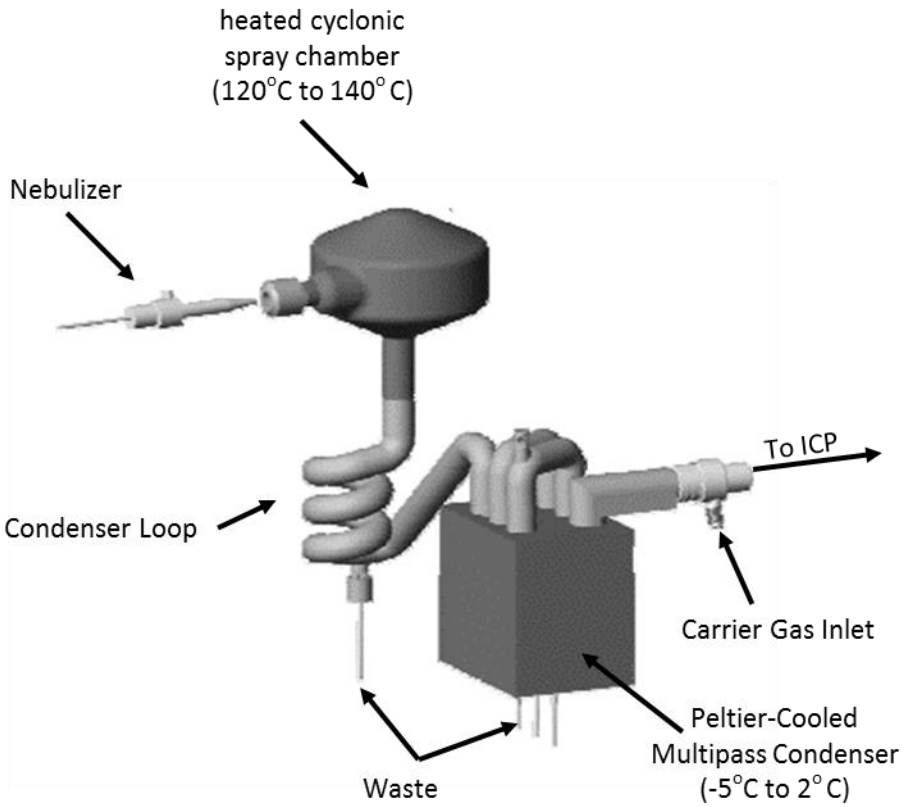

Figure 2.2 Internal sample flow path of the Apex sample inlet system

The generation of fine aerosols is very important as droplets with diameters above 10 μm are not completely vaporized before the plasma analytical sampling zone.[8] The impact bead spray chamber is a small volume unit that assists in aerosol filtering of larger diameter droplets.[9] In addition to an impact bead spray chamber other methods of processing post nebulized samples have been developed. One such system includes the APEX Sample Inlet System (Figure 2.2). The Apex is a fully integrated inlet system that connects directly to the ICP torch injector and incorporates a nebulizer. The Apex improves sensitivity primarily by increasing both sample transport efficiency and the quality of aerosol introduced to the ICP instrument. The sample is aspirated via a nebulizer into a heated cyclonic spray chamber to vaporize the entire sample. The excess solvent aerosol is then condensed out by a Peltier cooled condenser. The dry aerosol containing over 90% of the sample analyte passes to the ICP.[10]

2.1.2 ICP-ion source

In elemental MS the inductively coupled plasma (ICP) ion sources have become the standard. ICP creates a reliable and reproducible method for the production of elemental ions of metals. This is important in the such as geochemistry, environmental analysis, biomedical, and nuclear material analysis and forensics.[11-14]. By virtue of excellent detection limits, multi-element capabilities, and large sample throughput, ICP-MS has superseded previous methods for trace analysis. The ICP torch achieves traditionally difficult to produce elemental metal ions with the use of Argon (Ar) or other suitable pure gasses such as helium or hydrogen used to achieve a stable plasma. As shown in Figure 2.3, the design of the plasma torch consists of concentric quartz tubes with the inner tube

containing the sample aerosol and support gas and the outer tube containing additional support gas flow to cool the tubes. Coupling is achieved via a radiofrequency (RF) generator that is typically capable of generating 1-5 kW at between 27 and 50 MHz thus producing an oscillating current in a cooled induction coil that wraps around the tubes.[15] In turn, the current in the induction coil induces an oscillating magnetic field. The gas flowing through this region is made electrically conductive by introducing a spark from a Tesla coil. The magnetic field is then able to induce an oscillating current in the created ions and electrons of the support gas. The gas that is flowing in a rotationally symmetric fashion will be inductively heated by the oscillating fields of ions inside of the coil. The electrons generated in this field are accelerated perpendicularly to the torch. At high speeds, the mix of cations and electrons (known as eddy current) will collide with additional support gas atoms to produce further ionization that causes a significant temperature increase. Within 2 ms, a steady state of a high electron density plasma in the tip of the torch is achieved. A long, well-defined tail emerges from the top of the plasma source. As shown in Figure 2.3, the temperature within the plasma ranges from 6,000-10,000 K.[15] When introduced, a sample spends several milliseconds in the analytical zone of the plasma. The sample moves through the plasma cone on a current of support gas the high temperatures will effectively desolvate, vaporize, atomize, and ionize the sample leaving ions representing the elemental composition of the sample. The energy available in the argon plasma is approximately 15.8 eV, which is sufficient to ionize most elements on the periodic table as most their first ionization energies in the range of 4 to 12 eV.[15] These energy levels, achieved approximately 12 to 14 mm from the load

coil correspond to a temperature of approximately 7500 K.[16] The plasma acts as a reservoir of energy provided by the rf field that allows for 80 % of analytes (M) to be more than 75 % ionized.[16] Various ionization processes have been suggested resulting from the presence of species that are obtained during the plasma generation. The major species include argon ions (Ar^+), and the electrons (e^-), as well as metastable and excited Ar^m argon atoms. The main ionization processes can be described as:[1]

1. Electron impact ionization

$e^-(fast) + M \rightarrow M^+ + e^-(slow) + e^-(slow)$

2. Penning –ionization

$Ar^m + M \rightarrow M^{+*} + Ar + e-$

3. Charge transfer ionization

$Ar^+ + M \rightarrow M^+ + Ar$

Different ionization energies of atoms may be exploited to improve analytes in comparison to interferences by tuning of the rf-power for preferable ionization of the target analyte. Hence, it is possible to partially separate potential interfering isotopes or molecules. [17]

2.1.3 The interface region

After the sample has been ionized it must be introduced to the mass analyzer. Due to the high thermal energy associated with the ICP plasma the development of an interface region was crucial in the use of an ICP torch as a viable ion source.

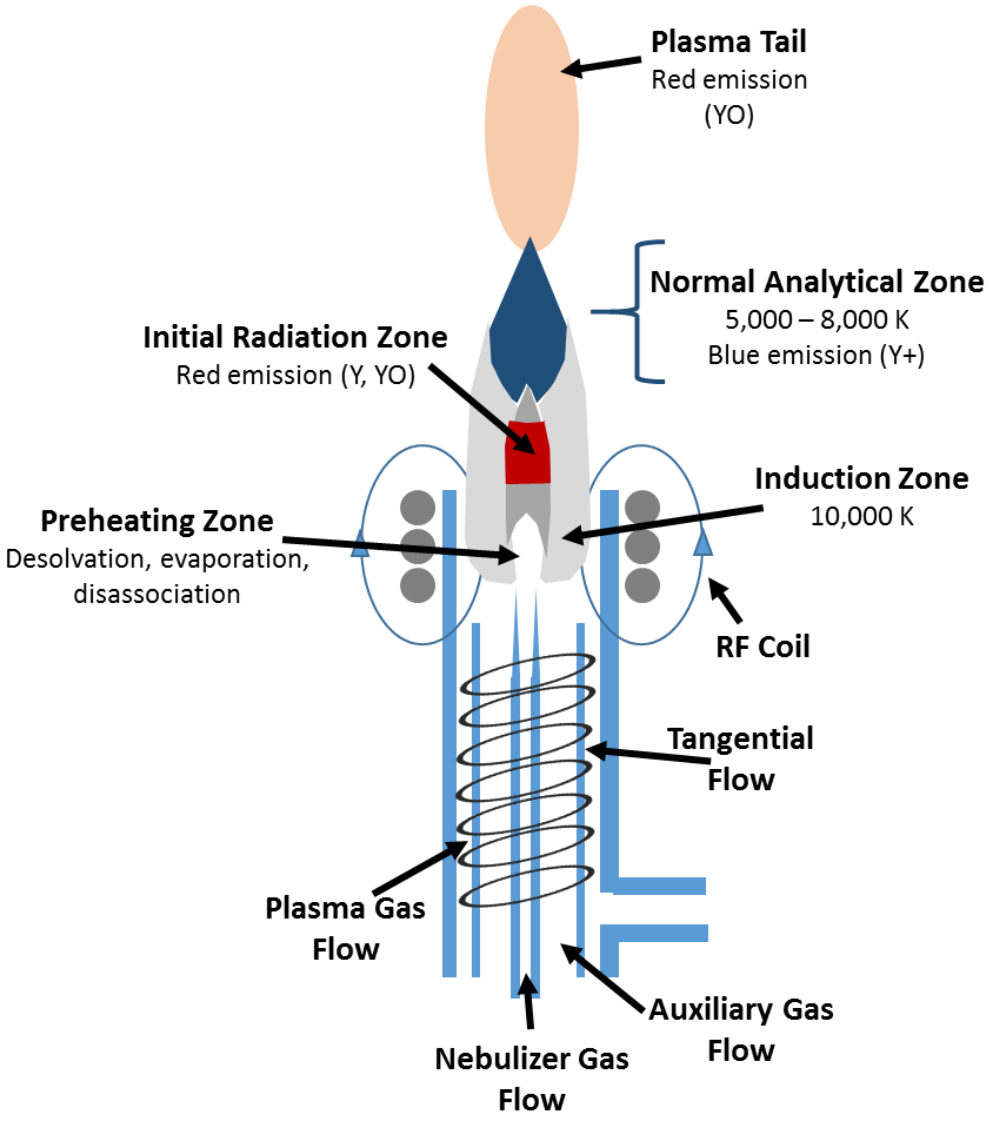

Figure 2.3. ICP Torch Schematic Reproduced showing different plasma zones.

The ions must be extracted from a high temperature, corrosive plasma at atmospheric pressure (760 torr) and focused and guided into a high vacuum chamber (10^{-7} torr) at room temperature. This transfer is accomplish by an interface region that contains two successive nickel cones (shown in Figure 2.4) with millimeter-sized orifices through which the ions in the analytical region of the plasma cone must be sampled. The ions are extracted through the orifice of the first sample cone into a region between the two cones held at a pressure of 1 to 3 torr by a large capacity rotary vacuum pump. This vacuum removes a majority of the excess argon atoms helping to change the ion beam from viscous flow to molecular flow. The ions are then further extracted through the orifice of the second skimmer cone into the front section of the mass spectrometer which is maintained at a pressure between 10^{-4} to 10^{-5} torr. Electrostatic lenses keep the ions focused in a compact "ion beam" as they pass through the vacuum system to the final chamber, where the mass spectrometer (MS) and detector are housed. The ion lenses perform a second, essential function of separating the ions from the residual neutral material, that would otherwise may reach the detector and increase random background noise. [16] The continuous ion beam evolved from the ICP plasma source makes it an ideal choice for scanning type mass analyzers such as a quadrapole or magnetic sector. However orthogonal ion introduction techniques have been used vary successfully to couple the ICP ion source with pulse type analyzers such as time of flight and electronic or magnetic induced orbit analyzers. [2]

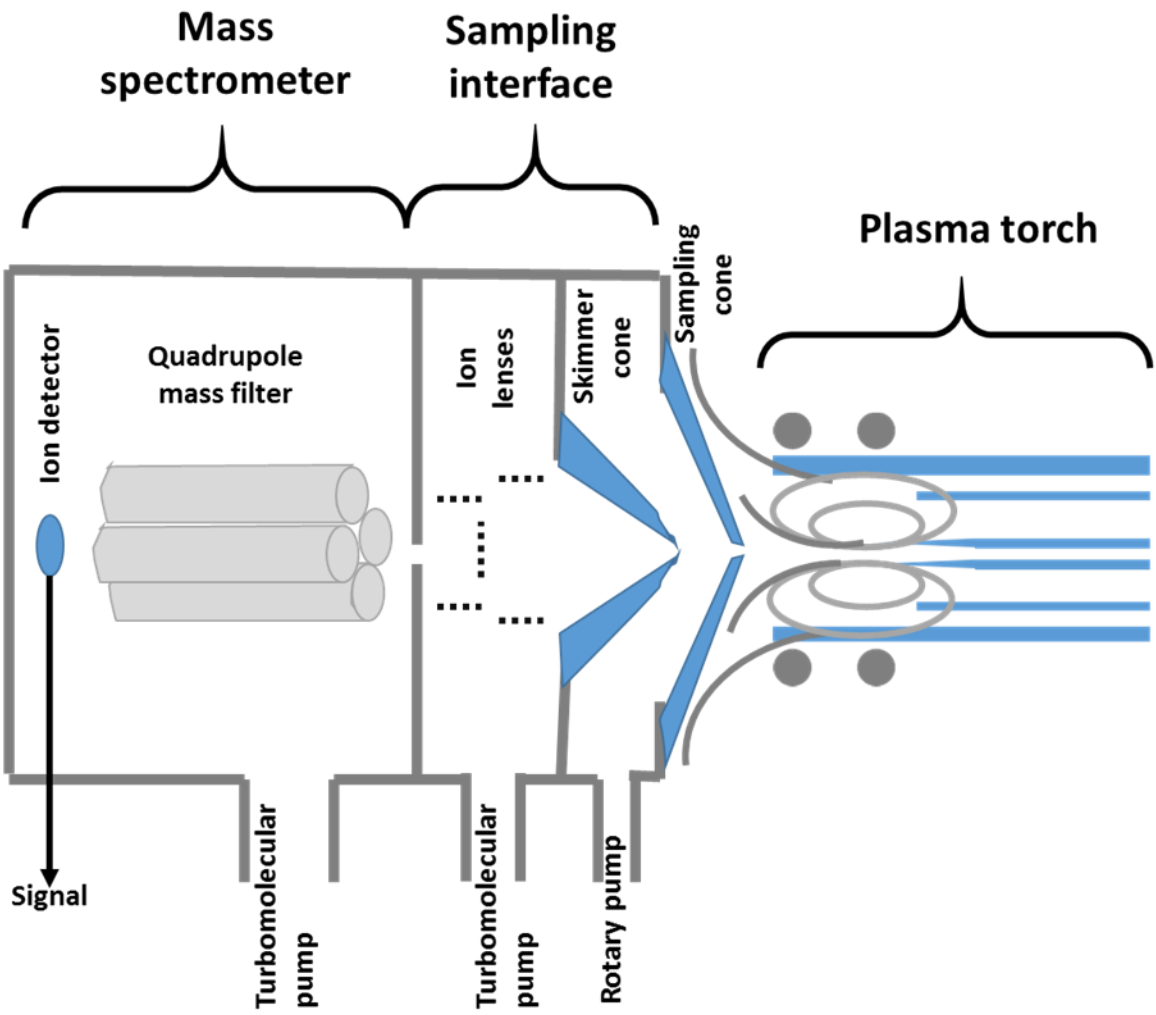

Figure 2.4. Schematic of ICP-MS

2.1.4 Mass analyzers

Ions extracted from the interface region are directed through the ion optics into the mass separation analyzer. The vacuum in this region is maintained at about 10^{-6} Pa. The most common mass separation devices used in ICP instruments are quadrupole, double focusing sector field and time of flight mass spectrometers.[18] Quadrupole analyzers are mainly used in ICP-MS due to the relatively low costs, their simple operation and their relatively fast m/z separation. However, mass peaks in quadrupoles are not flat-top and require stable mass calibration. Small changes in operating conditions can significantly alter the ion transmission into the analyzer and the mass resolution is low in comparison to other configurations (m/Δm = 300). The general layout of the quadrupole mass analyzer is shown in Figure 2.5 The ideal configuration is that the four rods should have a hyperbolic profile to generate most stable electric field distribution. In practice, many systems are manufactured using round rods with an interelectrode spacing to produce the best approximation to the optimum hyperbolic field (Figure 2.5). The potential in a quadrupole field may be expressed in rectangular coordinates by the following equation:[19]

$$\boldsymbol{V = \frac{V_0}{r_0^2}(x^2 - y^2)} \qquad \text{Eq. 2. 1}$$

where V_0 is the voltage applied to each rod, and the parameter r_0 is half the distance between opposite rods. The electric field components in the x, y and z directions are:[1]

$$E_x = -\frac{dV}{dx} = -\frac{2V_0 x}{r_0^2} \quad \textbf{Eq. 2. 2}$$

$$E_y = -\frac{dV}{dy} = -\frac{2V_0 y}{r_0^2} \quad \textbf{Eq. 2. 3}$$

$$E_z = -\frac{dV}{dx} = 0 \quad \textbf{Eq. 2. 4}$$

In the static case, the equation of motion in the x and y directions becomes:

$$\frac{d^2x}{dt^2} = -(\frac{2V_0 x}{r_0^2})(\frac{e}{m}) \quad \textbf{Eq. 2. 5}$$

$$\frac{d^2y}{dt^2} = -(\frac{2V_0 y}{r_0^2})(\frac{e}{m}) \quad \textbf{Eq. 2. 6}$$

where e and m refer to the magnitude of charge and ion mass, respectively. The solution of equation 2.5 yields a sinusoidal oscillation in the x-z plane, while the solution of equation 2.6 provides an exponentially increasing trajectory in the y-z plane.[1] The mass to charge ratio (m/e) corresponding to the tip of the stability region is given by:[19]

$$\frac{m}{e} = \frac{0.1435V}{f^2 r_0^2} \quad \textbf{Eq. 2. 7}$$

where m/e, atomic mass units, V, volts; r_0, centimeters; and f (frequency) megahertz. When scanning through frequencies ions on the correct charge to mass ratio pass through the quadrupole while all other ions are sent on a trajectory off of the focal path.

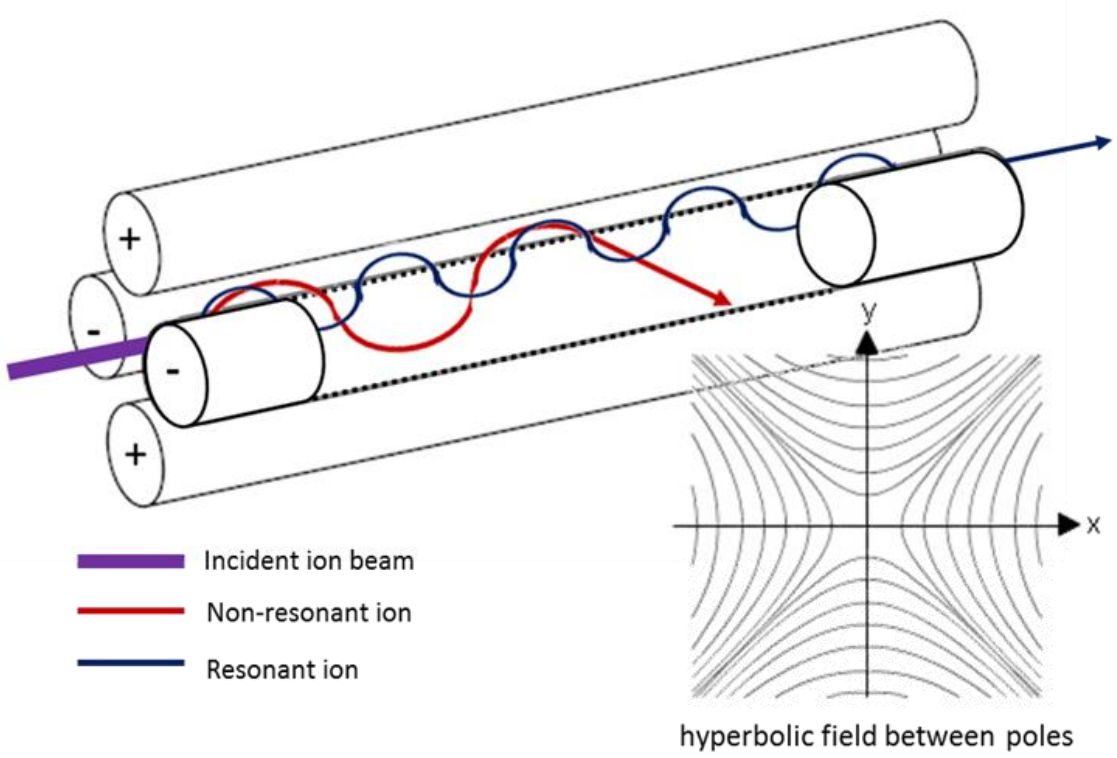

Figure 2.5. Schematic of the quadrupole mass analyzer with cylindrical rods and associated hyberbolic field.

2.1.5 Ion detection

The ion beam separated by the mass analyzer is converted to electrical signal using various detectors. The order of magnitude of the signal detectable is in the range from 0.1 ion/s to 1011 ions/s. For low signal ranges (< 106 ions/s), the ion-counting mode is used, while for higher signals the detector is operated in analogue mode. Some of the common ion detectors include a Faraday cup and the electron multiplier.

The Faraday Cup detector is stable and robust in operation and can be used to screen unknown samples that may contain high concentrations of elements. The ion beam is directed into a Faraday collector coupled to a true dc amplifier system. This device can be used to directly measure currents down to 10-15 A (corresponding to about 104 ions/s). The absolute operating range of the amplifier may be varied by changing the value of the feedback resistor, and the output can be transformed into a series of pulses, which can be handled by the data system using a voltage-to-frequency converter.[1]

The most commonly used ion detectors are in ICP-MS are the discrete or the continuous dynode electron multipliers. A typical discrete-dynode electron multiplier has between 12 and 24 dynodes along the length of the detector and is used with an operating gain of between 10^4 and $10^{8.}$.[16] The principle of the detectors is based on a system where by when the ions emerge from the mass separation system, they impinge on the first dynode and are converted into electrons. As the electrons are attracted to the next dynode, electron multiplication takes place, which results in a very high number of electrons emerging from the final dynode. This electronic signal is then converted by the data processing system in the conventional way and the readout is in counts/second (or cps).

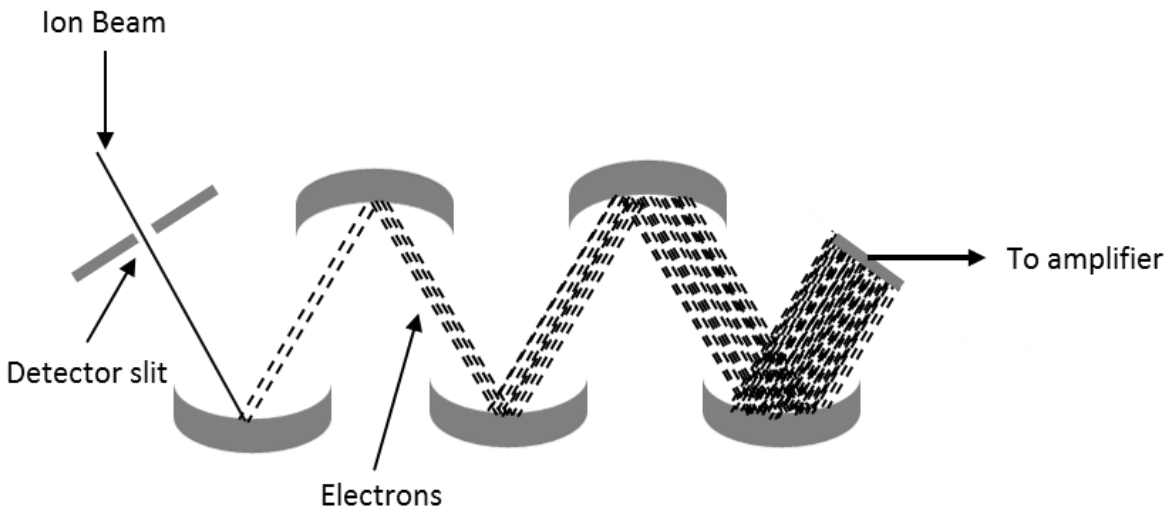

Figure 2.6. Discrete dynode electron multiplier.

Table 2.1 LOD of different ICP-MS techniques for determination of long-lived radionuclides.

Analytical Method	Detection Limit
ICP-MS (ng/l)	
Quadrupole ICP-MS	0.01-0.6
ICP-SFMS	0.00004-0.005
ICP-QMS with collision cell	0.003-0.01
ICP-TOFMS	0.1-1
MC-ICP-MS (sector field)	0.0001-0.0002

These cps are directly proportional to concentrations and can be converted into analyte concentrations using comparative measurements of calibration standards. Most detection systems have a dynamic range of up to 6 orders of magnitude in ion counting mode and up to 5 orders of magnitude by combination of ion counting with analog mode (i.e. the measurement of electric current on one of the intermediate dynodes).

2.1.6 Capability of quadrupole ICP-MS for analysis of radionuclides

When compared with optical techniques of elemental analysis, the increase in sensitivity and dynamic range are orders of magnitude better. The detection limit (Table 2.1) of a typical ICP-MS with a quadrapole mass analyzer reaches into the part-per-billion range for most elements and as low as part-per-trillion levels for many elements. When an ICP ion source is coupled with a high resolution electrostatic analyzer, the levels of detection can reach down to the part-per-quadrillion level for many elements.[11] These low levels of detection make ICP-MS a valuable tool in trace elemental analysis. ICP-MS has become a well-established analytical technique for the determination of long-lived radionuclides providing high sensitivity, low background resulting in low LOD's, good precision and accuracy for isotope and isotope ratio measurements with relatively simple sample preparation procedures.[20-23].

While there are many advantageous features of using ICP-MS the one major disadvantage is isobaric interferences with other elements or molecular ions. While the quadrupole mass analyzers have been used as standard ion separation tools in ICP-MS because of their linear dynamic range, robustness and relatively low costs, the quadrupole-based ICP-MS provide a resolution power of approximately 300, which is

insufficient to deal with some of the inevitable isobaric interferences. Advanced ICP-MS techniques provide useful features to solve these inherent interference problems. In many cases, molecular interferences can be resolved from the isotope of interest using double-focusing sector field ICP-MS by using higher mass resolution (>3000). Their increasing availability is now allowing to determine rapidly long-lived radionuclides in environmental samples.[24, 25] Matrix considerations must be taken into account when selecting the isotopes, particularly from mono-isotopic analysis. Matrix based interferences are usually oxides, peaks that occur sixteen mass unites form the major element in the sample. These effects occur to varying extents, and generally the problem increases with the boiling point of the matrix oxide. These oxides may be minimized through several tuning methods, with the position of the torch and the nebulizer gas flow having the greatest effects. Since many of these oxide species occur as a constant background, their contribution may be blank subtracted. However, this persistence background interference renders it impossible to determine elements at ultra-trace levels (low ppt). In addition to oxide formation other matrix components must be considered, such as the formation of polyatomic molecules with chloride ions in hydrochloric acid (HCl).[16] In order to combat these oxide and polyatomic interferences inline pre-filters such as an Apex® desolvation nebulizer helps to remove solvents capable of introducing interferences.[10] With these minimal considerations and the capacity for automation ICP-MS is advantageous choice for elemental analysis.

2.2 Solid phase extraction for ICP-MS

The specificity, sensitivity, and short analysis times associated with mass spectrometry makes it one of the most preferred methods used in high-throughput analysis. However the direct injection of a large number of complex samples into the instrumentation may not only adversely affect quantitation but also may cause damage to varying components of the system. In order to create a high- throughput and a high performing system a purification step must be invoked to eliminate or at least minimize matrix effects. One such method of purification includes solid phase extraction. Although, the term solid phase extraction (SPE) was coined in 1982, the use of a disposable cartridges filled with silica-based bonded phase sorbents for sample clean-up dates back to the mid to late 1970's.[26] The major advantages of using SPE over previously used liquid-liquid extraction technologies came with the need for high throughput. These advantages include reduced time and labor requirements, significantly lower solvent volumes, decreased risk of emulsion formation, selectivity, increased sorbent choices, and amenity to automation. As the use of SPE technology increased in popularity in the 1980's and early 1990's new polymeric sorbents were introduced in an effort to increase capacity, due to small surface area, and the instability in strongly acidic or alkaline solvents of the previously silica-based sorbents. Later in the 1990's functionalized polymers were introduced and addressed the low retention of polar compounds and the loss of performance after unintentional drying associated with the previous generation of polymers. Today SPE boasts a large number of hydrophobic and polar functionalized, neutral, and ion exchange polymeric SPE sorbents.[26] The traditional flow of operation for SPE consists of four steps that include: 1) conditioning of the sorbent with solvent and

water or with a buffer 2) loading of a sample in an aqueous or low organic mixed liquid phase, 3) washing away unwanted components with combinations of solvents, and 4) elution of the desired compound with the appropriate solvent. However the mechanism behind the extraction fall into three classes of interactions between the sorbent and the analyte: polar, ionic, and the van der Waals. Neutral sorbents that interact via van der Waal or hydrophobic forces have an associated energy of between 1 and 5 kJ/mol. These weak interactions exclude the use of a full strength solvent to conduct a thorough wash and often the extracts are plagued with contamination. Polar interactions can be subdivided into several different interactions with varying associated energy level including: dipole-induced dipole (2-7 kJ/mol), dipole-dipole (5-10 kJ/mol), hydrogen bonding (10-25 kJ/mol), and ion-dipole (10-50 kJ/mol). Ionic interactions are electrostatic and have the highest associated energy levels between 50 and 500 kJ/mol. Sorbents possessing ion exchange functionalities can tightly retain ionizable analytes and are amenable to concentrated solvent rinses and thereby removing large proportions of contaminations and furnishing cleaner extracts.[26]

2.2.1 TRU resin for radionuclides

Eichrom's TRU Resin is an extraction chromatographic material in which the extractant system is octylphenyl-N,N-di-isobutyl carbamoylphosphine oxide (abbreviated CMPO, Figure 2.7) dissolved in tri-n-butyl phosphate (TBP). The CMPO/ TBP solvent system complexes actinide elements and extracts them out of certain acidic aqueous solutions. The tetravalent actinides show extremely high retention on the column, at nitric acid concentrations in excess of 2M. Hexavalent uranium is slightly less followed by trivalent

americium and plutonium. It is important to note that pentavalent neptunium exhibits very low retention at any nitrate concentration.[27] The presence of certain cations may effect the uptake of actinides. Calcium and divalent iron show no effect, particularly valuable since both are present in large quantities in many environmental and bioassay samples. Aluminum actually increases the uptake of actinides on the TRU Resin column by driving the formation of the actinide-nitrato complex that is readily extracted by the CMPO/TBP system. However, trivalent iron shows a significant, negative effect on Am retention. If it is suspected that iron is present in a sample, a reducing agent such as ascorbic acid should be added to ensure that all Fe(III) is reduced to Fe(II).[27] Additionally, some commonly occurring polyatomic anions have a significant adverse effect on the retention of the tetravalent actinides and care should be taken for samples with elevated levels of phosphate, sulfate, and especially oxalate. The effect of oxalate is quite significant for the tetravalent actinides which readily form oxalato complexes that are not extracted by the CMPO/TBP solvent system. Uranium retention is not affected significantly by oxalate until the concentration exceeds 0.1M.[27]

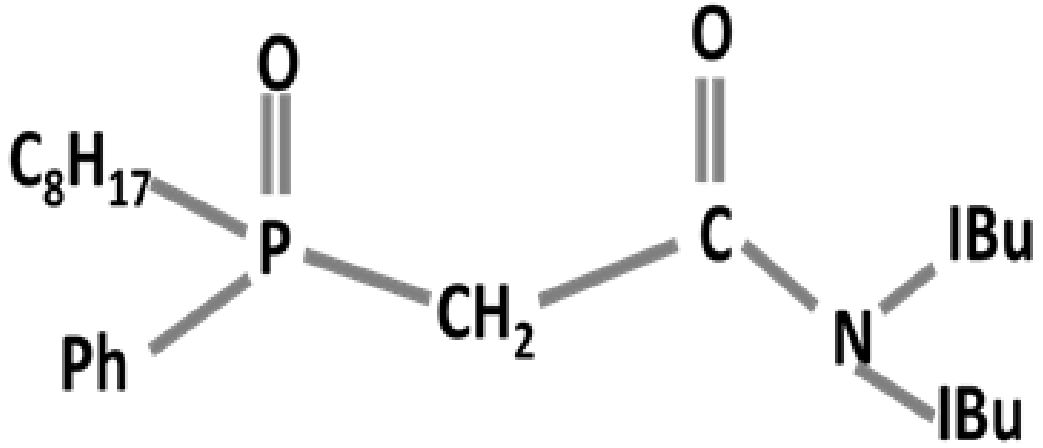

Figure 2.7 Octylphenyl-N,N-di-isobutyl carbamoylphosphine oxide (CMPO)

2.3 References

[1] Montaser, A., *Inductively coupled plasma mass spectrometry*. 1998: John Wiley & Sons.

[2] Hoffmann, E.D., et al., *Mass spectrometry: principles and applications.* Journal of the American Society for Mass Spectrometry, 1997. **8**(11): p. 1193-1194.

[3] Easter, R.N., J.A. Caruso, and A.P. Vonderheide, *Recent developments and novel applications in GC-ICPMS.* Journal of Analytical Atomic Spectrometry, 2010. **25**(4): p. 493-502.

[4] Gourgiotis, A., et al. *Comparison of cyclonic and impact bead spray chambers in inductively coupled plasma-quadrupole mass spectrometry (ICP-QMS): application in natural U and Th isotopes*. in *AGU Fall Meeting Abstracts*. 2009.

[5] Boumans, P., *Inductively coupled plasma-atomic emission spectroscopy: its present and future position in analytical chemistry.* Fresenius' Zeitschrift für Analytische Chemie, 1979. **299**(5): p. 337-361.

[6] Kniseley, R.N., et al., *An improved pneumatic nebulizer for use at low nebulizing gas flows.* Applied Spectroscopy, 1974. **28**(3): p. 285-286.

[7] Todoli, J.-L. and J.-M. Mermet, *Liquid sample introduction in ICP spectrometry: A practical guide*. 2011: Elsevier.

[8] Olesik, J.W. and J.C. Fister, *Incompletely desolvated droplets in argon inductively coupled plasmas: their number, original size and effect on emission intensities.* Spectrochimica Acta Part B: Atomic Spectroscopy, 1991. **46**(6): p. 851-868.

[9] Paredes, E., et al., *Influence of nebulizer design and aerosol impact bead on analytical sensitivities of inductively coupled plasma mass spectrometry.* Spectrochimica Acta Part B: Atomic Spectroscopy, 2010. **65**(11): p. 908-917.

[10] *APEX Sample Inlet System: a high stability, high sensitivity, low-memory desolvating inlet system for ICP-OES & ICP-MS* 2010, Elemental Scientific Inc. : Omaha, NE 68131 USA

[11] Jenner, G., et al., *ICP-MS—a powerful tool for high-precision trace-element analysis in earth sciences: evidence from analysis of selected USGS reference samples.* Chemical Geology, 1990. **83**(1): p. 133-148.

[12] Schramel, P., *ICP and DCP emission spectrometry for trace element analysis in biomedical and environmental samples. A review.* Spectrochimica Acta Part B: Atomic Spectroscopy, 1988. **43**(8): p. 881-896.

[13] Tagami, K. and S. Uchida, *Rapid uranium preconcentration and separation method from fresh water samples for total U and 235 U/238 U isotope ratio measurements by ICP-MS.* Analytica chimica acta, 2007. **592**(1): p. 101-105.

[14] Unsworth, E.R., J.M. Cook, and S.J. Hill, *Determination of uranium and thorium in natural waters with a high matrix concentration using solid-phase extraction inductively coupled plasma mass spectrometry.* Analytica chimica acta, 2001. **442**(1): p. 141-146.

[15] Thomas, R., *Practical guide to ICP-MS: a tutorial for beginners*. 2013: CRC press.

[16] *X series ICP-MS Operators course manual*. 2007, Thermo Scientific Training Institute.

[17] Vanhaecke, F., et al., *Comparison of the application of higher mass resolution and cool plasma conditions to avoid spectral interferences in Cr (III)/Cr (VI) speciation by means of high-performance liquid chromatography–inductively coupled plasma mass spectrometry.* Analytica chimica acta, 2000. **419**(1): p. 55-64.

[18] Becker, J.S., *Inductively coupled plasma mass spectrometry (ICP-MS) and laser ablation ICP-MS for isotope analysis of long-lived radionuclides.* International Journal of Mass Spectrometry, 2005. **242**(2): p. 183-195.

[19] Dawson, P. and N. Whetten, *Radio Frequency Quadrupole Mass Spectroscopy.* Adv. Electron. Electron Phys, 1969. **27**: p. 58-158.

[20] Izmer, A., S. Boulyga, and J.S. Becker, *Determination of 129 I/127 I isotope ratios in liquid solutions and environmental soil samples by ICP-MS with hexapole collision cell.* Journal of Analytical Atomic Spectrometry, 2003. **18**(11): p. 1339-1345.

[21] Hill, S.J., L.J. Pitts, and A.S. Fisher, *High-performance liquid chromatography–isotope dilution inductively coupled plasma mass spectrometry for speciation studies: an overview.* TrAC Trends in Analytical Chemistry, 2000. **19**(2): p. 120-126.

[22] Kerl, W., et al., *Isotopic and ultratrace analysis of uranium by double-focusing sector field ICP mass spectrometry.* Fresenius' journal of analytical chemistry, 1997. **359**(4-5): p. 407-409.

[23] Heumann, K.G., *Isotope dilution mass spectrometry.* International Journal of Mass Spectrometry and Ion Processes, 1992. **118**: p. 575-592.

[24] Becker, J.S., et al., *Determination of uranium and thorium at trace and ultratrace levels in urine by laser ablation ICP-MS.* ATOMIC SPECTROSCOPY-NORWALK CONNECTICUT-, 2004. **25**(5): p. 197-202.

[25] Rädlinger, G. and K.G. Heumann, *Iodine determination in food samples using inductively coupled plasma isotope dilution mass spectrometry.* Analytical chemistry, 1998. **70**(11): p. 2221-2224.

[26] Wang, P.G., *High-throughput analysis in the pharmaceutical industry*. 2008: CRC Press.

[27] Horwitz, E.P., et al., *Separation and preconcentration of actinides from acidic media by extraction chromatography.* Analytica Chimica Acta, 1993. **281**(2): p. 361-372.

CHAPTER 3:
THE AUTOMATION AND OPTIMIZATION OF SOLID PHASE EXTRACTION INDUCTIVELY COUPLED PLASMA MASS SPECTROMETRY ANALYSIS FOR THE HIGH THROUGHPUT DETERMINATION OF AQUEOUS LEVELS OF U, TH, NP, PU, AND AM.

A version of this chapter was originally published by Jennifer J Charlton, Micheal J Sepaniak, Alison K Sides, T Greg Schaaff, Darrin K Mann, and James A Bradshaw.

> Charlton, J.J., et al., *The automation and optimization of solid phase extraction inductively coupled plasma mass spectrometry analysis for the high throughput determination of aqueous levels of U, Th, Np, Pu, and Am.* Journal of Analytical Atomic Spectrometry, 2013. **28**(5): p. 711-718.

All changes from the original manuscript are trivial in nature and result from reformatting to conform to standards for a dissertation as required by The University of Tennessee in Knoxville. James A. Bradshaw is the corresponding author on this work and contributed in the initial setup of the automated system as well as parts of the introductory text. The remaining coauthors contributed intellectual capital.

3.1 Abstract:

The development of an automated chemical and mechanical sequence is presented for actinide analysis by inductively coupled plasma mass spectrometry (ICP-MS) using a column-based chromatographic system with TRU Resin for matrix separation. The approach yields a robust method that allows for simple handling with high sample throughput for use in rapid response scenarios. Nanogram-level studies were carried out using ICP-MS with mono-isotopic spiked samples. Sample throughput was extrapolated to successfully handle over 2000 samples a day. This process includes a manual valency adjustment allowing for direct optimal loading while simultaneously minimizing sample dilution, an automated solid phase extraction platform, and a unique transfer system for flow through from the extraction to the ICP-MS detection platform. Bed volumes, reagent

compositions, resin environments as well as volume and flow rates were optimized to increase recovery. Under optimal conditions the average recoveries over the range from 0.1 to 1.0 µg/L were 238U 106.3 ± 5.4 %, 237Np 100.5 ± 2.3 %, 242Pu 94.3 ± 5.2 % and 232Th 109.2 ± 4.8 %. Using synthetic urine as a complex matrix the recoveries were 238 U 96.2 ± 1.6%, 237Np 95.4 ± 1.7 %, 242Pu 81 ± 2.4 %, 232Th 98.8 ± 1.7 % and 241Am 53 ± 3.6 % for samples at the 1 µg/L level co-eluted with a 0.5 M HCl / 0.3 M oxalic acid solution. These high recoveries were obtained while successfully removing 99.999% of monitored matrix ion constituents and minimizing reagent volumes, culminating in the development of a method that allows for rapid onsite handling of a large number of samples while maintaining high recovery and consistency inherent to automation.

3.2 Introduction

Initiatives are underway both within and outside the United States to provide sample analysis for the purposes of site remediation from prior contamination. Determination of the extent of contamination across large areas including a variety of environments (i.e. water systems, soil, man-made structures, etc.) dictates both the approach as well as contingencies involved in clean-up[1]. The nuclear fallout, for example, at the Fukushima site, has and will continue to pose significant hurdles to traditional actinide detection and analysis due the variety of sample types as well as the sheer volume of samples required to ensure a thorough and complete remediation. National security interests also benefit from these types of technological advancements. Were a significant number of people exposed to radioactive material, bioassay sampling, in addition to environmental samples,

would need to be rapidly collected and analyzed, to allow for effective medical treatment and identification of the extent to which a given area had been contaminated.

Much of the commercially available equipment in chemical process automation has been constructed for organic analysis or pharmaceutical applications. These systems suffer from significant corrosion problems due to the acid concentrations used in the separation of radionuclides. Most systems do not have adequate volume capabilities to handle the large volumes necessary for radiochemical separations as these processes require concentrating trace level samples. Furthermore, the typical analysis procedure does not lend itself to extremely high volume throughput[2, 3]. The current need for an automated process that is both compatible with the more extreme chemical constituents as well as the capability to provide mass-sample throughput is greater than ever.

The typical analytical approach, namely solid phase extraction (SPE), is one of the most time-consuming and labour intensive steps in a radiochemistry laboratory.[2, 4-8]. Previous attempts at the robust automation of SPE have yielded major advances but a large sample throughput remains elusive[9]. All aspects of the separation, from column conditioning, to loading, to rinsing and elution, are treated as separate steps generally procedure-specific to different actinides. Depending on the variety of actinides within a sample, multiple load-elution steps are necessary, if not entire splitting of samples for multiple analysis pathways.

Historically this separation strategy was dictated by the preferred detection technique of radiometric counting (i.e. alpha and gamma counters.) Actinides had to be well separated and of known identity before quantitating content via counting techniques[2]. High level

quantitation by thermal ionization mass spectrometry (TIMS) also benefits from this approach[4]. In the case of the need for mass-sample throughput however, these approaches are ill-suited at best. Modern inductively-coupled plasma mass spectrometry (ICP-MS) systems are capable of both high sample throughput as well as sufficiently sensitive detection for many applications. Where extremely high level quantitation is not necessary, instead only detection above certain concentration limits, ICP-MS provides a significant advantage. Furthermore, because mass spectrometry can discriminate and quantitate species based on mass, time intensive counting and individual actinide isolation techniques are not necessary[10].

Here we present a technique where actinides are selectively separated from their sampling environment in a single load-elution stage, significantly improving typical chemical processing time prior to analysis. This system is coupled to an automated ICP-MS that simultaneously detects and quantitates all radionuclide of interest. This technique applies to U, Th, Np, Pu, and Am though ongoing research efforts are underway to address additional species such as Cm, Pa and other radionuclides of interest. This change could double or possibly triple the capacity of the laboratory. Analysis of rush or emergency samples, which would normally take 2 or more days to complete, could be completed in under 24 hours or less without loss of separative performance.

In addition to ultimately being used to improve and automate the analysis of large numbers of samples collected for detection of actinide presence in production, environmental, process, and bioassay scenarios, an automated SPE would prove essential in the event of a mass population radiation exposure. An automated SPE could

also be trailer mounted and taken to the vicinity of the release, allowing either direct analysis of the samples (ICP-MS) or the pre-concentration of the samples to be shipped back to a central laboratory. Laboratories would be able to respond quickly as needed with this automated ICP-MS technology available to analyze large numbers of samples.

3.3 Instrumentation and materials

3.3.1 Materials

Mono-isotopic high quality reagent tracers of 1000 ± 3 µg/mL ^{238}U in 2% HNO_3 (High Purity Standards, lot 604605) 10 ± 0.05 µg/mL ^{232}Th 2% HNO_3 (High Purity Standards, lot 0815406), 5021.90 dpm/mL ^{237}Np in 2 M HNO_3 (lab prepared), 3217.49 dpm/mL ^{242}Pu in 2 M HNO_3 (lab prepared), and 20 kBq nominal activity per 5 mL sealed vial ^{241}Am (Amsterdam International, 59-25-50, KA9730) were used. Nitric acid Ultrex II (JT Baker, lot J38N76) and hydrochloric acid Ultrex II (JT Baker, lot J08N71) were ultra pure grade. Oxalic acid dihydrate (EMD Chemicals, lot TD30EZEMS) ascorbic acid (JT Baker, lot J38604) were certified ACS grade. Ferrous sulfamate solution (0.6 M) was prepared in house. All water used for dilutions was 18 MΩ or greater purity (Barnstead, Nanopure). Synthetic urine matrix was prepared with aqueous constituents of urea, NaCl, KCl, creatinine, Na_2SO_4, NH_4Cl, citric acid, $MgSO_4$, NaH_2PO_4, $CaCl_2$, oxalic acid, lactic acid, dextrose, Na_2SiO_3, pepsin, and nitric acid.

3.3.2 Instrumentation

Automated positive pressure column separations were conducted using a Gilson GX-274 ASPEC liquid handler with digital syringe pumps to deliver reagents at a controlled rate and with TRILUTION LH software user interface platform to dictate sequencing, volumes,

and rates. Automated sample transfer was accomplished via a four-channel length/time-lagged peristaltic pump controlled via an Arduino circuit synchronizing sample transfer and channel rinse stages. Exploratory samples were nebulized and introduced into the plasma using a Elemental Scientific Inc. MicroFlow PFA-AT nebulizer in an impact beam spray chamber with Peltier cooler. The samples that used the optimized method in the detection limit studies were introduced in to the plasma by an APEX desolvation nebulizer with an added nitrogen gas flow to increase sensitivity, limit solvent effects, and enhance stability. Analysis was conducted with Thermo Electron Corporation XSeries^{II} quadrupole ICP-MS with ThermoLab software package (see Fig I). Samples were transferred from the Gilson GX-274 ASPEC liquid handler to the ICP-MS for analysis via variable length tubing through a 4-1 junction directly into the APEX unit driven by a 4 channel peristaltic pump. A basic arduino-based sensor initiated switching between rinse solutions when samples were not being injected. The ICP-MS was set to auto-detect sample introduction via identification of an internal spike.

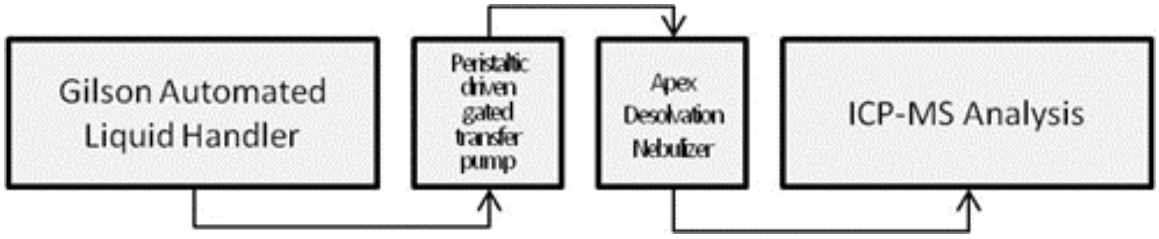

Figure 3.1. Step wise integrated instrumental aspects of method.

3.4 Approach and experimental procedure

3.4.1 Approach

The approach throughout the development of the method was to maintain a focus on the goals of automation, decreased causticity, decreased technician dependence, and increased throughput while maintaining high recoveries and sensitivities. These parameters are imperative to the development of system which may be pragmatically deployable in the case of high-dosage and/or large area exposure, where the need for rapid mass sample handling is tantamount.

3.4.2 Experimental procedure

3.4.2.1 Column preparation

Columns were prepared with Eichrom TRU resin 100-150 micron sphere-sized. The resin was manually loaded via aqueous slurry into 6 mL Applied Separations columns. Columns were topped with hydrophilic polyethylene frits, then closed with sealing caps.

3.4.2.2 Mixed actinide sample solution

Mono-isotopic stock solutions for each ^{238}U, ^{232}Th, ^{237}Np, ^{242}Pu, and ^{241}Am were created to a concentration of 100 µg/L in 5 % nitric acid. Samples containing 1 µg/L of ^{238}U, ^{232}Th, ^{237}Np, ^{242}Pu, and ^{241}Am were prepared by first pipetting 150 µL of each solution into a centrifuge tube and bringing up the volume to 9.5 mL with appropriate matrix solution. Three mL of 0.6 M ferrous sulfamate and 2.4 mL of 16 M nitric acid were added to obtain a final volume of 14.9 mL.

3.4.2.3 Valency adjustment experiments

To successfully retain the radionuclides of interest on the TRU resin they must be in either be in the hexavalent, tetravalent or trivalent state. Np in aqueous solution is generally in

the pentavalent state and therefore must be reduced to facilitate retention. To accomplish the proper valency adjustnments the aqueous mixed actinide samples were adjusted to 2.5 M nitric acid and 0.6 M ferrous sulfamate level. These samples were covered with parafilm and sonicated for 1 hr then heated on a hot plate in a water bath at 80^{o}C for 60 minutes, taking an aliquot every 20 minutes and separately at 60^{o} C for 120 minutes taking an aliquot every 30 minutes. After heating, the sample was cooled and 0.08 g solid ascorbic acid was added to the solution, which was then brought to a final volume of 15 mL with the addition of water, creating a 1 ppb load solution. The prepared columns were conditioned with 2.5 M nitric acid, and the solution was loaded on the column and rinsed with 10 ml of 2.5 M nitric acid both at gravity fed flow rates. The solution ran through the column and the wash were collected and analyzed via ICP-MS, for analyte breakthrough.

3.4.2.4 Automated extractions

The stepwise extraction that was converted from a completely manual procedure to a mostly automated procedure is depicted in Figure 3.2.

3.4.2.5 Initial automated sequence

Following solution preparation and appropriate valency adjustment of 1 hour at 80C, the initial extraction process consisted of first conditioning the columns, then loading the sample, washing the resin, chemically converting the column environment, and finally eluting and collecting the analyte. The initial extraction involved a multistep elution scheme. The prepared 1 mL resin columns were placed in the Gilson liquid handler where all source flow rates were 10 mL/min.

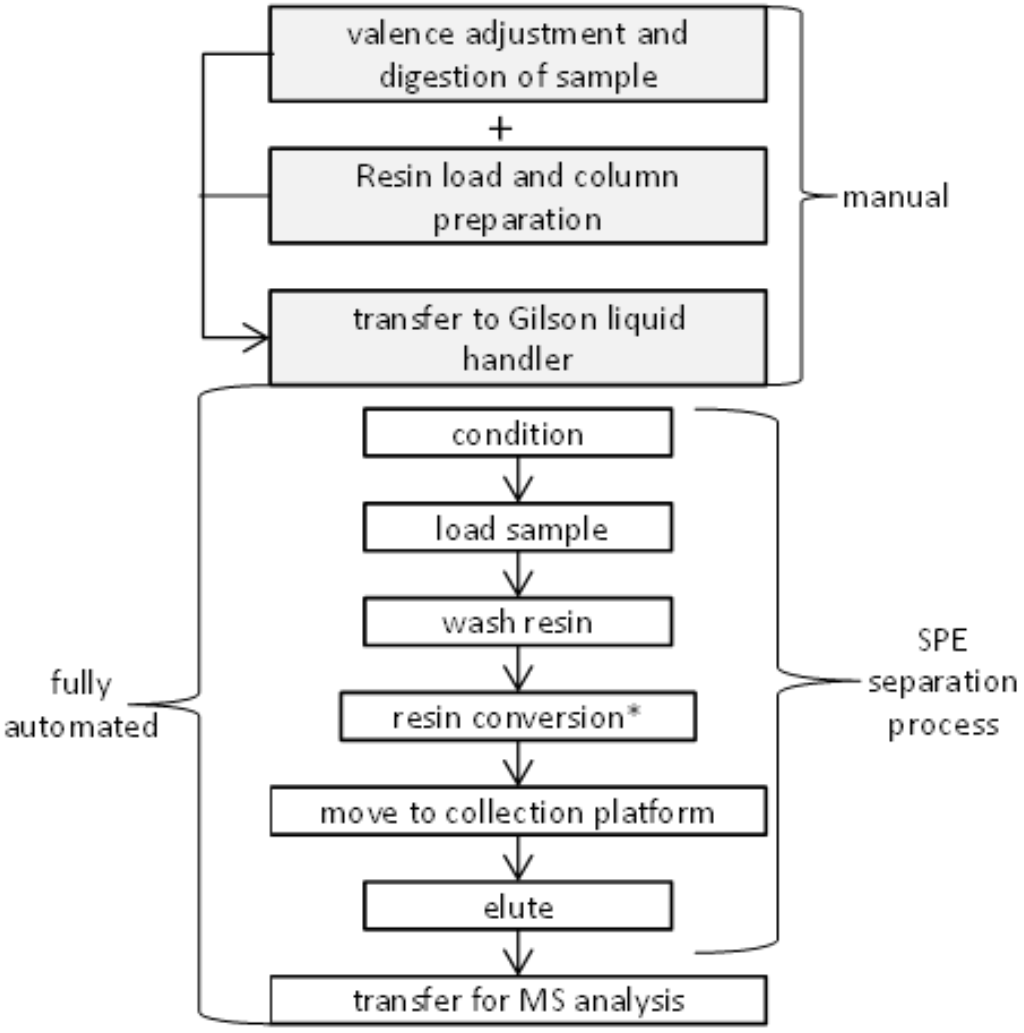

Figure 3.2. SPE chemical sequence used in extraction of actinides (* was eliminated in final method)

The columns were conditioned with 10 mL of 2.5 M nitric acid at a flow rate of 5 mL/min. Once conditioned, the columns were then loaded with 10 mL of the sample solution containing 1 µg/L of ^{238}U, ^{232}Th, ^{237}Np, ^{242}Pu, and ^{241}Am at a flow rate of 5 mL/min. Analytes retained in the sample injection probe were simultaneously rinsed onto the resin from the sample introduction point. Columns were rinsed to remove the matrix with 20 mL of 2.5 M nitric acid at a flow rate of 5 mL/min. The elution process of the analytes started with a conversion process from a nitric environment to a chloride environment with a 2 mL volume of 9 M HCl, at 5 mL/min flow rate followed by a 100 µL syringe supplied air push at 5 ml/min. The samples on the resin were then robotically transferred to the collection platform. A step wise elution scheme adapted from Horwitz, et al [11] included 5 mL of 4 M HCl then 10 mL volumes of 1.5 M HCl and 1M HCl / 0.03 M oxalic acid at flow rates of 5 mL/min, each followed by a 100 µL syringe supplied air push at 5 ml/min. Due to the ability of mass spectrometry to discriminate between elements of interest, the focus was not on separation instead on collection and recovery. The eluents were collected in one sample and transferred for ICP-MS analysis.

3.4.2.6 Oxalic acid tests

In testing oxalic acid levels only uranium was initially analyzed at the varying concentrations, and then the full actinide sequence was analyzed at the optimal uranium conditions. The column conditioning, washing and conversion steps remained the same as described previously, however the elution scheme was changed to a single-step 5 mL elution with varying concentrations of a combined HCl/oxalic acid eluent at 1 M / 0.03 M, 1M / 0.09 M, 1M / 0.15 M, 1 M / 0.3 M, and 0.5 M / 0.3 M.

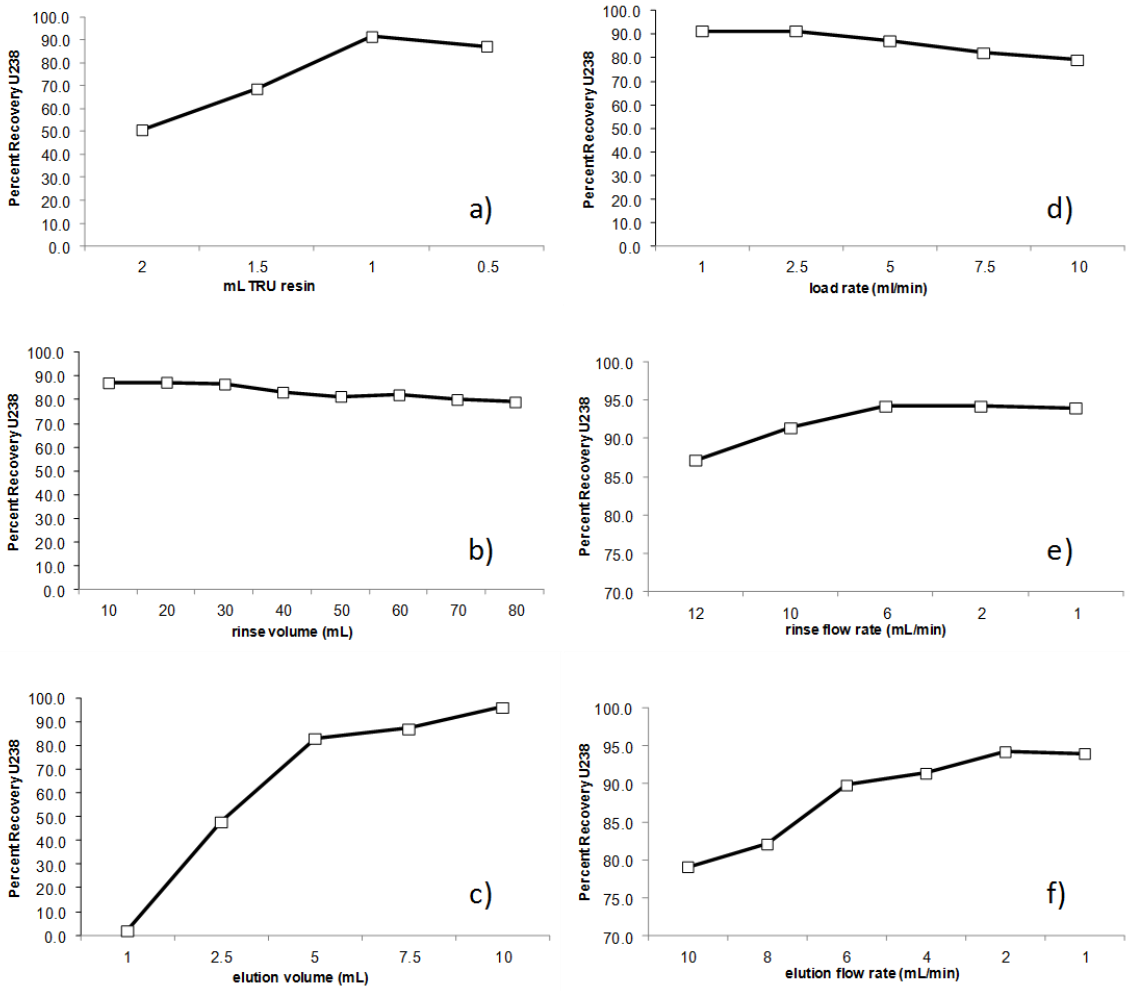

Figure 3.3. Rate and volume studies based on recovery of 238 U a) amount of TRU resin in column b) 2.5 M HNO_3 rinse volume study c) 0.3 M Oxalic Acid/ 0.5 M HCl elution volume study d) Sample load flow rate study e) 2.5 M HNO_3 rinse flow rate study f) 0.3 M Oxalic Acid / 0.5 M HCl elution flow rate study

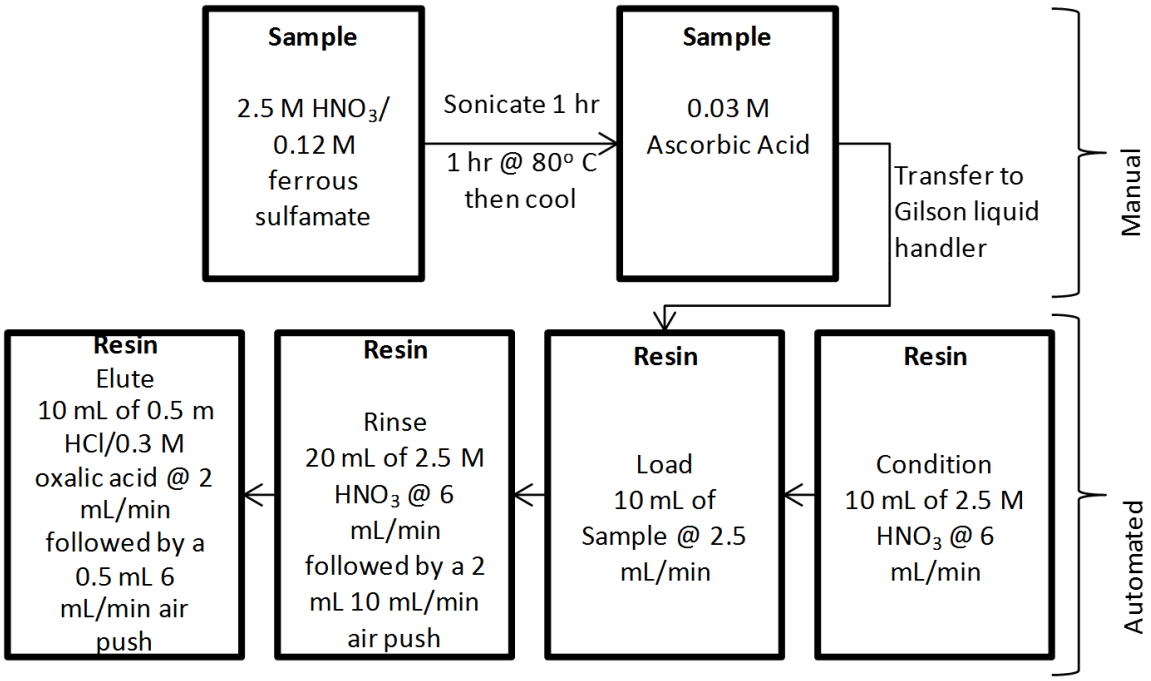

Figure 3.4. Step wise depiction of optimal method used for synthetic urine and detection limit studies

Table 3.2. Percent recoveries and percent relative standard deviation of ^{238}U, ^{232}Th, ^{237}Np and ^{242}Pu at 1 µg/L, 0.5 µg/L, 0.2 µg/L, and 0.1 µg/L.

Analyte	*1 µg/L*	*0.5 µg/L*	*0.2 µg/L*	*0.1 µg/L*	*average over range*	*% rsd over range*
^{232}Th	102.5	108.6	110.5	115.0	109.2	4.75
% rsd	2.5	3.5	4.6	6.8		
^{237}Np	101.2	101.6	102.0	97.0	100.5	2.31
% rsd	1.8	4.4	2.2	6.3		
^{238}U	101.8	101.0	111.5	111.0	106.3	5.36
% rsd	5.1	2.2	2.2	0.6		
^{242}Pu	93.6	99.6	96.0	88.0	94.3	5.16
% rsd	2.3	3.2	3.4	1.7		

The eluent was collected and transferred for ICP-MS analysis.

3.4.2.7 Conversion studies

Conversion method testing was conducted as described above using a 0.5 M HCl / 0.3 M oxalic acid eluent solution. The non-conversion method did not introduce the 9 M HCl conversion medium, instead allowing a time gap that was equivalent and kept the subsequent 100 µL syringe supplied air push at 5 ml/min. The eluent was collected and transferred for ICP-MS analysis.

3.4.2.8 Volume studies

All further testing was conducted via a consistent condition, load, rinse and a single elution chemical scheme while varying aspects of reagent and resin volumes as well as load, rinse and elution rates and treated as an evolutionary process maintaining the optimal conditions from the previous study to move forward to the next study. The chronology of the studies were: 1) resin bed volume, 2) wash volume, and elution volume, 3) rinse rate, load rate and elution rate. The resin bed volume study varied the volume of TRU resin in the column in half mL steps from 0.5 mL to 2.0 ml. The optimal level of resin of 1 mL was used in all subsequent studies. The rinse volume study varied the volume of the 2.5 M HNO3 from 10 mL to 80 mL in 10 mL steps. Eichrom reports that Fe and Ca can be retained by the TRU resin and large quantities in the eluted solution can add unwanted complexity to the matrix of the ionized solution[12-14]. The percent of 57Fe and 48Ca was directly compared via counts to the solution prior to loading the resin. Volumes of 2.5 M nitric acid were used as a wash. A 20 mL wash volume was adopted in subsequent studies. The elution volume study included 1 ml, 2.5 ml, 5 ml, 7.5 ml, and 10 mL volumes

of 0.5 M HCl / 0.3 M oxalic acid solution. The volume was mechanically limited by Gilson platform collection tubes. A 10 mL elution volume was used in subsequent studies.

3.4.2.9 Flow rate studies

Flow Rates were then studied for load, rinse and elution steps. Load flow rates that were studied included 1 ml/min, 2.5 ml/min, 5 ml/min, 7.5 ml/min, and 10 mL/ min. The rate of 2.5 mL/min was used as a load rate for subsequent studies. The rinse flow rates study consisted of 1 ml/min, 2 ml/min, 6 ml/min, 10 ml/min and 12 mL/min rates. A rinse flow rate of 6 mL/min was maintained for subsequent studies. The final rate that was studied was for the elution step, consisting of 1 ml/min, 2 ml/min, 4 ml/min, 6 ml/min, 8 ml/min and 10 ml/min rates. The rate of 2 mL/min was used in subsequent studies. All ICP-MS analyses was conducted on a Thermo Electron Corporation XSeriesII quadrupole ICP-MS using an impact bead spray chamber to introduce the sample into the plasma.

3.4.2.10 Studies of optimized method

After the completion of the chemical process optimization, a limit-of-detection study was undertaken using columns with a resin bed volume of 1 mL loaded onto the Gilson automated platform. Columns were conditioned with a 10 mL volume of 2.5 M HNO3 at a flow rate of 6 ml/min. 10 mL of the mixed analyte solution of appropriate concentration was loaded on the columns at a flow rate of 2.5 mL/min. The columns were then rinsed with 20 mL of 2.5 M HNO3 at a 6 mL/min rate followed by a 100 µL syringe supplied air push at 5 ml/min.

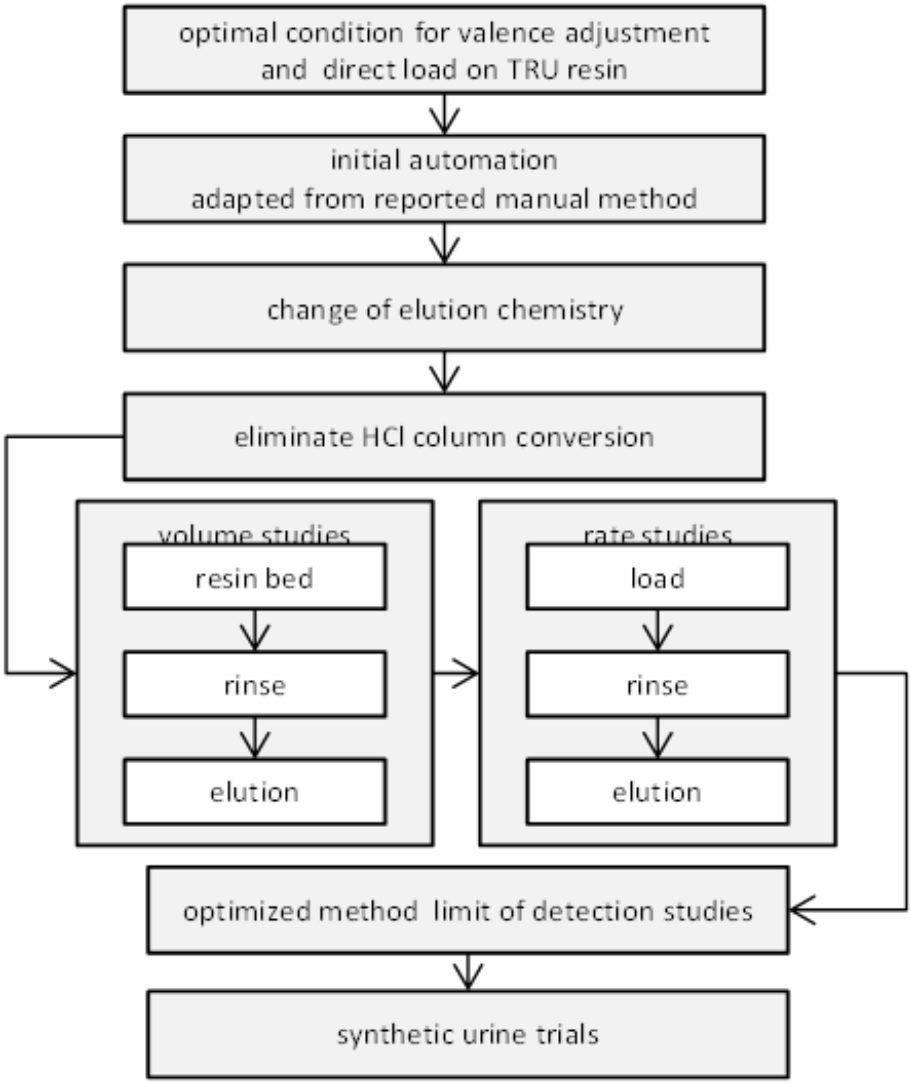

Figure 3.5. Progression of method from initial manual method to optimized automated method. The method was evolutionary in nature maintaining the optimal uranium recovery method from the previous study

The Gilson platform then mechanically moved the samples to a collection platform, and 10 mL of a 0.5 M HCl / 0.3 M oxalic acid eluting solution was applied to columns at a 2mL/min rate followed by a 100 µL syringe supplied air push at 5 ml/min. The resulting eluted solutions were collected for MS analysis. The study included varying analyte concentrations of 1 µg/L, 0.5 µg/L, 0.2 µg/L and 0.1 µg/L for ICP-MS analysis.

The automated transfer mechanism providing continuous flow through analysis from the Gilson liquid handler SPE platform to the apex desolvation nebulizer was constructed by transferring all four Gilson channels through time/length lagged tubing. Optical sensors and a custom programmed Arduino microcontroller synchronized transfer of samples and intermittent rinsing. The ThermoLab software utilized auto-detection capabilities to sample input, allowing compatibility without any necessary electronic triggering between the ICP-MS and SPE automation hardware.

The extrapolated number of samples able to be successfully analyzed in a 24 hour period was based on a timed run of a fully loaded Gilson platform which allows handling of 48 separate samples. Up to four of the SPE platforms may be run in tandem through the transfer mechanism for ICP-MS analysis before reaching a bottleneck.

3.4.2.11 Studies in synthetic urine

Using lab prepared columns with a resin bed volume of 1 mL loaded onto the Gilson automated platform, columns were conditioned with a 10 mL volume of 2.5 M HNO3 at a flow rate of 6 ml/min. 10 mL of the mixed analyte solution in a synthetic urine matrix of 1 µg/L was loaded on the columns at a flow rate of 2 mL/min. The columns were then rinsed with 20 mL of 2.5 M HNO3 at a 6 mL/min rate followed by a 100 µL syringe supplied air

push at 5 ml/min. The Gilson platform then mechanically moved the samples to the collection platform and 10 mL of a 0.5 M HCl / 0.3 M oxalic acid eluting solution was applied to the column at a 2mL/min rate followed by a 100 µL syringe supplied air push at 5 ml/min. The resulting eluted solution was collected for MS analysis. To evaluate the matrix removed from the analyzed sample, a two point analysis of metal ions was conducted. A 20 mL rinse volume removed, greater than 99.999% of 57Fe and 48Ca ions content was removed.

3.4.2.12 ICP-MS analysis and recovery

Electron Corporation XSeriesII quadrupole ICP-MS included an internal standard of 1 µg/L 165Ho and a three point linear calibrated model with blank correction for 238U, 232Th, 237Np, 242Pu and 241Am at 0.1 µg/L, 0.5 µg/L and 1.5 µg/L concentrations in a 0.5 M HCl / 0.3 M oxalic acid matrix. The model was considered linear and was used if the correlation coefficient value was 0.995 or greater. The model was confirmed by an internal calibration verification (ICV) sample with 0.2 µg/L levels of 238U, 232Th, 237Np, 242Pu and 241Am and an initial blank verification (IBV) in a 0.5 M HCl / 0.3 M oxalic acid matrix. Upon completing eight sample analyses, the calibration model was rechecked with a continuing-calibration verification (CCV) sample of the same composition as the ICV and a continuing calibration blank. The calibration and each analysis were allowed a 120 second fast uptake delay for both sample and wash. Each was sampled in triplicate with 100 sweeps at 10.0 ms dwell time and averaged. The results were compared against the spiked levels, and reported in percent recovery of the known spiked level. In a field

analysis the volume dilution of 9.5 of sample to 15 mL of solution should be taken into consideration.

3.5 Results and discussion

The development of this automated method was considered an evolutionary process and optimal results were carried over to the next stage as described in the flow chart (Figure 3.3) and graph (Figure 3.4) of increasing recoveries.

3.5.1 Valency adjustment

The initial stage of the project was to develop a method that allows for simultaneous extraction of the full complement of commonly analyzed actinides in a single direct load method. The goals were to minimize pre-processing, step-wise dilutions, and reagent volumes, all while remaining compatible with the Gilson automated platform.

Eichrom's TRU extraction chromatography resin was chosen for the reported ability to successfully retain U, Th, Am, Np, and Pu simultaneously in specific valence states. Eichrom reports the success of retention of specific ions as a k' value, defined as the volume of eluent in free column volumes to peak maximum. The higher the k' value the more readily the resin will retain the analyte of interest.TRU resin has a high retention of the tetravalent actinides Pu(IV), Np(IV), Th(IV) with reported k' values in the range of 10^4-10^6 at nitric acid concentrations above of 2 M. Hexavalent uranium U(VI) is approximately one order of magnitude lower in the range of $10^{3.5}$. Trivalent americium Am(III) and plutonium Pu(III) max-out about 10^1. However, penta-valent species such as neptunium NP(V) have only nominal retention at any nitric acid concentration, therefore reduction of this species is important to retain it on the resin [12, 15, 16]. Current Eichrom

Technologies Inc. Analytic Procedures for TRU [6-8]require a calcium phosphate precipitation technique prior to valency adjustment via dissolving the precipitate in a 3.0M HNO_3 / 1.0 M $Al(NO_3)_3$ solution, adding 0.6 M ferrous sulfamate to the concentration of 0.1 M, then reducing the Fe(III) compound to an non-interfering Fe(II) via the addition of ascorbic acid prior to loading on the column. Our approach was to forgo the precipitation and directly add the reducing agents to the sample in a manner that is compliant with the hardware. The addition of $Al(NO_3)_3$ has been reported to enhance the retention of Am(III) as it has the effect of increasing the activity of nitrate ions in solutions, driving the formation of the americium-nitrato complex that is readily extracted by the CMPO/TBP extraction system[11, 16]. The addition of the compound changed the composition of the solution such that bubbles formed in the volumetric tubing of the Gilson liquid handler and was therefore was omitted. Due to the omission of the $Al(NO_3)_3$ from the solution the Am is not expected to be readily retained by the resin and therefore recoveries are expected to be low. In order to have the highest Am recovery under these conditions the nitric acid concentration of solution was 2.5 M. Eichrom reports that 2.5 M nitric acid has the retention of Am(III) and the lowest retention of interfering Fe(III) [11]. Thus a 2.5 M HNO_3 / 0.12 M ferrous sulfamate solution with heat at first 60 C and later 80 C was chosen to reduce the Np(V) to Np(IV) and for retention by the resin.

As shown in Figure 3.5, there was a steady increase of the retention of the neptunium over the heated times at both temperatures signifying a reduction from Np(V) to the readily retained Np(IV)[11, 16, 17]. The study also addressed the interference of the sulfate ion on the retention of the Th(IV) ion, as it is corrected over time with the addition of heat.

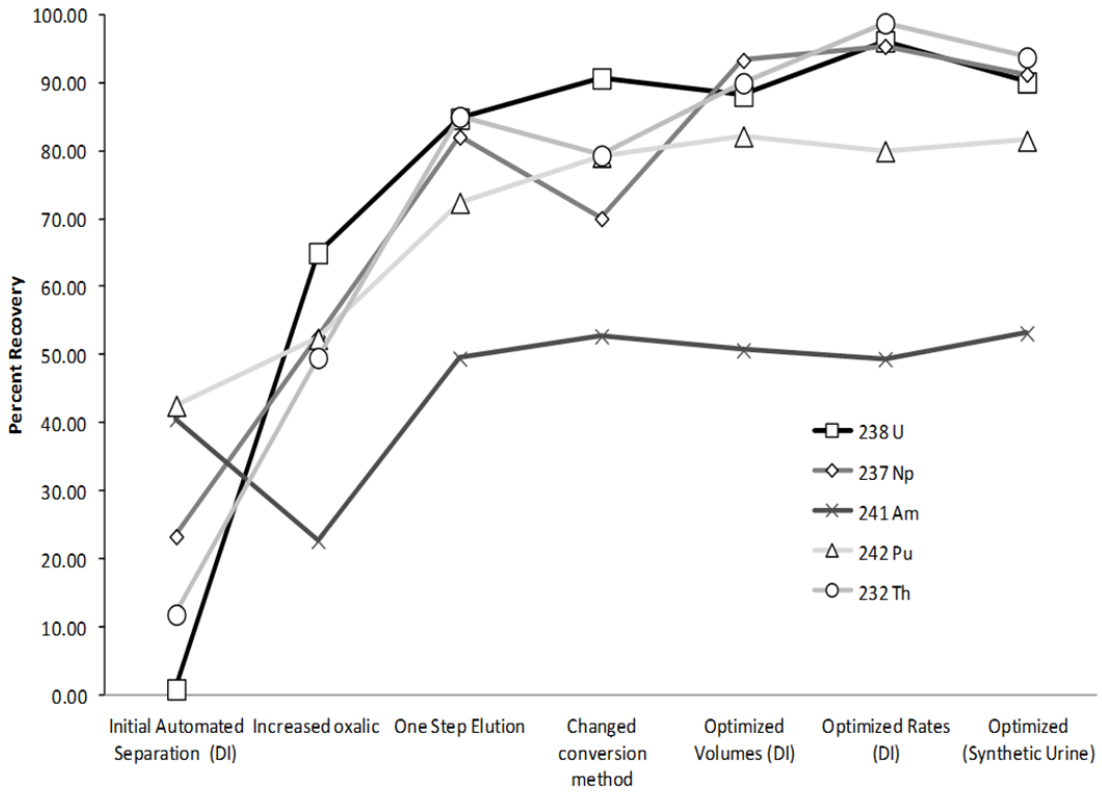

Figure 3.6. Result of each evolution of the method with an overall trend of increasing recoveries

With the heat set at 60^{o} C the Np only achieved retention of 80 percent on the resin after 90 minute, however after 60 minutes at a temperature of 80^{o} C the Np was retained at 93 %. The time of 1 hour at 80^{o} C was chosen to continue forward, so as to allow full valance transformation of Np(V) to Np(IV) and minimize the reduction of Pu(IV), and ensure that the Th interference was minimized.

3.5.2 Initial automated attempt

Adapting a method from Horwitz et al[18], the first attempt at an automated method had minimal recoveries with U 0.8%, Th 11.8%, Np 23.3%, Am 40.6% and Pu 42.6%. This adaptation also required extensive mechanical manipulation of the column in order to collect the multistage elution scheme.

Thus a single elution scheme was used based on the reported oxalato complexes that form with tetravalent actinides, and employed solutions of oxalic salts to strip actinides selectively from TRU resin using selective concentrations[11]. With the intent to strip every actinide effectively from the resin in a single elution, increasing the oxalic acid concentration and decreasing the HCl concentration was examined, following only the U elution results.

3.5.3 Single elution with oxalic acid

Due to the reported high complexation ability of the oxalate ligand[19] varying concentrations of an hydrochloric acid/ oxalic acid mixture were used as eluents. As shown in Table I the recovery of uranium was increased by a factor of almost 14 with a tenfold increase in the oxalic acid concentration as well as a fifty percent reduction in the hydrochloric acid concentration.

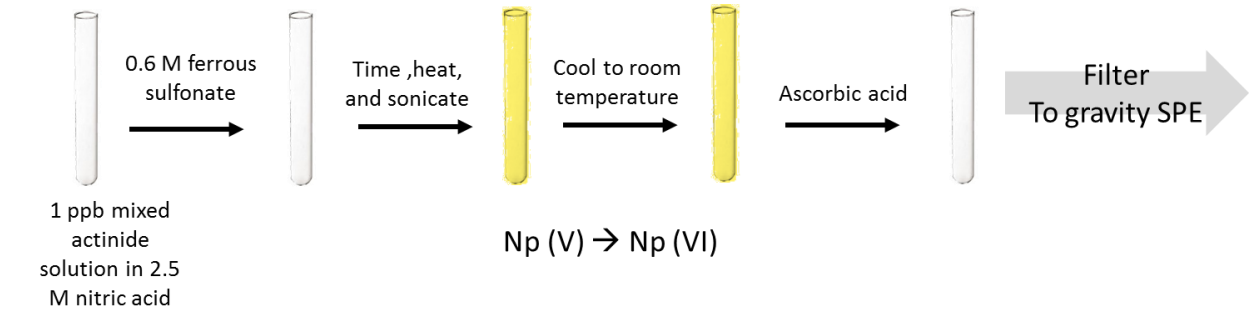

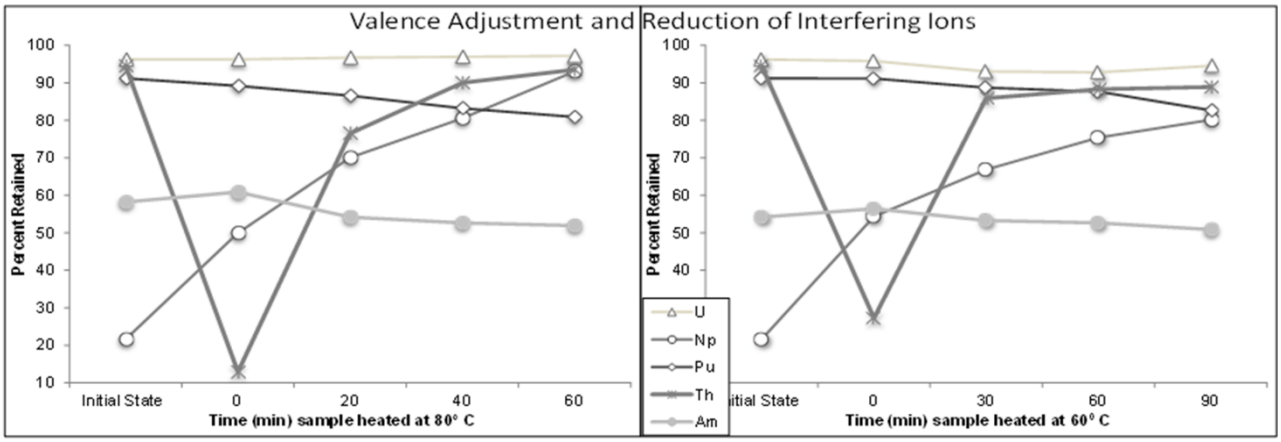

Figure 3.7. Temperature and time monitored 2.5 M HNO3 / 0.6 M ferrous sulfamate valence adjustment of actinide series as determined by retention on TRU.

The lower range was chosen from the Eichrom literature and the upper range was chosen from the pragmatic reason that the oxalic acid went into and stayed in solution without the addition of heat or vigorous agitation. When the full range of actinides was examined under these conditions, the percent recoveries were found to be ^{238}U 84 %, ^{241}Am 50 %, ^{237}Np 82 %, ^{232}Th 85 %, and ^{242}Pu 72 %. The across actinide recoveries all increased thus the 0.5 M HCl / 0.3 M oxalic acid solution was chosen as the elution scheme. The conversion of the column from a nitric acid environment to a hydrochloric acid environment was examined next with the intent of minimizing reagents volumes and the caustic 9 M HCl solution used to make the conversion, while either increasing or maintaining recoveries.

3.5.4 Column conversion

As shown in Table 3.2, upon direct elution after loading and washing, skipping the conversion process, and leaving a time gap to maintain consistent timing, the recovery of ^{238}U, ^{241}Am, and ^{242}Pu increased, however the recoveries of the tetravalent ^{232}Th and ^{237}Np decreased. In part, because of the emphasis on obtaining the highest possible ^{238}U recovery with minimal reagent use of caustic reagents, the 9M HCl conversion of the column was omitted.

3.5.5 Volume and rate studies

Using the non-conversion methodology, various volumes studies were then pursued, as shown in Fig VI a, b, and c. The full actinide series was monitored, however the uranium recovery was used as the gauge as to what would be considered optimal conditions. The first study was a resin bed volume study giving an optimal recovery with 1 mL of TRU resin in the 6 mL column.

Table 3.1. Percent recovery of 238 U with varying oxalic acid and HCl concentrations

1 M HCl/0.03 M oxalic acid	6.24	
1 M HCl/0.09 M oxalic acid	6.35	
1 M HCl/0.12 M oxalic acid	27.36	
1 M HCl/0.15 M oxalic acid	67.93	
1 M HCl/0.3 M oxalic acid	80.25	
0.5 M HCl/0.3 M oxalic acid	84.79	

Table 3.2 Single elution method percent recovery of actinide series comparing a nitric acid column to a hydrochloric acid environment

	Th	*Np*	*U*	*Am*	*Pu*
HCl column conversion	85.0	82.1	84.8	49.5	72.4
No conversion	79.4	70.1	90.7	52.8	79.2

Following rinse volume studies found 20 mL removed 99.999% of ^{48}Ca and ^{57}Fe from a nitrated and iron-sulfamated synthetic urine solution, without compromise to actinide retention on the column. The final volume study was elution volume, where the highest allowed single tube volume of 10 mL was found to have the best recovery for uranium at 96%. When the volume studies were concluded, the precise delivery rate inherent to the Gilson liquid handler allowed for controlled rate studies of the load, rinse and elute stages shown in Figure 3.6 d, e and f. In each study, the highest recovery with the fastest flow rate was considered optimal. The optimal rate for loading the sample on the column in the system was found to be 2.5 mL/min. Rinse rate recoveries were found to be stable from 1 ml/min to 6 ml/min then dropped off at higher rates, thus 6 mL/min was considered the highest usable speed. The final rate study was the elution step with 2 mL/min found to be the optimal rate of elution. As shown in Fig IV, the overall trend is of increasing recoveries was realized at each stage in the evolution of the method. At the culmination of the discovery studies, the optimized method shown in Figure 3.7 was used to conduct synthetic urine studies and detection limit studies.

3.5.6 Limit of detection

Using the optimal method of extraction and elution on varying concentrations of analyte from the 1 µg/L to the 100 ppt range, the recoveries for the analyzed actinides maintained a high recovery rate with reported relative standard deviations at each concentration of less than 7%. The percent relative standard deviation of the range for all analyzed actinides was less than 5.4 % (shown in Table 3).

3.5.7 Studies in synthetic urine and matrix

The optimal method that was developed in deionized water was used with a complex synthetic urine matrix. The recoveries were 238 U 96.2 ± 1.6%, 237Np 95.4 ± 1.7 %, 232Th 98.8 ± 1.7 %, 242Pu 81 ± 2.4 %, and 241Am 53 ± 3.6 %.

3.5.8 Scalable to high throughput platform

A fully loaded platform of 48 samples was fully separated and transferred for analysis in 1 hour and 54 minutes. The system was designed with the capacity to effectively process four Gilson liquid handling units in tandem giving this platform a handling capacity of 2425 samples in a 24 hour period; counted after an initial three hour time lag for first sample to be processed.

3.5.9 Reagent volumes

Shown in Fig VIII the development of a method that focused on the minimization of the causticity and reagent volumes was imperative to allow for feasible deployment and reduce corrosion of platforms. Many current analytical procedures use a 8 M nitric acid solution to accomplish the necessary valency adjustment [6-8]. The highest nitric acid concentration within procedure presented here is 2.5 M. Also accomplished was the ability to forgo a caustic column adjustment with 9 M HCl[12, 16] and the use of a minimally caustic 0.5 M HCl concentration in the elution step. These parameters were an important aspect of the method, when considering the logistics of deployment and the effects of highly concentrated acid on instrumentation.

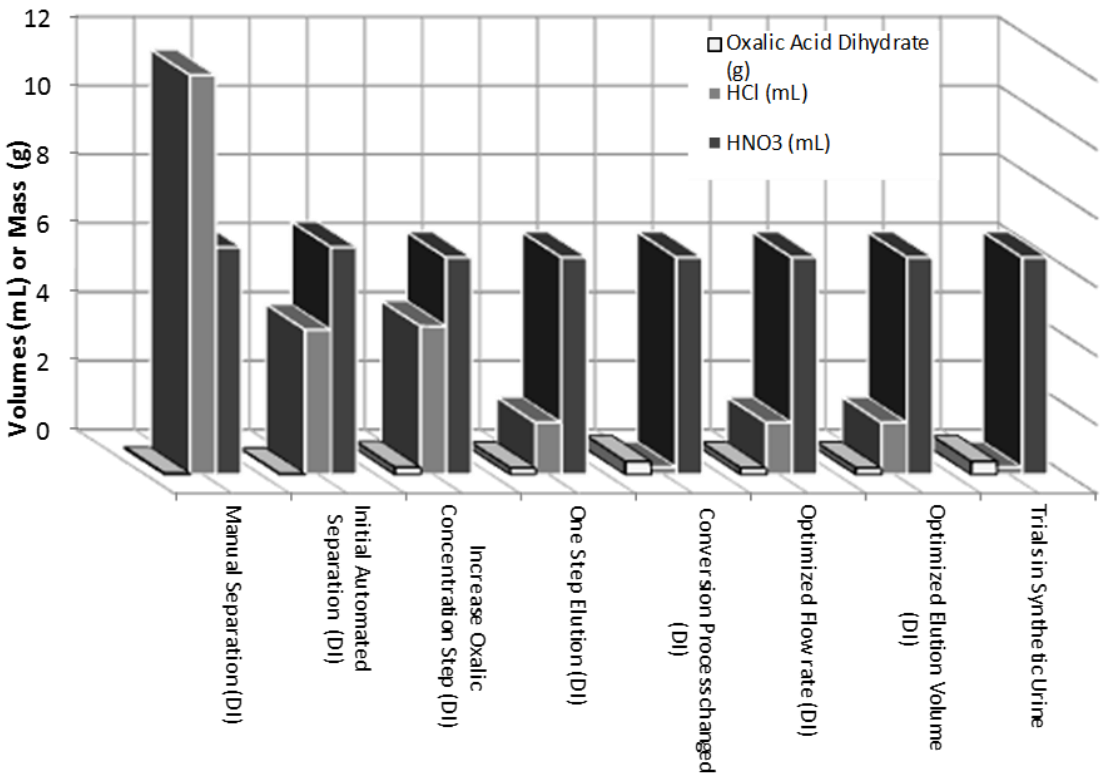

Figure 3.8. Minimization of concentrated reagent volumes decreased throughout the evolution of the process

3.6 Conclusions

This work presents a viable, robust, automated method for actinide pre-concentration, detection and analysis technique when rapid high-throughput sample processing is essential. Its merits include high recovery, minimized sample preparation and dilution, direct loading on the SPE platform, a one step elution process, high-throughput with decreased technician dependence, concurrent analysis of the major actinides while maintaining a field deployable platform.

3.7 Funding acknowledgement

The authors gratefully acknowledge funding from U.S. Department of Energy, National Nuclear Security Administration, Office of Non-proliferation and Verification Research and Development.

3.8 Notes and references

[a] *The University of Tennessee Knoxville, 420 Buehler Hall, 1420 Circle Dr. University of Tennessee, Knoxville, TN 37996-1600*

[b] *Y-12 National Security Complex, PO BOX 2009 MS 8244, OAK RIDGE, TN, 37831*

**Corresponding author, 865-576-8825, bradshawja@y12.doe.gov*

3.9 References

[1] Geldermann, J., et al., *Multi-criteria decision support and evaluation of strategies for nuclear remediation management.* Omega, 2009. **37**(1): p. 238-251.

[2] Egorov, O.B., et al., *Automation of radiochemical analysis: From groundwater monitoring to nuclear waste analysis*, in *Radioanalytical Methods in Interdisciplinary Research: Fundamentals in Cutting-Edge Applications*, C.A. Laue and K.L. Nash, Editors. 2004, Amer Chemical Soc: Washington. p. 246-270.

[3] Unsworth, E.R., J.M. Cook, and S.J. Hill, *Determination of uranium and thorium inn natural waters with a high matrix concentration using solid phase extraction inductively coupled plasma mass spectrometry.* 2001. **442**(2001).

[4] Grate, J.W., et al., *Extraction Chromatographic Methods in the Sample Preparation Sequence for Thermal Ionization Mass Spectrometric Analysis of Plutonium Isotopes.* Analytical Chemistry, 2011. **83**(23): p. 9086-9091.

[5] Chiarizia, R., et al., *Diphonix(R) resin: A review of its properties and applications.* Separation Science and Technology, 1997. **32**(1-4): p. 1-35.

[6] *Analytical Procedures : Americium, Plutonium and Uranium in Water*. 2005.

[7] *Analytical Procedures: Americium, Plutonium and Uranium in Urine*. 2005.

[8] *Analytical Procedures : Americium, Neptunium, Plutonium, Thorium, Curium, Uranium, and Strontium in Water (with Vacuum Box System)*. 2006.

[9] Grate, J.W., O. Egorov, and M.J. O'Hara, *Automated separation-based approaches to rapid radiochemical analysis and sensing.* Abstracts of Papers of the American Chemical Society, 2007. **233**.

[10] Tagami, K. and S. Uchida, *Rapid uranium preconcentration and seperation method from fresh water samples for total U and 235U/238U isotope ratio mesurements by ICP-MS.* 2007. **592**(2007).

[11] Horwitz, E.P., et al., *SEPARATION AND PRECONCENTRATION OF ACTINIDES FROM ACIDIC MEDIA BY EXTRACTION CHROMATOGRAPHY.* Analytica Chimica Acta, 1993. **281**(2): p. 361-372.

[12] Horwitz, E.P., et al., *Chromographic Materials for the determination of Actinides, Stronium, and Technetium in Environmental, Bioassay , and Nuclear Waste samples*. 1993.

[13] Horwitz, E.P. and M. Dietz, *Concentration and separation of actinides from urine using a supported bifunctional organophosphorus extractant.* Analytica Chimica Acta, 1990. **238**: p. 263-271.

[14] Horwitz, E.P., et al., *UPTAKE OF METAL-IONS BY A NEW CHELATING ION-EXCHANGE RESIN .1. ACID DEPENDENCIES OF ACTINIDE IONS.* Solvent Extraction and Ion Exchange, 1993. **11**(5): p. 943-966.

[15] Horwitz, E.P., *Extraction Chromatography of actinides and selected fission products*. Eichrom Industries.

[16] Horwitz, E.P. *Extraction Chormatography of Actinides and Selected Fission Products: Princibles and Achievement of Selevtivity*. in *International workshop on the application of extraction chromatography in radionuclide measurement*. 1998. Belguim.

[17] Chiarizia, R., et al., *UPTAKE OF METAL-IONS BY A NEW CHELATING ION-EXCHANGE RESIN .2. ACID DEPENDENCIES OF TRANSITION AND POSTTRANSITION METAL-IONS.* Solvent Extraction and Ion Exchange, 1993. **11**(5): p. 967-985.

[18] Horwitz, E.P., et al., *Preconcentration of Actinides from Acidic Media by Extraction Chromotography.* Analytica Chimica Acta, 1993. **281**: p. 361-372.

[19] Petit, J., et al., *Stability constants determination of successive metal complexes by hyphenated CE-ICPMS.* Electrophoresis, August 19, 2009. **31**(2010): p. 355–363.

CHAPTER 4:
INTRODUCTION TO NANOPILLAR ARRAYS FOR SELECTIVE TRANSPORT AND FLOURESCENCE ANALYSIS

4.1 Introduction

Richard Feynmann stated in 1959 that “There’s Plenty of Room at the Bottom”, predicting the recent explosion in nanotechnology research. Nanotechnology is the study of materials systems at nanometer-scale dimensions. At first glance, just making an object small may not seem interesting, but a material often behaves differently on nanoscale dimensions than in bulk, which has led to many interesting problems as well as new opportunities in miniaturization. While nanotechnology has touched many areas of research, this thesis concerns nano-optics, the study of light on the nanoscale, by using high aspect ratio nanopillar optical anntenea devices to control local electromagnetic fields and the field effect on the increase fluorescence emission of a target analyte.

4.1 Fabrication of nanopillar arrays and relevant related methodologies

Nanofabrication at its core aims to create nanoscale structures with the ability to serve as components in specific devises or act as a complete system on their own. Nanofabrication techniques look to reproducibly create tailored substrates. Overall two distinct groups of fabrication methods have emerged: bottom-up and top-down.[1] Bottom-up fabrication focuses on synthetic methods for creating substrates by assembling subnanoscale building blocks into specific patterns. The most common uses for these types of methods include biological and chemical sensors.[2] Top-down methods involve conventional lithographic techniques where nanoscale structures are created by removing parts of a bulk material, often by some etchant process. The top-down approach has been used commonly in electronic and photonic industries and is

also becoming increasingly more common in the creation of spectroscopy substrates,[2] but certain limits have prevented rapid development in these areas.

4.1.1 Electron beam lithography

Large parts of this dissertation focus on developing field enhanced nanopillar substrates via electron beam lithography (EBL). The potential for EBL to reproducibly create nano regime structures in a variety of shapes and sizes makes this fabrication method ideal for investigating effects of changes in pillar morphology on the electromagnetic field and subsequent fluorescence intensity at and near the surface of the structure. Since EBL pattering was first developed in the early 1960's [3], the semiconductor industry has pushed the technique toward miniaturization and increased throughput.[4-8]] The continued relatively slow serial pattering process has hampered its ability in mass-production settings [4]. EBL is generally used either in mask making for use with other lithography or, as in this case, in a direct writing process on the semiconductor substrate [9]. EBL is different than most photolithography in that the directed electrons, rather than photons, specifically expose a known location on the substrate instead of the entire surface. As such, there is no need for a mask when working with EBL [4] as the patterned areas are only created when directly exposed to the electron beam. The surface of the substrate is often coated with a photoresist, an electron sensitive material often coating a semiconductor wafer [10]. There are a variety of resists with varying resolution and time constraints, however the largest distinction is in the reaction of the resist to the electron beam.

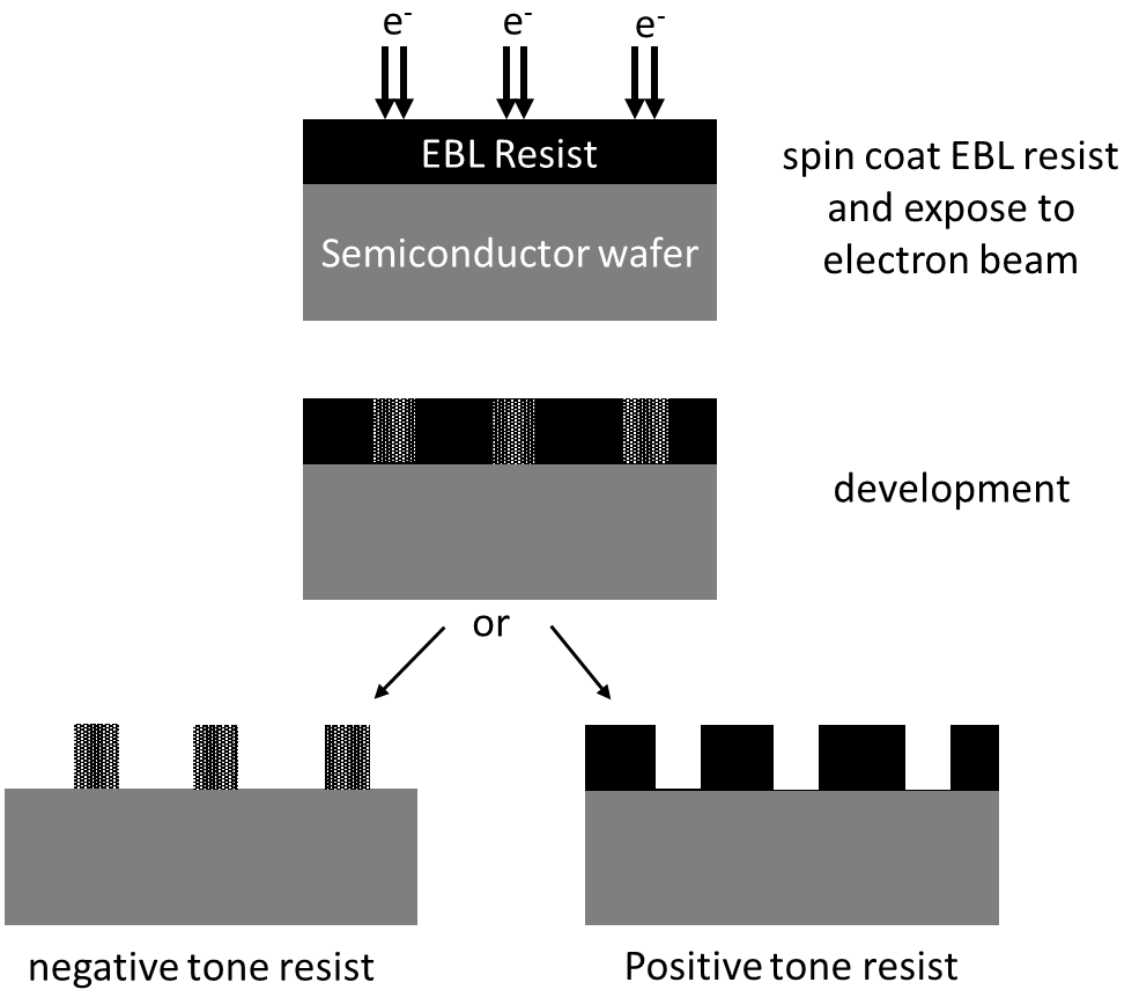

Figure 4.1. Illustration of development differences between negative and positive tone resists.

As shown in Figure 4.1 Positive tone resist molecules become depolymerized after exposure to the electron beam and are removed during development, creating space where the pattern was written. Negative tone resist molecules polymerize after exposure and remain during chemical development while the rest of the resist rinses away.

Figure 4.2 shows a simplified schematic of a common EBL system with the main components of a typical system as: an electron gun or source, a vacuum system or column to focus the electron beam, and a computer system that controls the various parts [9]. The electron gun controls the creation of the electron beam with the first step producing the electrons by cathodes or electron emitters. Once formed, the electrons are accelerated by electrostatic fields producing greater energy. A series of electric and magnetic lenses can focus and deflect the beam to a specific point on the substrate under a high vacuum. Finally, the computer system coordinates the movement of the electron beam and intermittently turn the beam on and off over the substrate expose selected areas of the substrate directly underneath to the beam.

EBL fabrication techniques can be optimized to obtain resolution better than +/- 10 nm [11]. Some of the parameters of optimization include, type of resist, the development method, and tuning the energy associated with the electrons within the beam. The Zep 520A resist utilized in the work reported herein is a type of high resolution PMMA and has resolution better than 10 nm [12]. The type of developer employed can help yield better contrast between developed and undeveloped areas. With high energy electrons, the beam can diffuse deeper into the resist causing more area to be exposed. Low energy electrons cannot scatter enough over large distances, leaving certain areas to

overexposure. In both cases either extremely high or low electron energies can lead to extra resist exposure [13], resulting in a detriment to the resolution of the method.

Following exposure and development a thin film of metal is vapor deposited on the surface. Through a previously developed lift off process[14-16] that removes unwanted resist and with it areas of the metal film a pattern of metal nanoparticles are created.This leaves the metallic features in known patterns or a mask that is followed by a reactive ion etching to create high aspect cylindrical pillars.

4.1.2 Reactive ion etching

The metallic features left on the surface of the substrate act as a hard mask for further etching of the substrate material. In nanofabrication this etching can be achieved either through a wet chemical etch or a dry plasma etch. While wet chemical is often the simplest form of etching using a solution to chemically attack the underlying surface while leaving the mask intact. The nondirectional manner in which it reacts with the substrate tend to undercut the substrate under the mask, decreasing the stability of nanoscale features [17]. In this research we utilize a dry plasma etching method to create the anisotropic profile we need to effectively harvest and collect light with our high aspect ratio pillar arrays. This dry plasma etch utilizes an ionized gas and an electric field to accelerate ions toward substrate. Where both physical (from the directional bombardment of the ions) and chemical (from the film reacting with the plasma) are balanced to create the desirable pillar profile [17]. A viable alternatives for nanopillar production via a lithography free pathway, is discussed in Chapter 5.

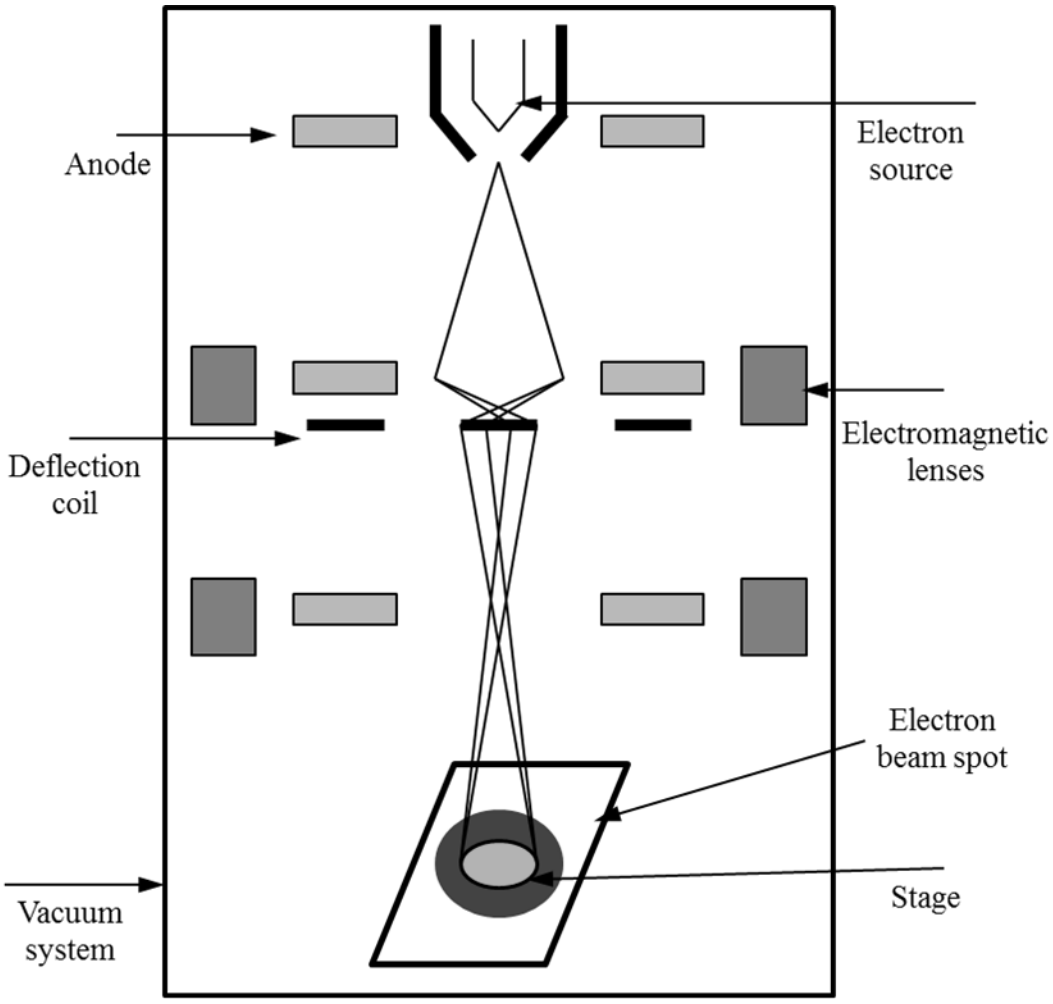

Figure 4.2. Simplified schematic of an electron beam lithography system.

4.2 Wicking in a pillar array system

4.2.1Mobile phase flow in capillary driven systems

The flow in a capillary driven system is dependent on the interplay between the surface tension (g) and the viscosity (h) of the of the model phase.[18] In these capillary driven systems it is predicted that the solvent front mitigation distance (Z_f) is proportional to the square root of the product of the mitigation time (t) and the proportionality consonant (k) as shown in Eq. 4.1 and Eq. 4.2.

$$Z_f = \sqrt{kt} \quad \text{Eq. 4.1}$$

$$k = \frac{2K_0 d_p g}{h \cos\theta} \quad \text{Eq. 4.2}$$

Where K_0 is the permeability constant, d_p is the particle size, Ɵ is the contact angle of the mobile phase.

4.2.2 Calculating mobile front displacement (Z_f) of the wicking front through rough wetting in pillar systems

Another method to predict the solvent front mitigation distance is through rough wetting. The basis of this calculation is diameter, gap, and height of pillars as well as the and viscosity and surface tension of the solvent and it's interaction with the substrate. Following the derivation in Mai et al[19], which is a previously established condition [20]

$$cos\theta > cos\theta_c = \frac{1-\varphi_s}{r-\varphi_s} \quad \text{Eq. 4.3}$$

must be met for wicking to take place. In this equation θ is the contact angle that the liquid makes with a smooth surface of the substrate and θ_c is the critical angle. θ_c is calculated based on the roughness (r) of the textured surface as ratio of surface areas and adjusted by φ_s a ratio of the area on top of the pillars to area of analysis. In the case of highly ordered periodic nanopillars,

$$r = \frac{\pi dh}{(d+g)^2} + 1 \qquad \text{Eq. 4.4}$$

$$\varphi_s = \frac{\pi d^2}{4(d+g)^2} \qquad \text{Eq. 4.5}$$

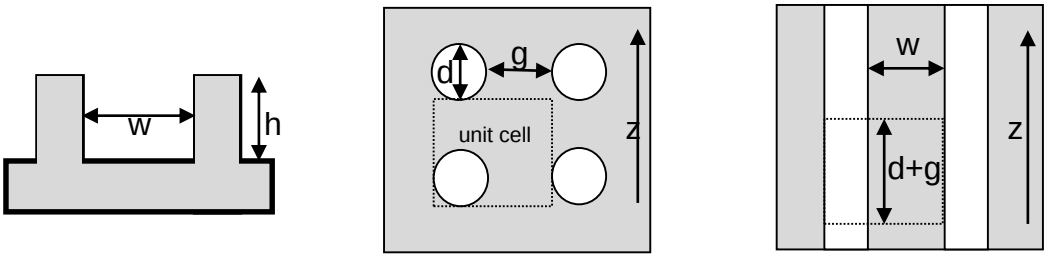

where d is the diameter, g is the gap (spacing between pillars), and h is the pillar height. The displacement of the wicking front (z) with time (t) was found to follow the diffusive relation

$$z = (Dt)^{1/2} \qquad \text{Eq. 4.6}$$

where t is time after start of wicking. D is derived assuming Poiseuille flow and equating the driving capillary pressure of wicking and the retarding forces of viscous loss,

$$D = \frac{2\gamma h}{3\mu\beta}\frac{cos\theta - cos\theta_c}{cos\theta_c} \qquad \text{Eq. 4.7}$$

where μ is the viscosity of the liquid, γ is the surface tension of the liquid and β is generally an empirically determined a constant and in this modeling the system β has been derived by Mai et al[19]. For ease of analysis the fluid flow is approximated as flow through open

nanochannels that are the same dimensions as the fabricated nanopillars. A unit cell of nanopillars will hold the same volume as a unit cell of nanochannels, the width (w) of the nanochannel can be calculated to be,

$$w = \frac{\left[(d+g)^2 - \frac{\pi}{4}d^2\right]h}{(d+g)h} = \frac{(4-\pi)d^2+8dg+4g^2}{4(d+g)} \quad \text{Eq. 4.8}$$

Mai et al[19], goes on to state that gravitational forces can be ignored due to the scale of the experiment as in Bico et al[20] and reduces the Navier-Stokes equation. Furthermorethe model sets boundary conditions such that the capillary pressure driving the force in z is independent of x and y. A velocity profile U is derived with an approximated U_{mean}. Using condition where $w \rightarrow \infty$ with the equation for Pioseuille flow over a flat surface then comparing the fully derived U_{mean} with mean velocity (U_{mean}) derived previously by Bico et al[20], the expression for β is:

$$\beta = \frac{4h^2}{w^2} + 1 \quad \text{Eq. 4.9}$$

4.3 Analytical application

4.3.1 Flourescence

In part this thesis measures the effect these structures have on molecular fluorescence, an effect that depends heavily on local electromagnetic fields. Fluorescence is a photophysical process whereby light of one wavelength excites a molecule, which in turn emits light of a lower energy, or longer wavelength. The simplest model to describe emission of light by a molecule is the two-level system, with each of the two primary electronic states that also have a progression of vibrational modes. Fluorescence consists of the absorption of a photon by a molecule followed by the emission of a lower energy photon (red-shifted wavelength) as seen in the Jablonksi diagram in Figure 4.3a.

On the excitation side, a wavelength of light is chosen whose energy is equivalent to or greater than the direct ground state (S_0) to excited state (S_1) allowed dipole transition (blue arrow). The singlet state (S) refers to the fact that all of the electrons in this state are paired with another electron of antiparallel spin. Not requiring a spin flip, a transition between two singlet states is an optically allowed transition. Figure 4.3b shows schematically the absorption (blue) and emission (red) spectra example. The excitation light can be chosen at any wavelength where there is absorption by the molecule. Once the molecule is in the excited state, internal conversion, or fast, non-radiative vibrational relaxations, occur in a few ps and the molecule relaxes to the lowest level of the electronic excited state. At this point, the molecule typically remains in the excited state for ~ few ns before relaxing to the ground state. This relaxation can either be radiative (red arrow), where the molecule emits a lower energy photon, or non-radiative (black arrow), where the molecule does not emit a photon but simply gives off the energy as heat and moves through other levels to relax to the ground state (internal conversion or intersystem crossing for instance). The width of the emission and the peaks in the spectrum in Figure 4.3b are due to the number of different vibrational levels available for the molecule to relax down to the ground state at room temperature.[21]

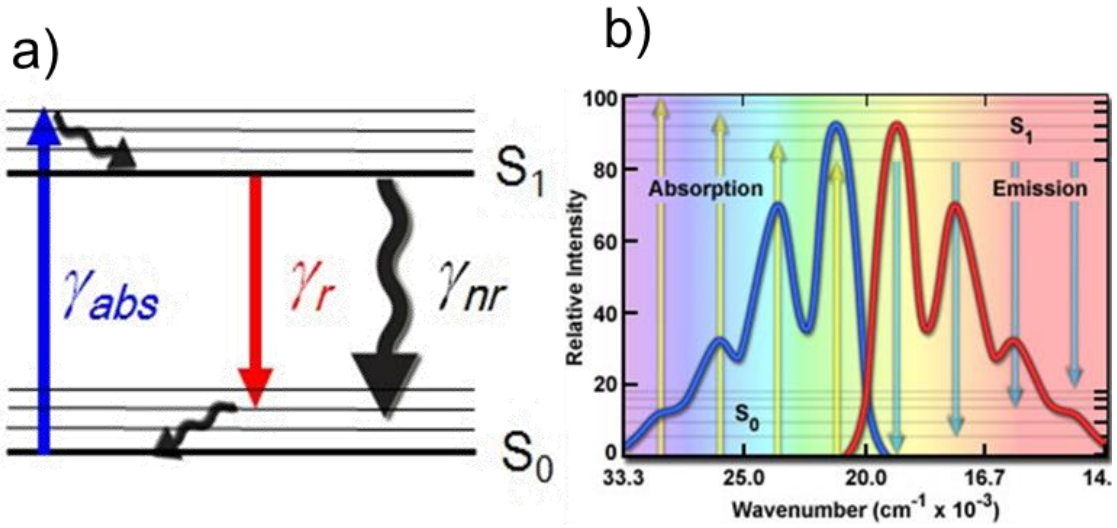

Figure 4.3. Simplified Jablonksi diagram for a typical fluorescence transition, and b) absorption (blue) and fluorescence emission (red) of example spectra.

4.3.2 Single-molecule fluorescence

For over two decades it has been known that a single molecule could be optically detected, first based on a measuring a single-molecule's absorption of light,[22] and then demonstrated by measuring absorption by recording a single-molecule's fluorescence emission[23] at low temperature. These early experiments were quickly followed by room temperature detection of single-molecule fluorescence[24]. This was followed by a rapid growth of the field of single-molecule fluorescence spectroscopy and imagining, particular in the biological community. Now, instead of performing bulk experiments and only measuring average behavior, it is possible to measure the behavior of every target molecule and understand heterogeneity in behavior.

In order to detect a single-molecule's fluorescence, a very good fluorophore is necessary. A good fluorophore has several properties. First, it absorbs light well, which corresponds to a high absorption cross-section. Second, a good fluorophore tends to emit radiatively instead of non-radiatively, which is reflected in the fluorescence quantum efficiency (QE). The QE is the probability that a molecule will emit a fluorescence photon per photon absorbed and is given by:[25]

$$QE = \frac{\gamma_r}{(\gamma_r+\gamma_{nr})} \qquad \text{Eq. 4.10}$$

where γ_r and γ_{nr} are the radiative and non-radiative decay rates, respectively. If the QE is 100%, then the molecule always emits a photon and never decays non-radiatively, making it an ideal fluorophore for most applications. A good fluorophore must be stable and capable of emitting many photons before photobleaching. Photobeaching refers to

any change in the molecule that occurs during illumination, typically involving a chemical reaction that alters the molecule's identity, causing it to no longer fluoresce. For example, a common pathway for a molecule to photobleach is called photooxidation that can occur when the molecule enters a triplet state, a forbidden transition from the singlet state that occurs with low probability. The triplet state represents an intermediate from which the molecule can return to the singlet ground state eventually. However, the triplet state is long-lived and so there is time for the molecule to react with triplet oxygen and cause the molecule to no longer fluoresce. A good fluorophore will emit ~10^6 photons before eventual degradation.[26]

4.3.3 Fluorescence microscopy

The field of fluorescence microscopy is rapidly growing, providing ever increasing imaging capabilities. Over the last decade, many new technologies and techniques have been developed which allow for deeper, faster, or higher resolution imaging. Fluorescence microscopy is a powerful tool that has vast capacity to detect and analyze many biological and elemental compounds. This versatility explains why google scholar is able to locate over two million articles in 0.13 seconds related to fluorescence microscopy techniques. Some advances include the widespread use of fluorescent proteins,[25] a large number of new fluorophores available[27], growth of the utility of the basic confocal microscope, use of multiphoton microscopy to optically image deeper into tissues, and breaking of the diffraction limit for super-resolution.[28] Many of the new advanced techniques are now being commercialized, opening their use to a large population of modern analysts. Microscopy experiments can be optimized by adjustments in image resolution, imaging

speed, and the amount of signal collected from the fluorescing sample all of which are bounded by the limits imposed by photobleaching and/or phototoxicity. In many experiments, photon densities at the diffraction limited spot size can be very high leading to destruction or changes in the signal of the fluorophore. While many techniques for fluorescence microscopy have been introduced, one of the most accessible and widely used techniques is wide field fluorescence microscopy.

4.3.4 Wide field fluorescence microscopy

In the most basic form, wide-field fluorescence microscopy (WFFM) involves exciting the fluorophore(s) in the sample of interest using a fluorescent light source, a microscope, excitation and emission filters, and an objective lens. The resulting emitted light, of longer wavelength, is observed through the microscope eyepieces or by a camera, followed by computer digitization.[29] WFFM is simple, relatively inexpensive technique that has high temporal resolution (ms/frame) and a x,y resolution that is diffraction limited at approximately 200 nm.[28] Developments in microscope and camera design, light filters, and in new techniques have greatly improved resolution and light collection for WFFM. One of the most significant advancements has been the development of low-noise, cooled CCD cameras. These cameras allow for the gradual accumulation of fluorescence signal to be integrated with little noise while still maintaining high resolution. The main disadvantage of basic WFFM is that that all of the emitted light is integrated through the sample in the z dimension. Therefore, it is difficult to tell where the fluorescence from a point in the sample originated in the z-dimension.

4.3.5 Determining resolution in the x,y plane

The Resolution in the x,y plane is a function of the numerical aperture (NA) of the objective lens and the wavelength of the excitation light according to Ernst Abbe's diffraction limit expression:[28]

$$R_{xy} = \frac{0.61\lambda}{NA} \quad \text{Eq. 4.11}$$

where λ is the wavelength of the emitted light and NA is the numerical aperture of the microscope objective. For a high NA objective (NA =1.4) the diffraction limit is around 200 nm.

4.3.6 Optical nano-antennas

The use of antennas in modern society are vast. Macroscopically antennae are used to receive and transmit radio and microwave range electromagnetic waves in devices such as cell phones, televisions, laptops, and radios. Microscopically, antennas are capable of capturing and concentrating these fields efficiently to subwavelength volumes. Notably, scaling radio-wave antennas to optical frequencies proved to be a challenge and use of these optical frequency antennas are interesting because light cannot be focused to an infinitesimally small point with normal lenses, instead it is limited by diffraction essentuall the same as Eq. 4.11.

$$d = \frac{\lambda}{2NA} \quad \text{Eq. 4.12}$$

where λ is the wavelength of light and NA is the numerical aperture of the optics used. For visible wavelengths the diffraction limit is ~200-300 nm, much larger than many objects of interest, such as single molecules, which are typically just a few nm in size (Figure 4.4). An antenna can help concentrate light to a smaller area and decrease the mismatch in size between light and the nanoscale emitter.

4.3.7 Optical properties of semiconductor nanopillars

Semiconductor nanostructures have been long known to be promising for applications in optics and optoelectronic devices. This notion has been well manifested by the tunable wavelength of light emitted from quantum dots in different sizes due to quantum confinement effects,[30] which finds broad applications from new light-emitting devices to novel biological tissue imaging agents. Although the nanopillars we investigate are in a size regime where the quantum confinement effect is negligible, the high aspect-ratio of the wire (in our case pillars) opens up unique opportunities for many important photonic applications[31, 32] that require anisotropic geometry, like waveguides.[33]. A large variety of nanopillar(wire)-based photonic devices have been demonstrated[33-36], to effectively extend optical functionalities down to the nanoscale regime. Recent studies have shown that semiconductor nanowires are particularly promising for photovoltaic applications.[37, 38] Arrays of semiconductor nanopillars or tapered nanocones can absorb more solar radiation than a comparable volume of bulk materials. Whereas numerous photonic devices have been demonstrated with semiconductor nanowires by far, many important questions regarding the optical properties of the nanowires still remain unanswered. Particularly, a thorough understanding of the fundamentals of light-matter interaction in the nanowires is critically lacking at this point. This understanding is of significance for both fundamental and applied interests.

4.3.8 Leaky Mode Resonances

The description of highly confined modes in optical fibers and microscale dielectric resonators is based on classical waveguide theory. It has been shown that by solving

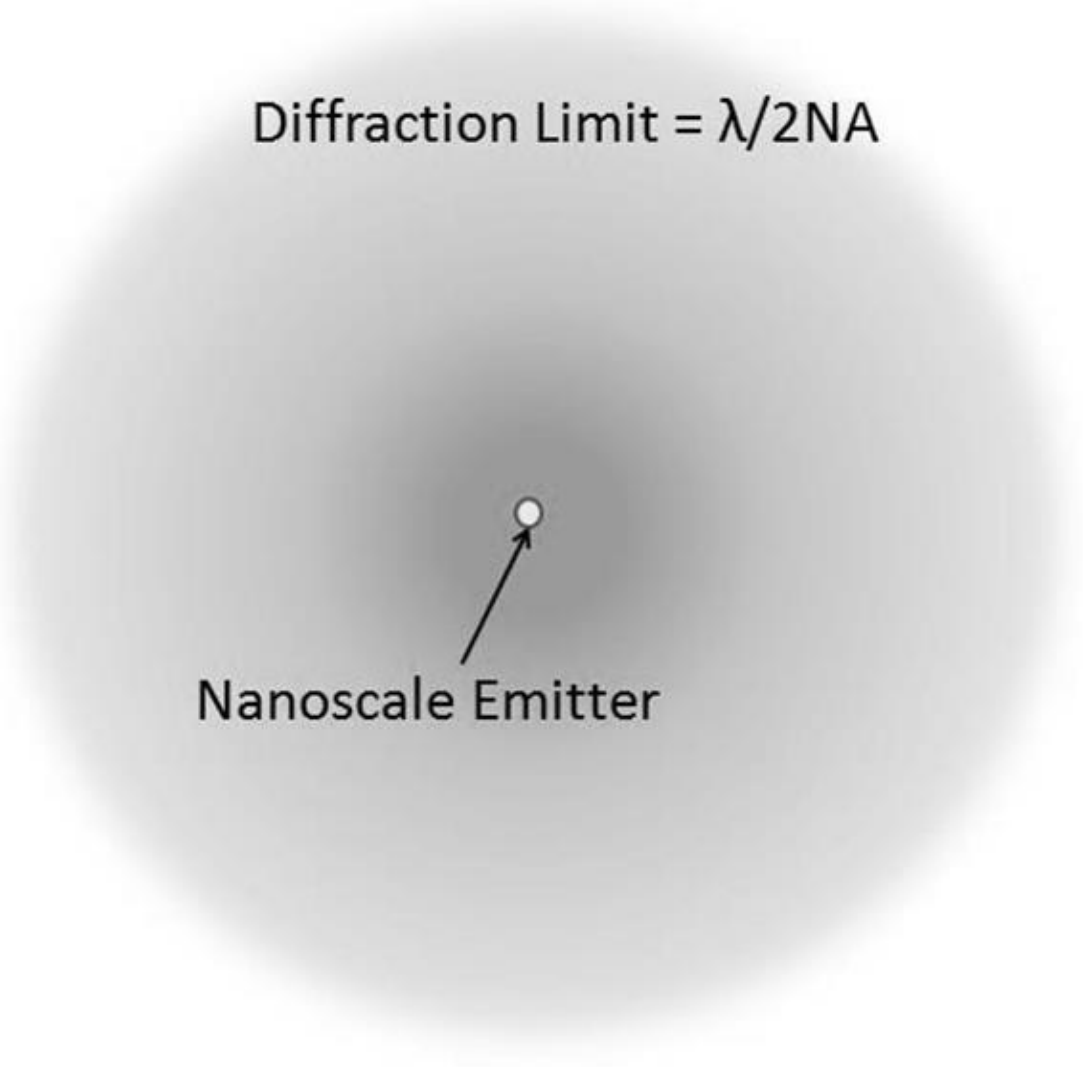

Figure 4.4. Size mismatch between the diffraction limit and a nanoscale emitter.

Maxwell's equations with the appropriate boundary conditions[39] it follows that nanowires tend to support a limited number of transverse electric (TE) and transverse magnetic (TM) leaky mode resonances (LMRs), which increase in number as their radius is increased. The complex and nontrivial nature of optical resonances in semiconductor nanowires and nanopillars clearly follows from a number of very recent studies in this area [40-45]. In particular, a series of recent studies by Brongersma's group [40-42] demonstrated that leaky mode resonances in semiconductor nanowires provide a powerful and elegant means to engineer light absorption in optoelectronic devices [42, 46] and tune the color of silicon nanostructures [40]. Muskens *et al.* [47] showed that strong Mie-type internal resonances in vertically aligned semiconductor nanowire arrays lead to record levels of light scattering that can be tuned over a wide spectral range. Furthermore, the guided mode properties of individual silicon nanopillars can give rise to a palette of surprisingly vivid colors readily visible in bright field microscopy [43].

4.4 References

[1] Fan, M., G.F.S. Andrade, and A.G. Brolo, *A review on the fabrication of substrates for surface enhanced Raman spectroscopy and their applications in analytical chemistry.* Analytica Chimica Acta, 2011. **693**(1-2): p. 7-25.

[2] Yang, P., R. Yan, and M. Fardy, *Semiconductor Nanowire: What's Next?* Nano Letters, 2010. **10**(5): p. 1529-1536.

[3] Mollenstedt, G., *Important problems of the electron microscope*. A. L. Houwink, and B. J. Spit, Editors. The proceedings of the European Regional Conference on Electron Microscopy. 1961. 1-17.

[4] Yamazake, K., *Electron beam direct writing*. Nanofabrication Fundamentals and Applications, ed. A.A. Tseng. Vol. Chapter 10. 2008, Hackensack, NJ: World Scientific.

[5] Pfeiffer, H.C., *VARIABLE SPOT SHAPING FOR ELECTRON-BEAM LITHOGRAPHY.* Journal of Vacuum Science & Technology, 1978. **15**(3): p. 887-890.

[6] Berger, S.D., et al., *PROJECTION ELECTRON-BEAM LITHOGRAPHY - A NEW APPROACH.* Journal of Vacuum Science & Technology B, 1991. **9**(6): p. 2996-2999.

[7] Pfeiffer, H.C. and W. Stickel, *PREVAIL - AN E-BEAM STEPPER WITH VARIABLE AXIS IMMERSION LENSES.* Microelectronic Engineering, 1995. **27**(1-4): p. 143-146.

[8] Utsumi, T., *Low-energy e-beam proximity lithography (LEEPL): Is the simplest the best?* Japanese Journal of Applied Physics Part 1-Regular Papers Short Notes & Review Papers, 1999. **38**(12B): p. 7046-7051.

[9] Saitou, N., *Electron beam lithography - Present and future.* International Journal of the Japan Society for Precision Engineering, 1996. **30**(2): p. 107-111.

[10] Tseng, A.A. and A. Notargiacomo, *Nanoscale fabrication by nonconventional approaches.* Journal of Nanoscience and Nanotechnology, 2005. **5**(5): p. 683-702.

[11] Tennant, D.M., *Limits of Conventional Lithography*. Nanotechnology, ed. G. Timp. Vol. Chapter 4. 1999, New York: Springer.

[12] Namatsu, H., et al., *FABRICATION OF SUB-10-NM SILICON LINES WITH MINIMUM FLUCTUATION.* Journal of Vacuum Science & Technology B, 1995. **13**(4): p. 1473-1476.

[13] Murata, K., D.F. Kyser, and C.H. Ting, *MONTE-CARLO SIMULATION OF FAST SECONDARY-ELECTRON PRODUCTION IN ELECTRON-BEAM RESISTS.* Journal of Applied Physics, 1981. **52**(7): p. 4396-4405.

[14] Gunnarsson, L., et al., *Interparticle coupling effects in nanofabricated substrates for surface-enhanced Raman scattering.* Applied Physics Letters, 2001. **78**(6): p. 802-804.

[15] Yu, Q., et al., *Inverted size-dependence of surface-enhanced Raman scattering on gold nanohole and nanodisk arrays.* Nano Letters, 2008. **8**(7): p. 1923-1928.

[16] Im, H., et al., *Vertically Oriented Sub-10-nm Plasmonic Nanogap Arrays.* Nano Letters, 2010. **10**(6): p. 2231-2236.

[17] Mack, C., *Introduction to Semiconductor Lithography*. Fundamental Principles of Optical Lithography. 2007, Hoboken, NJ: Wiley.

[18] Miller, J.M., *Chromatography: concepts and contrasts*. 2005: John Wiley & Sons.

[19] Mai, T.T., et al., *Dynamics of Wicking in Silicon Nanopillars Fabricated with Interference Lithography and Metal-Assisted Chemical Etching.* Langmuir, 2012. **28**(31): p. 11465-11471.

[20] Bico, J., C. Tordeux, and D. Quéré, *Rough wetting.* EPL (Europhysics Letters), 2001. **55**(2): p. 214.

[21] Sharma, A. and S.G. Schulman, *Introduction to fluorescence spectroscopy*. Vol. 13. 1999: Wiley-Interscience.

[22] Moerner, W. and L. Kador, *Optical detection and spectroscopy of single molecules in a solid.* Physical Review Letters, 1989. **62**(21): p. 2535.

[23] Orrit, M. and J. Bernard, *Single pentacene molecules detected by fluorescence excitation in a p-terphenyl crystal.* Physical Review Letters, 1990. **65**(21): p. 2716.

[24] Betzig, E. and R.J. Chichester, *Single molecules observed by near-field scanning optical microscopy.* Science, 1993. **262**(5138): p. 1422-1425.

[25] Shaner, N.C., P.A. Steinbach, and R.Y. Tsien, *A guide to choosing fluorescent proteins.* Nature methods, 2005. **2**(12): p. 905-909.

[26] Lord, S.J., et al., *Photophysical properties of acene DCDHF fluorophores: Long-wavelength single-molecule emitters designed for cellular imaging.* The Journal of Physical Chemistry A, 2007. **111**(37): p. 8934-8941.

[27] Eisenstein, M., *Protein arrays: growing pains.* Nature, 2006. **444**(7121): p. 959-962.

[28] Combs, C.A., *Fluorescence microscopy: a concise guide to current imaging methods.* Current Protocols in Neuroscience, 2010: p. 2.1. 1-2.1. 14.

[29] Lichtman, J.W. and J.-A. Conchello, *Fluorescence microscopy.* Nature methods, 2005. **2**(12): p. 910-919.

[30] Bányai, L. and S.W. Koch, *Semiconductor quantum dots*. Vol. 2. 1993: World Scientific.

[31] Li, Y., et al., *Nanowire electronic and optoelectronic devices.* Materials today, 2006. **9**(10): p. 18-27.

[32] Yan, R., D. Gargas, and P. Yang, *Nanowire photonics.* Nature Photonics, 2009. **3**(10): p. 569-576.

[33] Greytak, A.B., et al., *Semiconductor nanowire laser and nanowire waveguide electro-optic modulators.* Applied Physics Letters, 2005. **87**(15): p. 151103.

[34] Duan, X., et al., *Single-nanowire electrically driven lasers.* Nature, 2003. **421**(6920): p. 241-245.

[35] Huang, M.H., et al., *Room-temperature ultraviolet nanowire nanolasers.* science, 2001. **292**(5523): p. 1897-1899.

[36] Bao, J., et al., *Broadband ZnO single-nanowire light-emitting diode.* Nano letters, 2006. **6**(8): p. 1719-1722.

[37] Cao, L., et al., *Semiconductor nanowire optical antenna solar absorbers.* Nano letters, 2010. **10**(2): p. 439-445.

[38] Zhu, J., et al., *Optical absorption enhancement in amorphous silicon nanowire and nanocone arrays.* Nano letters, 2008. **9**(1): p. 279-282.

[39] Snyder, A.W. and J. Love, *Optical waveguide theory*. 2012: Springer Science & Business Media.

[40] Cao, L.Y., et al., *Tuning the Color of Silicon Nanostructures.* Nano Letters, 2010. **10**(7): p. 2649-2654.

[41] Cao, L.Y., et al., *Semiconductor Nanowire Optical Antenna Solar Absorbers.* Nano Letters, 2010. **10**(2): p. 439-445.

[42] Cao, L.Y., et al., *Engineering Light Absorption in Semiconductor Nanowire Devices.* Nature Materials, 2009. **8**(8): p. 643-647.

[43] Seo, K., et al., *Multicolored Vertical Silicon Nanowires.* Nano Letters, 2011. **11**(4): p. 1851-1856.

[44] Walker, B.N., et al., *Tailored Silicon Nanopost Arrays for Resonant Nanophotonic Ion Production.* Journal of Physical Chemistry C, 2010. **114**(11): p. 4835-4840.

[45] Bronstrup, G., et al., *Optical Properties of Individual Silicon Nanowires for Photonic Devices.* Acs Nano, 2010. **4**(12): p. 7113-7122.

[46] Cao, L.Y., et al., *Resonant Germanium Nanoantenna Photodetectors.* Nano Letters, 2010. **10**(4): p. 1229-1233.

[47] Muskens, O.L., et al., *Large Photonic Strength of Highly Tunable Resonant Nanowire Materials.* Nano Letters, 2009. **9**(3): p. 930-934.

CHAPTER 5:
WICKING NANOPILLAR ARRAYS WITH DUAL ROUGHNESS FOR SELECTIVE TRANSPORT AND FLUORESCENCE MEASUREMENTS

A version of this chapter was originally published by Jennifer J. Charlton, Nickolay Lavrik, James A. Bradshaw, and Michael J. Sepaniak.

Charlton, J.J., et al., *Wicking Nanopillar Arrays with Dual Roughness for Selective Transport and Fluorescence Measurements.* ACS Applied Materials & Interfaces, 2014. **6**(20): p. 17894-17901.

All changes from the original manuscript are trivial in nature and result from reformatting to conform to standards for a dissertation as required by The University of Tennessee in Knoxville. All of the coauthors contributed intellectual capital.

5.1 Abstract

Silicon nanopillars are important building elements for innovative nanoscale systems with unique optical, wetting, and chemical separation functionalities. However, technologies for creating expansive pillars arrays on the submicron scale are often complex and with practical time, cost, and method limitations. Herein we demonstrate the rapid fabrication of nanopillar arrays using the thermal dewetting of Pt films with thicknesses in the range from 5 to 19 nm followed by anisotropic reactive ion etching (RIE) of the substrate materials. A second level of roughness on the sub-30 nm scale is added by over-coating the silicon nanopillars with a conformal layer of porous silicon oxide (PSO) using room temperature plasma enhanced chemical vapor deposition (PECVD). This technique produced environmentally conscious, economically feasible, expansive nanopillar arrays with a production pathway scalable to industrial demands. The arrays were systematically analyzed for size, density, and variability of the pillar dimensions. We show that these stochastic arrays exhibit rapid wicking of various fluids and, when functionalized with a

physiosorbed layer of silicone oil, act as a superhydrophobic surface. We also demonstrate high brightness fluorescence and selective transport of model dye compounds on surfaces of the implemented nanopillar arrays with two-tier roughness. The demonstrated combination of functionalities creates a platform with attributes inherently important for advanced separations and chemical analysis.

5.2 Introduction

There is a strong demand for high sensitivity platforms for the fluorescence detection of low level and/or low quantum yield samples. Some traditional approaches that can increase the effectiveness of a fluorescence analysis include increasing the intensity of the excitation field and emission collection efficiency, effectively transporting and concentrating an analyte within the area to be analyzed, and isolating from interfering species.[1] Herein we fabricate, and offer a convenient means to optimize, a single multifunctional platform that combines all of these approaches with an emphasis on tailoring nanoscale features. Using silicon nanopillars with vertical sidewall profiles and adding second level roughness via a porous silicon oxide (PSO) coating, we study attributes including wicking, superhydrophobicity, fluorescent brightness, and selective transport that are beneficial in creating a platform for low level fluorescence analysis. Our specific approaches and designs were driven by two main considerations. First, a unique combination of wicking dynamics and superhydrophobicity of these nanostructured surfaces can lead to capillary assisted selective transport, concentration[2,3] and delivery[4-6] of minute quantities of low level samples. Second, appropriately designed silicon nanopillars are known to facilitate enhancement[7,8] and collection of fluorescence

signals.[9] The use of micro and nanoscale pillar arrays have garnished significant attention as a platform for separations in pressure driven microfluidic systems[4-5,10-11] and systems that use electrophoretic pumping.[12] Due to their high surface area and wicking properties[13] pillar arrays are also promising as a platform for capillary driven microfluidic systems that take advantage of the open capillary architecture. When applied to analytical separations, such “open channel” microfluidic systems are anticipated to possess many advantages including the potential for multiplexing separations, capability of orthogonal separation formats, imaging separations without rigorous temporal limitations, as well as the overall simplicity often associated with planar chromatography.[6] These advantages combined with the low sample consumption common to micro and nanofluidic systems open the door to a platform for point-of-care analysis of traditionally difficult and high value samples.[14-17] Many current point-of-care capillary driven devices, such as lateral flow (immuno)assays, use a transport medium of nitrocellulose with pore sizes ranging from 0.05 to about 12 μm that can vary depending on manufacturing and storage conditions (including temperature and humidity). These poorly controlled changes in porosity alter flow dynamics of the substrate and can make it challenging to realize conditions that facilitate transport and allow an optimal reaction time for analysis.[18] Therefore, the main motivation behind the present study is to identify new types of wicking substrates that are free from environmentally induced changes in porosity, wetting, and capillary transport properties and also deterministically tunable as well as practically reproducible.

The remarkably diverse wetting phenomena observed on micro and nano fabricated surface textures[13] range from directional wicking and superwicking[19-31] to super-hydrophobicity and omni-phobicity.[23,28,30,32] Among various classes of previously explored surface nanostructures and nanotextures, silicon pillar arrays have been of our particular attention since they have the potential to combine the unique wetting properties associated with forests of small diameter pillars,[33] as well as unique optical properties associated with optical field enhancements in vicinity of nanoscale cylindrical dielectric resonators.[7-9] In particular, it has been recently shown that resonance enhancement of optical fields on the surface of silicon nanopillars facilitates detection of a small number of fluorescently labelled biological molecules.[8] Arrays of high aspect ratio nanopillars made from materials other than silicon can also provide non-resonance increases in fluorescence brightness and, respectively, improved figures of merit in fluorescence based analytical techniques due to a geometric factor, i.e. substantially increased surface areas.[34] Furthermore, the superhydrophobic properties of pillar arrays can be useful in delivering minute quantities of analytes while overcoming fundamental limitations of more conventional systems when diffusion limited kinetics slows down transport of highly dilute chemical species in ultra-low volumes.[2]

Both the optical resonances[7-8] and the fluid dynamics[33] observed in silicon pillar arrays can be tailored by changing the pillar size, shape, and density. To date, methods to reproducibly fabricate pillars with sub micrometer diameters often involve complex advanced lithography methods[7-8,35] or surface assembly of nanoparticles.[36] While several methods can produce highly ordered arrays of silicon pillars with diameters in the

100 to 500 nm range, most have practical limitations. Electron beam lithography (EBL) is often used to fabricate precisely defined pillar arrays with diameters around 100 nm.[8] The EBL approach requires expensive equipment and is a slow serial process, creating practical limits as to the size and quantity of fabricated arrays. On the other hand, the bottom up approaches such as surface assembly of nanoparticles have the ability to quickly cover large areas creating etch masks suitable for subsequent fabrication of tightly spaced pillar arrays.[36,37] However, these methods lack the ability to reproducibly create variations in the pillar size within the same wafer. Moreover, the use of nanoparticles is of a potential concern because environmental nano-pollutants can pose serious health risks.[38]

In the present study we show that the challenge of creating expansive arrays of silicon nanopillars with average diameters tunable from 100 to 500 nm can be addressed very efficiently through the thermal dewetting of thin Pt films followed by anisotropic reactive ion etching (RIE) of silicon oxide and silicon. Aiming to create substrates with a combination of high surface area and other functionalities important in planar chromatography and trace level analytical fluorescence analysis, we explore room temperature plasma enhanced chemical vapor deposition (PECVD) which allowed us to overcoat the silicon nanopillar arrays with a conformal layer of porous silicon oxide (PSO) and prepare wicking substrates with two-tier roughness.

5.3 Materials and methods

In order to create arrays of approximately circular patterns, we utilized thermally induced dewetting of thin Pt films deposited on silicon surfaces with a thermally grown silicon

dioxide (SiO_2). Nanopillar arrays were formed due to the masking role of Pt islands during reactive ion etching of SiO_2 and silicon as described in our previous work.[39] Subsequently, we analyzed average diameter, standard deviation, average spacing and density of pillars formed on the silicon wafer that had Pt film with original thickness varying from 5 nm to 19 nm. Finally, we create a secondary level of nanoscale roughness through the deposition of a PSO layer on the pillar surface using room temperature PECVD[40-42] and observe the effects this process has on the wicking of silicone oil. Experimentally determined wicking rates of silicone oil and ethanol were also compared to the results to an analytical model developed by Mia et al.[35] based on a widely accepted rough wetting model.[44]

Post silicone oil treatment it is observed that we created a hydrophobic surface with high fluorescent brightness and chemical selectivity with the aim of developing an analytical platform.

5.3.1 Pillar fabrication

As shown in Figure 1, our fabrication sequence started with physical vapor deposition of a Pt film (Thermonics Laboratory, VE-240) on a p-type silicon wafer with 100 nm of thermally grown SiO_2. During the Pt deposition, the deposition rate and the average (mass based) thickness of the deposited metal were monitored with a quartz crystal microbalance while a shutter that separated the metal source and the substrate acted as a mask. This mask was incrementally moved across the silicon wafer in such a way that Pt thickness varied in 1 nm increments from 5 nm to 19 nm across the four inch silicon wafer.

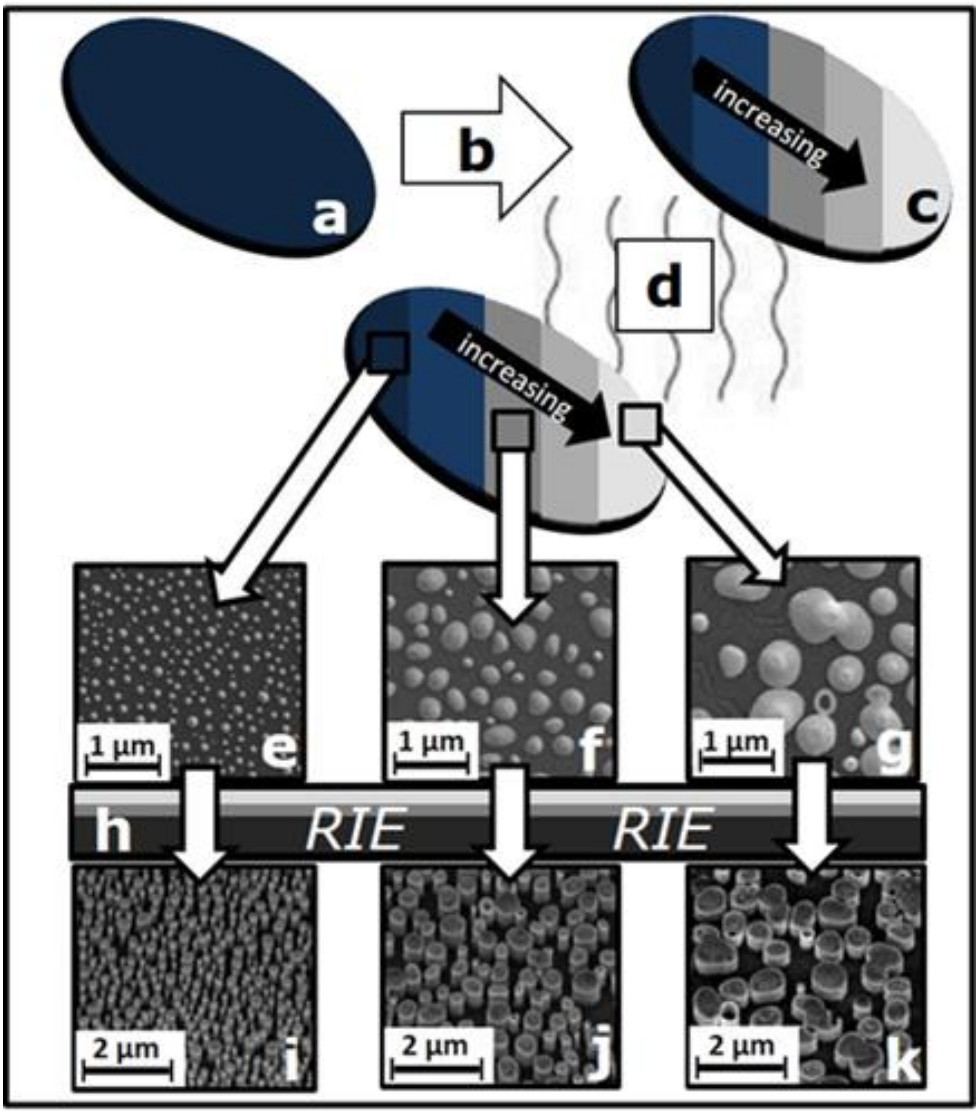

Figure 5.1. Process sequence used to fabricate silicon pillar arrays in the present work. (a) A silicon wafer with 100 nm of thermally grown SiO2 is used as a starting material. (b) Physical vapor deposition of Pt results in regions (c) with varying Pt thicknesses across wafer. (d) Thermal processing in a mixture of argon and hydrogen yields Pt islands. SEM of Pt islands from (e) 5nm, (f) 10 nm, and (g) 17 nm films acting as a mask during subsequent (h) RIE of silicon. SEM of pillar arrays with various morphologies formed after RIE form (i) 5 nm, (j) 10 nm, and (k) 17 nm Pt films.

As a result, as series of distinct 5 mm wide regions for each average thickness of Pt was created on a single wafer. The platinum film was then thermally annealed in a 10:1 mixture of argon and hydrogen at 735 Torr in a cold wall furnace (Easy Tube 3000, First Nano, Ronkonkoma, NY) equipped by a radiative heat source. During the anneal step the heat source was set to its maximum power (22 kW) for 8 s yielding an estimated maximum substrate temperature of 900^{o} C. The thermally induced metal film dewetting created circular masking patterns (see Figure 5.1e). These platinum islands were subsequently used as a selective mask for anisotropic reactive ion etching (Oxford PlasmaLab, Oxford Instruments, UK) of the substrate material as described previously.[39] The resulting 1±0.2 micron tall silicon pillars with the remaining Pt caps are similar to those created via EBL patterning and used as a platform for enhanced fluorescence analysis in our previous work.[7,8] However the pillars that are over coated with the PSO have a conformal material surface.

5.3.2 Functionality studies

The wicking behavior was studied with the pillar arrays inserted vertically into a pool of the liquid, in an open container for the silicone oil and in a sealed vial for the ethanol (190 proof, Decon Labs, Inc.). The wicking progress was captured with a 5.0 MP autofocus camera with LED Flash (LG Optimus F3) at known times. Using Image J software the digital images were scaled based on a known dimension and the z (displacement of the wicking front) was measured from the surface of the wicking liquid to the visible wicking front. Initially, silicone oil (HIVAC F4) was applied and allowed to wick at room temperature until the full wafer was covered the baked at 100^{0} C for 72 hours.

Subsequently, excess oil was removed in a five part wash using successive rinses of ethanol, toluene (Fisher Scientific), THF (Fisher Scientific) 90 % then THF 10% with 18 MΩ deionized water, and finally 18 MΩ deionized water. The substrates rendered hydrophobic after this process were used to study the wicking dynamics of ethanol. The contact angles were found by depositing 2.5 μL of 18 MΩ deionized water on each substrate, and subsequently imaging the drops with the aforementioned camera at 90^{o} from substrate surface. The angle was visually measured by a digitally overlaid protractor. Fluorescence brightness was evaluated by analyzing fluorescence images of the substrates spotted with 2.5 μL drop of 1 x 10 $^{-10}$ M rhodamine 6G in a 90 % water: 10% ethanol solution. Fluorescence images were obtained with a 30 second collection time, a 510-560 nm excitation source and a camera gain of 1.5 (Nikon Ellipse E600 Fluorescence Microscope). For the selective transport analysis, pillars with 96 nm average diameter were overcoated with 25 nm of PSO and spotted with a 1 μL drop of a mixed 1 x 10^{-7} M rhodamine 6G and 1 x 10^{-7} M fluorescein isothiocyanate (FTIC) in 10% ethanol 90 % water and allowed to dry for 48 hours. The spotted array was inserted perpendicular to just below the visible spot into 30% water 70% ethanol solution in a sealed vial and allowed to wick 1 cm past the original spot. The array was immediately removed from the vial and imaged with Nikon Eclipse LV150 microscope using the 5× objective. The microscope was equipped with a halogen lamp light source, a multicolor fluorescence cube (DAPI-FITC-TRITC), and a color CCD camera (DS-2M, Nikon, Inc.) controlled by NIS-Elements software. Fluorescence color (RGB) images with 16-bit color depth per channel were acquired by integrating a sequence of four 8-bit color images.

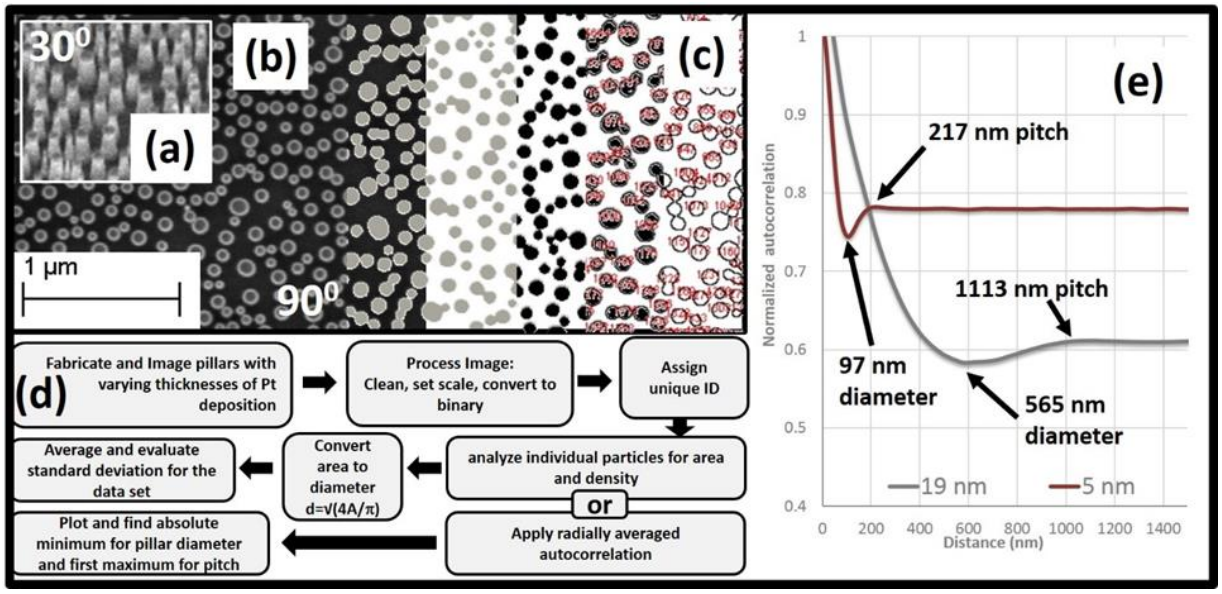

Figure 5.2. (a) SEM image of a silicon pillar array taken at 300 angle. (b) Top view SEM images of a similar array and a sequence of graphics produced from the digital image processing, (c) areas with assigned unique ID, (d) flow diagram of analysis of image to characterize pillar size, dispersity, and density, (e) example plots of radially averaged autocorrelation of the pillars from 5 nm and 19 nm Pt deposition with pitch and diameter clearly shown

5.3.3 Surface analysis

A flat silicon substrate was submerged in silicone oil and baked with a control sample that was not exposed to oil at 100^0 C for 72 hours. The samples were rinsed in various solvents and evaluated via ellipsometry to evaluate their effects on the thickness of the physiosorbed layer of silicon oil. The solvents included the five part (ethanol, toluene, THF, 90THF:10H_2O, H_2O) rinse described previously, acetone, methylene chloride, and trichloroethylene by submerging sample in clean solvent 1 minute repeated three times. Additionally the samples were soaked in water and ethanol for 1 and 24 hours. Ellipsometry was carried at 70° incidence and 635 nm probing wavelength using a UVISEL spectroscopic ellipsometer (Horiba-Jobin Yvon) with the elliptical probing area of 1 mm × 1.5 mm. Ellipsometry data were fitted to a two layer optical model using DeltaPsi2 Software (Horiba Scientific). The model included a silicon substrate, a native oxide, and an organic layer. Optical properties of silicon and silicon dioxide were taken from the DeltaPsi2 material database. We assumed a constant refractive index n = 1.4 for the organic layer.

5.4 Results and discussion

5.4.1 Pillar array morphology

Lee and Kim[45] have shown that surface morphologies of patterns formed as a result of Pt film thermal dewetting, and subsequently used for etching GaN nanostructures, depend on the Pt thickness as well as anneal temperature. More recently, our group has adopted a similar method to fabricate stochastically arranged silicon nanopillars

with a relatively small size dispersity.[39,46]

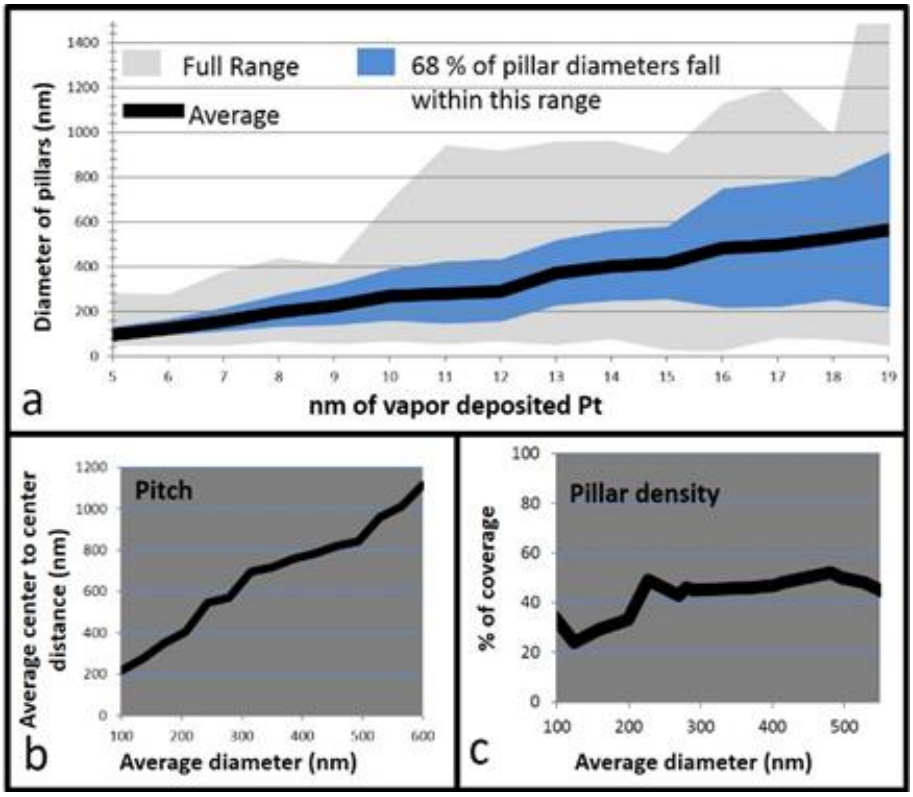

Figure 5.3. (a) The average pillar diameter and the dispersity of the diameters as a function Pt thickness. (b) The average autocorrelation calculated pillar-to-pillar distance (pitch) as a function of average pillar diameter. (c) The fractional coverage of surface occupied by pillars as a function average pillar diameter.

While a single thickness of Pt film[39] was annealed and used as a mask in our previous work, here we explore a range of Pt thicknesses and analyze respective pillar morphologies. Under the given annealing conditions, dewetting of Pt films thinner than 5 nm resulted in circular masking patterns that were too small to produce the targeted 1 micron tall pillars with sufficient mechanical strength. On the other hand, annealing of Pt films thicker than 19 nm led to spinodal dewetting morphologies. At the lower end of the Pt film thickness (5 nm) the average diameter of pillars is 97 nm with a %RSD of 27% and a range from 40 nm to 277 nm. A nearly linear increase in average pillar diameters with the increased Pt thickness is observed. This trend terminates at the higher end of the Pt film thickness (19 nm) with average diameter of 565 nm, a %RSD of 55%, and a range from 40 nm to 2190 nm. The average pillar-to-pillar distance (pitch) also increases with the diameter increase (Figure 5.3b). The pillar fractional coverage is near 50% over nearly the entire range pillar diameters decreasing to approximately 30% at the smaller diameters (Figure 5.3c).

5.4.2 Wicking rate

To evaluate the role the random arrangement of the pillars plays in effecting wicking velocity, our experimentally determined results were compared with wicking velocities predicted by an analytical model for a perfectly ordered pillar arrays. This model is based on averaged geometrical parameters derived through the analysis of the fabricated substrate, experimentally measured solvent-substrate contact angles, and accepted literature values of solvent viscosity and surface tension. Modeled results were compared to the velocities experimentally observed in our system.

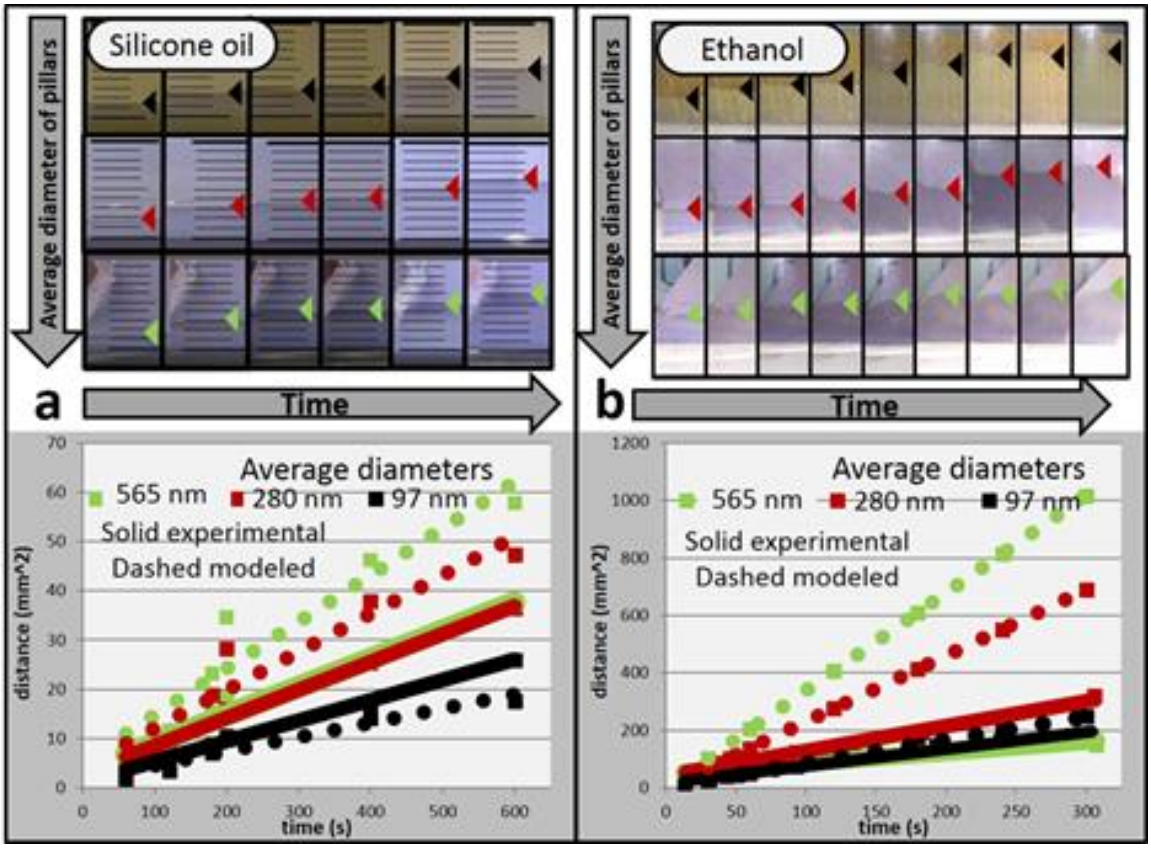

Figure 5.4. Study of the wetting behavior of (a) silicone oil and (b) ethanol on dewetted pillar arrays with average 97, 280, 565 nm diameters compared against an ordered model system.

In particular, we calculated wicking velocities for silicone oil (surface tension γ= 0.0344 N/m, viscosity μ= 0.02375 Pa*s, contact angle θ_{oil}=18^o) and ethanol (γ=0.0224 N/m, μ=0.00107 Pa*s, $\theta_{ethanol}$=22.5^o) using the semi-empirical model developed by Mai et al. for ordered arrays of silicon pillars.[35] The experimentally observed wicking was analyzed and compared with a previously established analytical model using the D coefficient from the well-known diffusive relation

$$D = z^2/t \qquad \text{Eq. 5 1}$$

where z is the displacement of the wicking front and t refers to the time after the start of wicking.

Comparison of the experimentally determined and analytically calculated D values (Figure 5.4) indicates slower wicking in the majority of implemented experimental systems compared to the analytical predictions for analogous perfectly ordered pillar arrays . As can be seen in Figure 5.4a, wicking of silicone oil in the arrays with the average pillar diameter of 97 is the only notable exception from this trend (wicking results for all arrays provided in Supplemental Information). We believe that this phenomenon can be explained based on the law of flow resistance in parallel channels.[47] Specifically, the model is based on a single averaged spacing motif while dewetted pillar arrays are comprised of various channel sizes on both sides of the average. With this in mind, it is reasonable to assume that the liquid flows preferentially through the path of least resistance which, in turn leads to the greater apparent wicking rate. Although nonuniform channel width is a common feature in all the samples studied here regardless of the pillar

diameter, more substantial viscous losses are associated with very tall and dense arrays of pillars.[35] Therefore, a positive effect of non-uniform parallel channels on wicking velocity is likely to be much more pronounced at the lower end of the explored interpillar spacing range.

As shown in Figure 5.4b, the wicking behavior of the much less viscous ethanol follows a similar trend when compared to the modeled values as the silicone oil. The pillar arrays with the 97 nm averaged diameter had a slope similar to the averaged the modeled system. Mai et al.[35] reported a similar trend when wicking water in similar arrays of high aspect ratio nanopillars. They proposed that the divergence was likely due to the deformation of the mechanically weak, high aspect ratio nanopillars caused by capillary forces during the wicking process. We believe additional considerations that can have an effect on the wicking behavior between solvent systems are changes in viscosity and vapor pressure of the liquid. With the lower viscosity the high roughness of the surface does not have as large of a negative effect on the modeled wicking dynamics. Additionally the volatile nature of ethanol, combined with the extremely low fluid volumes (approximately 0.085, 0.087, and 0.093 μL per cm^2 for the 97, 280, and 565 nm averaged diameter systems, respectively), can permit appreciable solvent evaporation during experiments. Even a small percentage of evaporation may significantly reduce the observed displacement of the wicking front. Overall, when compared with an analytical model of the average dimensions of the system, the experimentally observed wicking dynamics of the system are affected by the randomness of the array and this effect diminishes as the %RSD of the pillar diameter decreases.

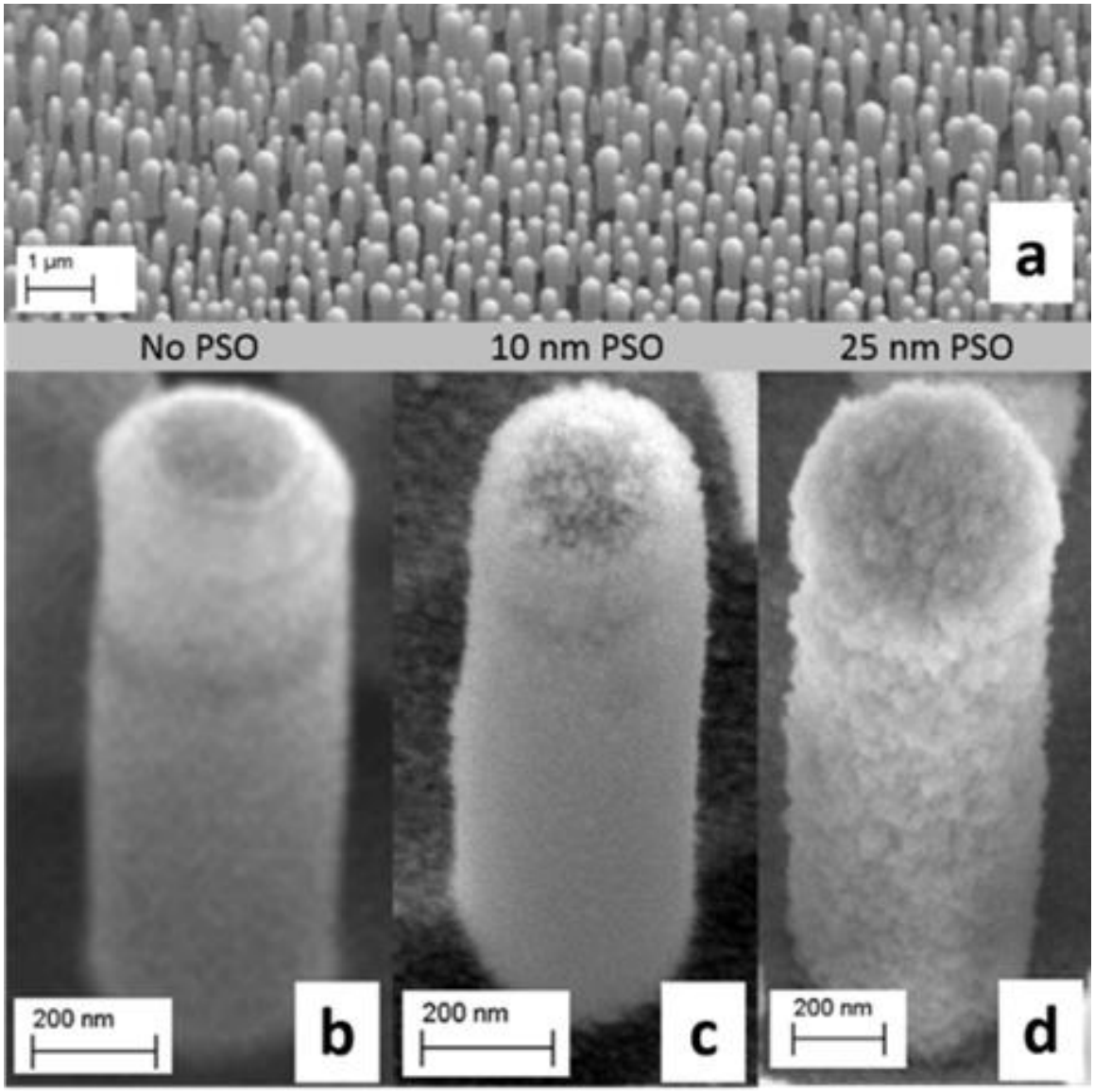

Figure 5.5. (a) Example of expansive pillar array with an average diameter of 270 nm and 10 nm of low temperature PECVD deposited PSO, (b) Approximately 400 nm diameter and 1500 nm tall silicon pillar, (c) with 10 nm PSO, and (d) with 25 nm PSO.

We studied the effect of a secondary roughness on the wicking dynamics of our system. As shown in Figure 5 a-d RIE pillars exhibits a mostly smooth silicon sidewall. Whereas, the pillars deposited with 10 nm of PSO shows slightly enhanced sidewall roughness, and the 25 nm thicknesss of PSO shows a greater degree of side wall roughness. With each system we evaluated the wicking behavior of both silicone oil and ethanol.

As shown in Figure 5.6, an increase in sidewall roughness results in a decrease in wicking velocity. Additionally, the degree to which the wicking velocity is decreased is minimized as the viscosity of the liquid decreases. We feel that these observed decreases in wicking velocity are due to additional viscous loses associated with the enhanced roughness of the pillar sidewall. These trends were observed at all average diameters (additional results found in Supplementary Information).

5.4.3 Superhydrophobicity

Liquid propagation in superhydrophobic micropillar arrays is of significant interest due to unique interfacial phenomena.[31] Recent work has shown that superhydrophobic platforms can be used to concentrate droplets of dilute analyte for SERS and fluorescence detection.[2] This concentrating effect is a result of the droplet remaining in Cassie-Baxter state where the droplet maintains only contact with the tops of the pillars, leaving air underneath during an evaporative process. The point at which the energy barrier that maintains the droplet in the metastable Cassie-Baxter state and external forces reach the same order of magnitude, the transition into the Wenzel state is observed, and the droplet will penetrate the pillar array.[48]

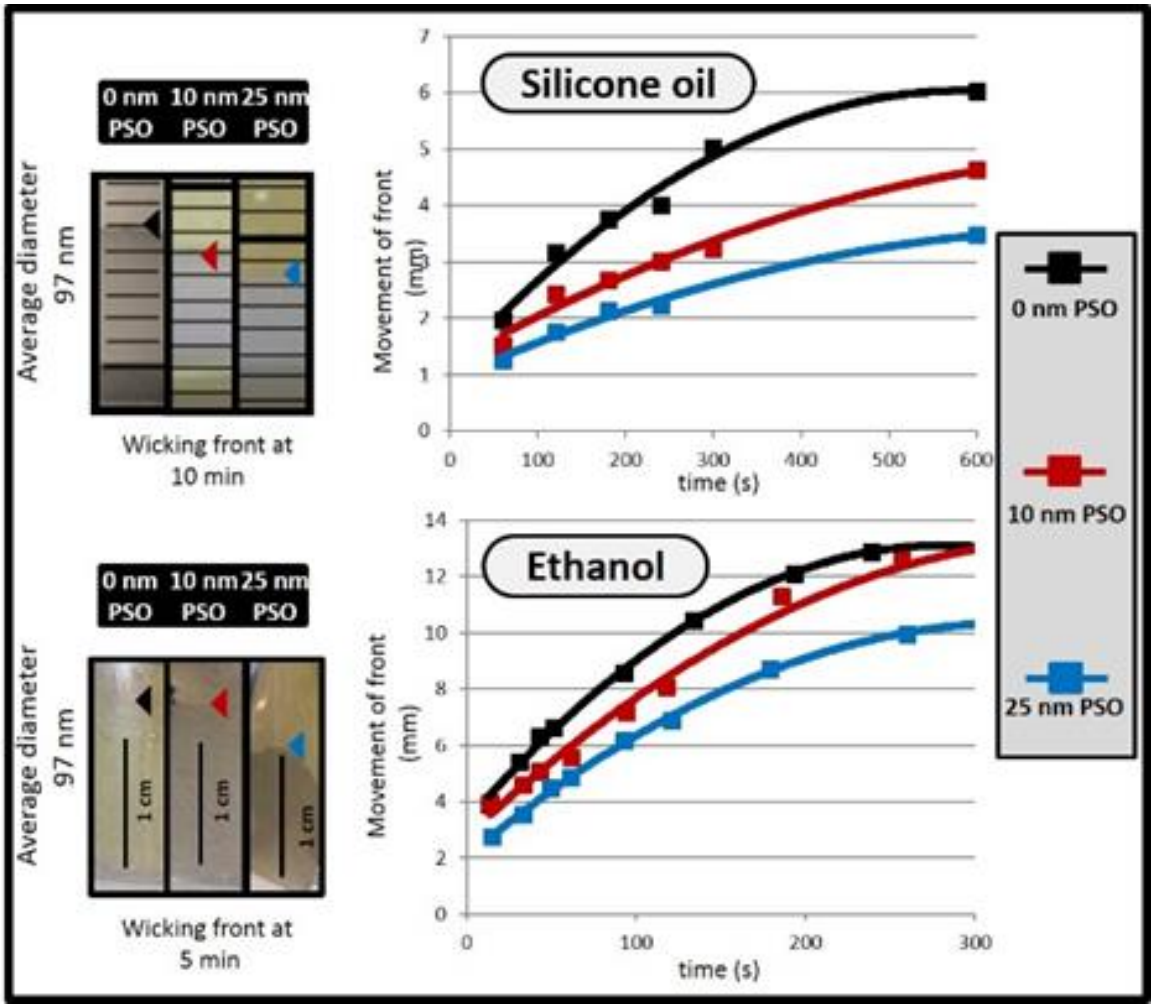

Figure 5.6. Wicking behaviors of silicone oil and ethanol on bare silicon pillar arrays and pillar arrays over coated with 10 nm and 25 nm PSO. Average pillar diameter in the arrays was 97 nm.

It is to be noted this evaporative concentrating effect has been shown to increase localized concentration on the magnitude of 100 fold in the spatially limited area where the Wenzel transition is observed.[3] In order for a substrate to be classified as super hydrophobic the contact angle of a water droplet must be greater than 150˚ and exhibit a roll-off angle less than 10°.[49] The pillar systems used in this work have a dual level

roughness that is traditionally associated with superhydrophobic surfaces,[23,28-30,49] these surfaces are roughed on the microscale for one level and on the nanoscale for the second. The novelty here is that these platforms have both levels of roughness within the nanoscale and still maintain the greater than 150˚ contact angle needed to categorize them as a superhydrophobic substrate. Additionally, we chose to use a unique silicone oil based organic to functionalize the PSO coated pillars. As it was well noted that upon wicking the silicone oil, the pillar arrays exhibited a high degree of hydrophobicity. It is reasonable to assume that a thin layer of the silicone oil led to formation of a textured surface analogous to the bioinspired self-repairing slippery surfaces (SLIPS) introduced by Wong et. al.[32] When evaluating the surface with elipsometry we found that 5.5 nm of thermally grown silicon oxide was created during the curing and baking time. Upon washing with the five part rinse described previously the thickness of the oxide and organic layers were between 11 and 14 nm combined. When triple rinsing with methylene chloride the thickness was similar to the five part rinse between 11 and 14 nm. Using the harsher chlorinated solvent trichloroethylene the oxide and organic layer was reduced to between 9 and 10 nm. By contrast, with less harsh solvent systems such as acetone and extended soaks in water and ethanol the samples were very uninform and the elipsometry measurements ranged from 20 to 40 within each sample. As shown in Figure 7a, a smooth silicon surface successively exposed to the silicone oil and washed had a contact angle of 50^{o}. However, pillar arrays with average diameters of 280 nm exposed to silicone oil exhibited a contact angle of 115^{o}. Even higher contact angles with values approaching those characteristic of the super-hydrophobic state with small contact angle

hysteresis is observed only on pillars additionally modified with PSO to produce a dual level roughened surface.[28] At the secondary roughness from a 10 nm deposition of PSO the angle is 140^{o} and at 25 nm of PSO we enter the super-hydrophobic range with a 155^{o} contact angle. The trend was similar at all of the pillar diameters.

5.4.4 High brightness

The substrate evaluated herein was developed with the goal of creating an easily fabricated expansive platform for surface fluorescent analysis. With this in mind we tailored our synthesis based on known attributes that would create an environment to maximize the brightness of a fluorescence sample. In addition to aforementioned analyte concentration effects associated with the super hydrophobic surface, one must consider the properties of added surface area as well as optical effects associated with silicon and silicon oxide. It has been shown in previous work that silicon pillars at or near 100 nm can produce an enhanced field and subsequently an increase in fluorescent brightness over a background.[8] This enhanced field effect is tunable by pillar size allowing enhancement selective spectral signals based on wavelength.[7] Other than field effects it has been shown that fluorescence brightness can scale with increased surface area by allowing increased sample concentrations on the surface within the limited field of view of the collection platform.[34] The nanopillars as well as the PSO play an important role of adding additional surface area. Finally the highly reflective nature of SiO_2 can add to the increased brightness due to constructive interference of the reflected incident and fluorescence signals[9] as well as reflecting signals with an initial direction away from the collection platform a more fortuitous path toward the collecting optics. When comparing

spots of similar size and concentration of rhodamine 6G, it is noted that (Figure 5.7b) the spot on the flat silicon and the pillars without PSO are of similar fluorescence brightness. However, high brightness of the pillars with the PSO was readily visualized and increased as the deposition thickness of PSO increased. We used imageJ software to quantify the brightness. The average brightness of the pillars with 10 nm PSO was 2.0 times and 25 nm PSO was 3.8 times that of the pillars without the PSO. This increased brightness may be attributed to several factors. We believe the increase in brightness is caused by the increased surface area of the PSO coated pillars as well as the reflective nature of SiO_2. The increased brightness with increased PSO deposition was observed at all pillar diameters.

5.4.5 Selective transport

The innate wicking, high brightness, and super-hydrophobic properties demonstrated for the silicone oil functionalized surface of the pillar arrays with 25 nm PSO, led to testing the array for selective compound transport as fluorescence analysis is known for its broad spectral nature and the ability to isolate compounds would increase the selectivity of any method developed for use with this platform. Selective transport of compounds is based on the likely hood of chemically induced interactions of the analyte with the substrate. These interactions would allow for the selective analysis of a single compound while removing interfering species that cause increases in background fluorescence. As shown in Figure 5.7e**,** the array experienced greater selective interactions with Rhodamine with a retardation factor of 0.70 as evidenced by its lesser transport down the array. The FITC had a retardation factor of 0.82, a similar trend to traditional reverse phase TLC.

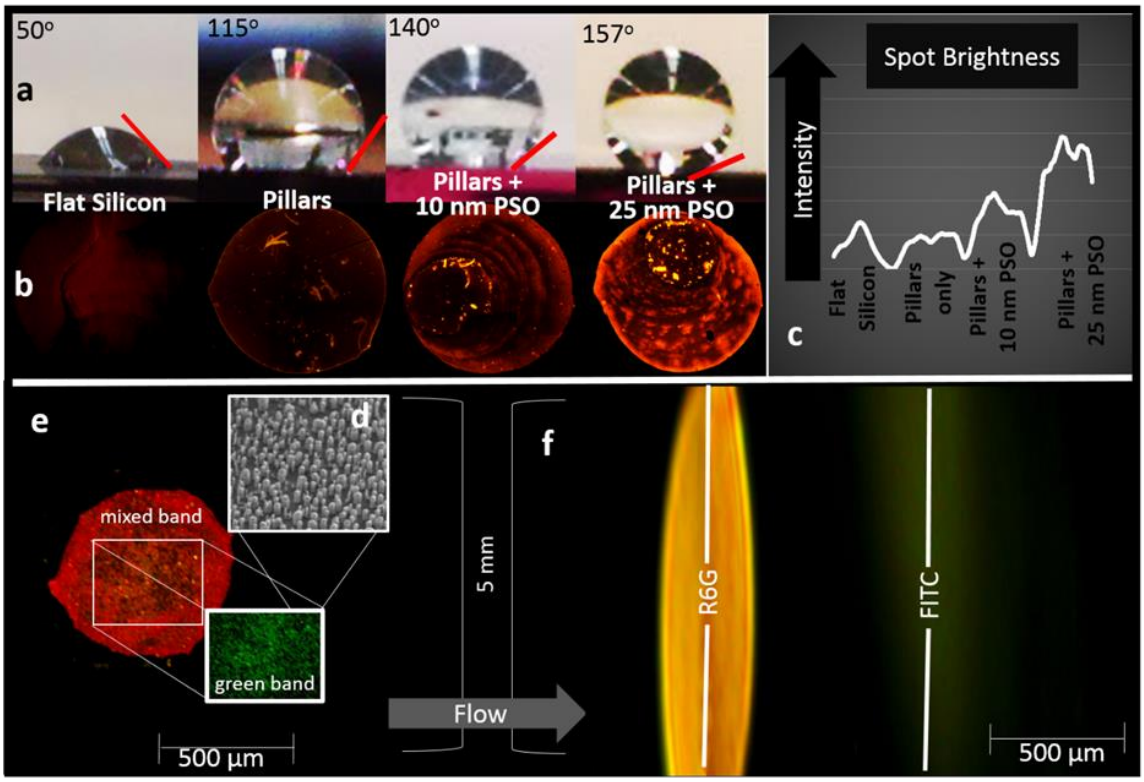

Figure 5.7. (a) Contact angle of 18 MΩ deionized water on silicone oil treated and washed flat silicon, array of silicon nanopillars with 280 nm average diameters, and similar nanopillar arrays with 10 and 25 nm of PSO deposited on the surface, (b) fluorescent spots of 1 x 10^{-10} M rhodamine 6G on each substrate, (c) fluorescence intensity for each sample, (d) SEM of dewetted pillar array, (e) FITC/rhodamine 6G mixed spot before wicking ethanol (f) substrate showing greater selective interactions with rhodamine 6G over FITC.

This selective transport is important in the development of new platforms for open platform separations.[7]

5.5 Conclusions

In summary, we demonstrate the straightforward processing of expansive stochastic nanoscale pillars via Pt dewetting, dry etching, and PECVD of PSO with relative ease, cost considerations, and environmental soundness. Advantages of the implemented arrays include easily tunable inter- and intra-wafer average pillar diameters, dual level tunable roughness, rapid solvent wicking, super-hydrophobicity, chemically selective transport, as well as the ability to promote high florescence brightness. These features, make the nanopillar arrays discussed herein, especially attractive for analytical methods and offer a pathway for the large scale production of substrates for use in separations of select compounds with florescence signal detection.

5.6 Author information

5.6.1 Corresponding author

[1]*E-mail: msepaniak@utk.edu, [3]*E-mail: lavriknv@ornl.gov

5.7 Acknowledgements

This research was conducted at the Center for Nanophase Materials Sciences, which is sponsored at Oak Ridge National Laboratory by the Scientific User Facilities Division, Office of Basic Energy Sciences, U.S. Department of Energy. This material is based on work supported in part by the National Science Foundation under Grant CHE-1144947 with the University of Tennessee. This work was supported in part by the Y-12 National

Security Complex Plant Directed Research and Development fund.

5.8 Supporting information

A large part of this work focused on fabricating and characterization of pillars created by the thermal dewetting of a Pt film with varying thicknesses, as differing pillars sizes have differing capabilities. The smaller end of the range with cylindrical silicon pillars around 100 nm have been shown to give an optical enhancement in the visible spectrum of fluorescence compounds.[8] While this may seem optimal when evaluating assays or direct fluorescent of analytes, pillars these slender high aspect ratio pillars are very fragile and easily damaged. We focus our functionality studies on the sturdier pillars with large larger diameters that are less likely to be easily damaged thus more apt to be used at in the field or point of care. These pillars when over coated with PSO and exposed to a wicked silicone oil[32] show the increased brightness, chemical selectivity, solvent wicking capability, and super-hydrophobicity.

Wicking of silicone oil was evaluated with pillars etched form 5, 7, 9, 11, 13, 15, 17, and 19 nm of Pt with no PSO layer. As shown in Figure 5.9 all of the substrates what were evaluated wicked the silicon oil with the most efficient wicking with pillars made with 15 nm Pt deposition with 415 average diameters and 842 average pitches. Most of the remaining pillar arrays performed similar but slightly below the 15 nm Pt-based pillars, except the highly roughened pillars made with 5 nm Pt with an average diameter of 97 nm and an average pitch of 223; where the viscous losses were expected to be very high. The remaining silicon oil wicking studies with layers of PSO and all of the ethanol studies

with and without PSO were conducted with pillars by the thermal dewetting of Pt with 5, 11, and 19 nm of Pt. The results for the smaller diameter arrays are within the main body of work. The remaining results are shown in Figure S-3. While the wicking velocity is decreased when the PSO is added to the pillar arrays the tradeoffs include the added functionalities of high brightness to increase raw signal of fluorescent compound, chemical selectivity to separate the components of mixtures which otherwise may exhibit interferences, and super-hydrophobicity to overcome diffusion limited kinetics and concentrate analytes in a small spot.

Table 5.3. Results of substrate analysis.

Deposition of Pt (nm)	*Average pillar diameter (nm)*	*%rsd*	*% of area covered with pillars*	*Number of pillars evaluated*	*Range from smallest to largest pillars (nm)*	*Average Pitch (nm)*
5	97	28%	34%	1834	236	217
6	124	29%	24%	1500	234	275
7	158	34%	29%	1126	337	349
8	199	37%	33%	774	377	403
9	227	41%	49%	855	362	543
10	270	42%	43%	545	641	569
11	280	51%	46%	973	902	694
12	290	49%	45%	953	865	715
13	370	40%	46%	516	924	756
14	403	39%	47%	532	901	783
15	415	40%	48%	541	869	819
16	482	64%	52%	196	921	840
17	496	54%	50%	147	926	961
18	527	53%	48%	334	927	1012
19	565	55%	43%	622	1042	1113

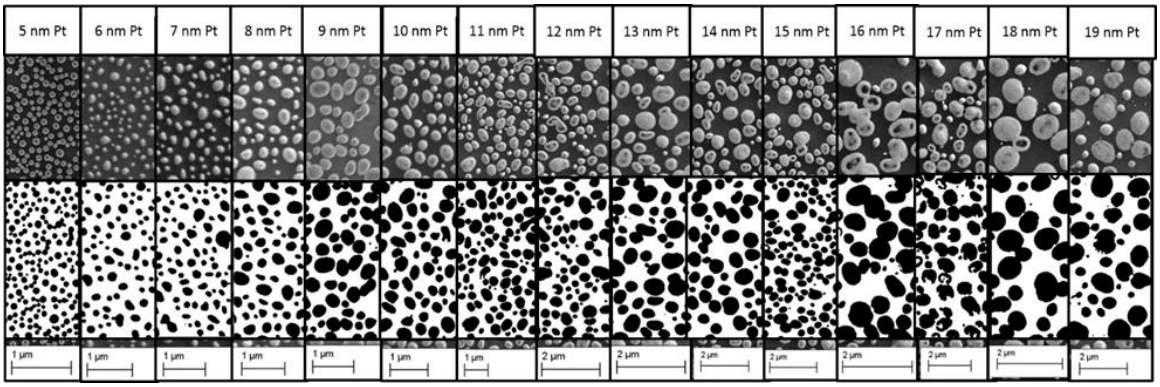

Figure 5.8. SEM images of pillars fabricated from each 5 thru19 nm of Pt.

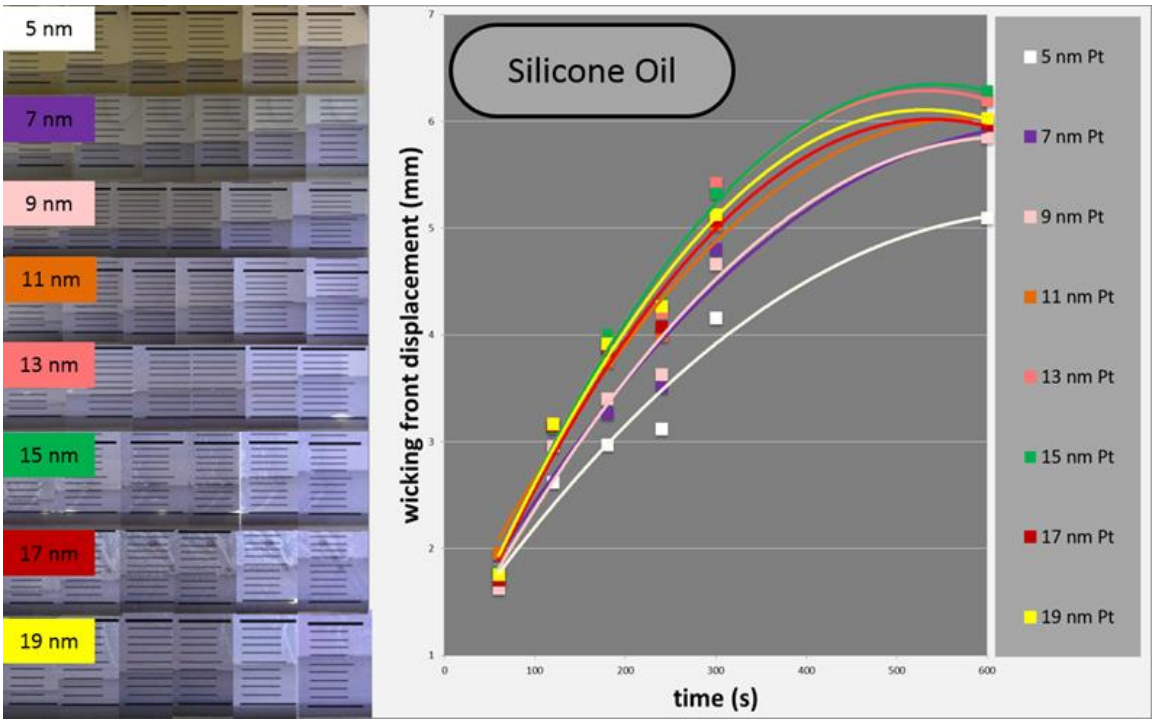

Figure 5.9. Images and chart of advancing wicking front with silicone oil on stochastic nanopillar arrays created with 5, 7, 9, 11, 13, 15, 17, and 19 nm of Pt.

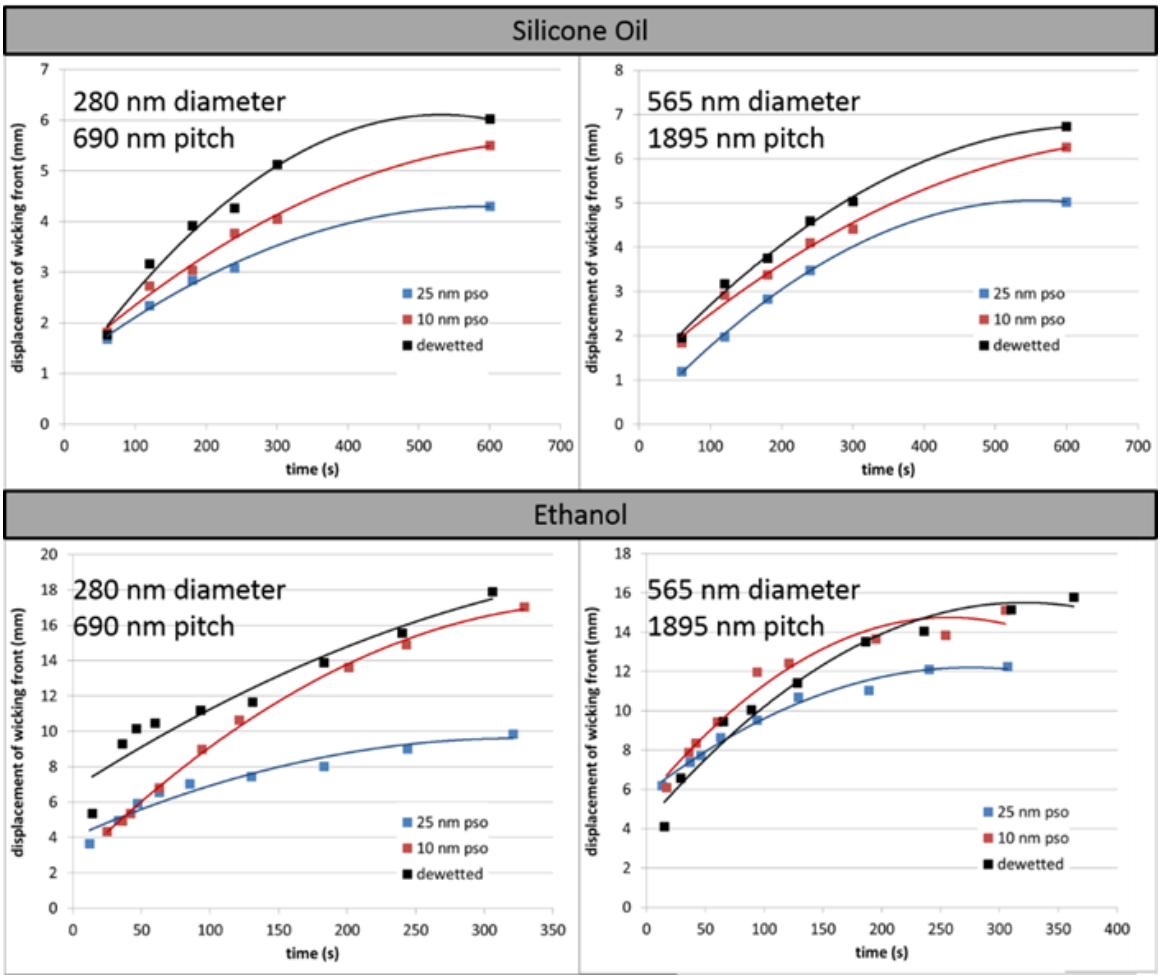

Figure 5.10. Wicking dynamics of both silicone oil and ethanol for stochastic nanopillar arrays with average diameters of 280 and 565 nm with 0, 10, and 25 nm of PSO.

5.9 References

[1] Demchenko, A. P. *Introduction to Fluorescence Sensing*; Springer Publishing. New York City, NY, **2009**.

[2] De Angelis, F.; Gentile, F.; Mecarini, F.; Das, G.; Moretti, M.; Candeloro, P.; Coluccio, M.; Cojoc, G.; Accardo, A.; Liberale, C., Breaking the Diffusion Limit with Super-Hydrophobic Delivery of Molecules to Plasmonic Nanofocusing SERS Structures. *Nat. Photonics* **2011**, 5, 682-687.

[3] Wallace, R.; Charlton, J.; Kirchner, T.; Lavrik, N.; Sepanaik, M., Superhydrophobic Analyte Concentration Utilizing Colloid-Pillar Array SERS Substrates. *Anal. Chem.***2014** (in submission)

[4] Lavrik, N. V.; Taylor, L. T.; Sepaniak, M. J., Nanotechnology and Chip Level Systems for Pressure Driven Liquid Chromatography and Emerging Analytical Separation Techniques: A Review. *Anal. Chim. Acta* **2011,** *694*, 6-20.

[5] Taylor, L. C.; Lavrik, N. V.; Sepaniak, M. J., High-Aspect-Ratio, Silicon Oxide-Enclosed Pillar Structures in Microfluidic Liquid Chromatography. *Anal. Chem.* **2010**, 82, 9549-9556.

[6] Kirchner, T. B.; Hatab, N. A.; Lavrik, N. V.; Sepaniak, M. J., Highly Ordered Silicon Pillar Arrays As Platforms for Planar Chromatography. *Anal. Chem.* **2013**, 85, 11802-11808.

[7] Wells, S. M.; Merkulov, I. A.; Kravchenko, I. I.; Lavrik, N. V.; Sepaniak, M. J., Silicon Nanopillars for Field-Enhanced Surface Spectroscopy. *ACS Nano.* **2012**, 6, 2948-2959.

[8] Kandziolka, M.; Charlton, J. J.; Kravchenko, I. I.; Bradshaw, J. A.; Merkulov, I. A.; Sepaniak, M. J.; Lavrik, N. V., Silicon Nanopillars as a Platform for Enhanced Fluorescence Analysis. *Anal. Chem.* **2013**, 85, 9031-9038.

[9] Choudhury, B. D.; Casquel, R.; Bañuls, M. J.; Sanza, F. J.; Laguna, M. F.; Holgado, M.; Puchades, R.; Maquieira, A.; Barrios, C. A.; Anand, S., Silicon Nanopillar Arrays with SiO2 Overlayer for Biosensing Application. *Opt. Mater. Express*. **2014**, 4, 1345-1354.

[10] De Malsche, W.; Eghbali, H.; Clicq, D.; Vangelooven, J.; Gardeniers, H.; Desmet, G., Pressure-Driven Reverse-Phase Liquid Chromatography Separations in Ordered Nonporous Pillar Array Columns. *Anal. Chem.* **2007,** *79*, 5915-5926.

[11] Mery, E.; Ricoul, F.; Sarrut, N.; Constantin, O.; Delapierre, G.; Garin, J.; Vinet, F., A Silicon Microfluidic Chip Integrating an Ordered Micropillar Array Separation

Column and a Nano-Electrospray Emitter for LC/MS Analysis of Peptides. *Sens. Actuators, B* **2008,** *134*, 438-446.

[12] Chan, Y. C.; Zohar, Y.; Lee, Y.-K., Effects of Embedded Sub-Micron Pillar Arrays in Microfluidic Channels on Large DNA Electrophoresis. *Electrophoresis* **2009,** *30*, 3242-3249.

[13] Quéré, D., Wetting and Roughness. *Annu. Rev. Mater. Res.* **2008,** *38*, 71-99.

[14] Diercks, A. H.; Ozinsky, A.; Hansen, C. L.; Spotts, J. M.; David, J. R.; Aderem, A., A Microfluidic Device for Multiplexed Protien Detection in Nano-Liter Volumes. *Anal. Biochem.* **2008,** *2009*, 30-35.

[15] Chin, C.; Laksanasopin, T.; Cheung, Y.; Steinmiller, D.; Linder, V.; Parsa, H.; Wang, J.; Moore, H.; Rouser, R.; Umiviligihozo, G.; Katrita, E.; Mwambarangwe, L.; Braustien, S.; Wijgert, J.; Sahabo, R.; Justman, J.; El-Sadr, W.; Sia, S., Microfluidics-Based Diagnostics of Infectious Diseases in the Developing World. *Nat. Med.* **2011,** *17*.

[16] Zhang, F.; Turgeon, N.; Toulouse, M.; Duchaine, C.; Li, D., A Simple and Rapid Fluorescent Neuraminindase Enzymatic Assay on a Microfluidic Chip. *Diagn. Microbiol. Infect. Dis.* **2012**, 74, 263-6.

[17] Green, J.; Sun, D.; Hafezi-Moghadam, A.; Lashkari, K.; Murthy, S., Microfluidic Pillar Array Sandwich Immunofluorescence Assay for Ocular Diagnostics. *Biomed. Microdevices*. **2011**, *13*, 573-83.

[18] Posthuma-Trumpie, G. A.; Korf, J.; van Amerongen, A., Lateral Flow (Immuno) Assay: its Strengths, Weaknesses, Opportunities and Threats. A Literature Survey. *Anal. Bioanal. Chem.* **2009,** *393*, 569-582.

[19] Chu, K.-H.; Xiao, R.; Wang, E. N., Uni-Directional Liquid Spreading on Asymmetric Nanostructured Surfaces. *Nat. Mater.* **2010,** *9*, 413-417.

[20] Xia, D.; Johnson, L. M.; López, G. P., Anisotropic Wetting Surfaces with One-Dimesional and Directional Structures: Fabrication Approaches, Wetting Properties and Potential Applications. *Adv. Mater.* **2012,** *24*, 1287-1302.

[21] Vorobyev, A. Y.; Guo, C., Laser Turns Silicon Superwicking. *Opt. Express* **2010,** *18*, 6455-6460.

[22] Vorobyev, A. Y.; Guo, C., Metal Pumps Liquid Uphill. *Appl. Phys. Lett.* **2009,** *94,* 224102.

[23] Callies, M.; Chen, Y.; Marty, F.; Pépin, A.; Quéré, D., Microfabricated Textured Surfaces for Super-Hydrophobicity Investigations. *Microelectron. Eng.* **2005,** *79*, 100-105.

[24] Chen, Y.; Melvin, L. S.; Rodriguez, S.; Bell, D.; Weislogel, M. M., Capillary Driven Flow in Micro Scale Surface Structures. *Microelectron. Eng.* **2009,** *86*, 1317-1320.

[25] Courbin, L.; Denieul, E.; Dressaire, E.; Roper, M.; Ajdari, A.; Stone, H. A., Imbibition by Polygonal Spreading on Microdecorated Surfaces. *Nat. Mater.* **2007,** *6*, 661-664.

[26] Ding, C.; Bogorzi, Srivastava, N.; Sigurdson, M.; Meinhart, C.; MacDonald, N., Super Wetting of Micro and Nano Structured Titania Surfaces, Conference Paper from The 15th International Conference on Solid-State Sensors, Actuators and Microsystems: Transducers 2009, Denver, Colorado USA, June 21 - 25, 2009.

[27] Jokinen, V.; Franssila, S., Capillarity in Microfluidic Channels with Hydrophilic and Hydrophobic Walls. *Microfluid. Nanofluid.* **2008,** *5*, 443-448.

[28] Kim, T.-Y.; Ingmar, B.; Bewilogua, K.; Oh, K. H.; Lee, K.-R., Wetting Behaviours of a-C:H:Si:O Film Coated Nano-Scale Dual Rough Surface. *Chem. Phys. Lett.* **2007,** *436*, 199-203.

[29] Rafiee, J.; Rafiee, M. A.; Yu, Z.-Z.; Koratkar, N., Superhydrophobic to Superhydrophilic Wetting Control in Graphene Films. *Adv. Mater.* **2010,** *22*, 2151-2154.

[30] Wang, M.-F.; Raghunathan, N.; Ziaie, B., A Nonlithographic Top-Down Electrochemical Approach for Creating Hierarchical (Micro−Nano) Superhydrophobic Silicon Surfaces. *Langmuir* **2007,** *23*, 2300-2303.

[31] Xiao, R.; Enright, R.; Wang, E. N., Prediction and Optimization of Liquid Propagation in Micropillar Arrays. *Langmuir* **2010,** *26*, 15070-15075.

[32] Wong, T.-S.; Kang, S. H.; Tang, S. K.; Smythe, E. J.; Hatton, B. D.; Grinthal, A.; Aizenberg, J., Bioinspired Self-Repairing Slippery Surfaces with Pressure-Stable Omniphobicity. *Nature* **2011,** *477*, 443-447.

[33] Ishino, C.; Reyssat, M.; Reyssat, E.; Okumura, K.; Quéré, D., Wicking Within Forests of Micropillars. *Europhys. Lett.* **2007,** *79*, 56005.

[34] Suzuki, Y.; Yokoyama, K., Construction of a More Sensitive Fluorescence Sensing Material for the Detection of Vascular Endothelial Growth Factor, a Biomarker for Angiogenesis, Prepared by Combining a Fluorescent Peptide and a Nanopillar Substrate. *Biosens. Bioelectron.* **2011,** *26*, 3696-3699.

[35] Mai, T. T.; Lai, C. Q.; Zheng, H.; Balasubramanian, K.; Leong, K. C.; Lee, P. S.; Lee, C.; Choi, W. K., Dynamics of Wicking in Silicon Nanopillars Fabricated with Interference Lithography and Metal-Assisted Chemical Etching. *Langmuir* **2012,** *28*, 11465-11471.

[36] Huang, Z.; Fang, H.; Zhu, J., Fabrication of Silicon Nanowire Arrays with Controlled Diameter, Length, and Density. *Adv. Mater.* **2007,** *19*, 744-748.

[37] Hsu, C.-M.; Connor, S. T.; Tang, M. X.; Cui, Y., Wafer-Scale Silicon Nanopillars and Nanocones by Langmuir–Blodgett Assembly and Etching. *Appl. Phys. Lett.* **2008,** *93*.

[38] Reijnders, L., Cleaner Nanotechnology and Hazard Reduction of Manufactured Nanoparticles. *J. Cleaner Prod.* **2006,** *14*, 124-133.

[39] Agapov, R.; Bernadeta, S.; Chris, F.; Dayrl, B.; Nickolay, V. L.; Michael, J. S., Lithography-Free Approach to Highly Efficient, Scalable SERS Substrates Based on Disordered Clusters of Disc-on-Pillar Structures. *Nanotechnology* **2013,** *24*, 505302.

[40] Batey, J.; Tierney, E., Low-Temperature Deposition of High-Quality Silicon Dioxide by Plasma-Enhanced Chemical Vapor Deposition. *J. Appl. Phys.* **1986,** *60*, 3136-3145.

[41] Ceiler, M.; Kohl, P.; Bidstrup, S., Plasma-Enhanced Chemical Vapor Deposition of Silicon Dioxide Deposited at Low Temperatures. *J. Electrochem. Soc.* **1995,** *142*, 2067-2071.

[42] Borrás, A.; Barranco, A.; González-Elipe, A. R., Design and Control of Porosity in Oxide Thin Films Grown by PECVD. *J. Mater. Sci.* **2006,** *41*, 5220-5226.

[43] Wang, D.; Ji, R.; Schaaf, P., Formation of Precise 2D Au Particle Arrays Via Thermally Induced Dewetting on Pre-Patterened Substrates. *Beilstein J. Nanotechnol.* **2011**, 2, 318-326

[44] Bico, J.; Tordeux, C.; Quéré, D., Rough Wetting. *Europhys. Lett.* **2001,** *55*, 214.

[45] Lee, J.-M.; Kim, B.-I., Thermal Dewetting of Pt Thin Film: Etch-Masks for the Fabrication of Semiconductor Nanostructures. *Mater. Sci. Eng.: A* **2007,** *449*, 769-773.

[46] Agapov, R. L.; Boreyko, J. B.; Briggs, D. P.; Srijanto, B. R.; Retterer, S. T.; Collier, C. P.; Lavrik, N. V., Asymmetric Wettability of Nanostructures Directs Leidenfrost Droplets. *ACS Nano* **2013,** *8*, 860-867.

[47] Reynolds, O., An Experimental Investigation of the Circumstances which Determine Whether the Motion of Water Shall be Direct or Sinuous, and of the Law of Resistance in Parallel Channels. *Proceedings of the royal society of London* **1883,** *35*, 84-99.

[48] Murakami, D.; Jinnai, H.; Takahara, A., Wetting Transition from the Cassie−Baxter State to the Wenzel Stateon Textured Polymer Surfaces. *Langmuir,* **2014**, 30, 2061-6067.

[49] Kang, S.; Hwang, S.; Jin, S.; Choi, C.; Kim, J.; Park, B., A Rapid One-Step Fabrication of Patternable Superhydrophobic Surfaces Driven by Marangoni Instability. *Langmuir,* **2014**, 30, 2828-2834.

CHAPTER 6:
SILICON NANOPILLARS AS A PLATFORM FOR ENHANCED FLUORESCENCE ANALYSIS

A version of this chapter was originally published by Michael Kandziolka, Jennifer J. Charlton, Ivan I. Kravchenko, James A. Bradshaw, Igor A. Merkulov, Michael J. Sepaniak, Nickolay V. Lavrik.

Kandziolka, M., et al., *Silicon Nanopillars As a Platform for Enhanced Fluorescence Analysis.* Analytical Chemistry, 2013. **85**(19): p. 9031-9038.

All changes from the original manuscript are trivial in nature and result from reformatting to conform to standards for a dissertation as required by The University of Tennessee in Knoxville. All laboratory work that is presented in this chapter was conducted by Michael Kandziolka as part of an undergraduate research appointment at the Center for Nanophase Material Sciences. As the corresponding author, Nikolay Lavrik contributed much of the fabrication of the pillar arrays as well as sections of the introductory and discussion text. Ivan I. Kravchenko contributed with electron beam lithography. The remaining coauthors contributed intellectual capital.

6.1 Abstract

The importance of fluorescent detection in many fields is well established. While advancements in instrumentation and the development of brighter fluorophore have increased sensitivity and lowered the detection limits of the method, additional gains can be made by manipulating the local electromagnetic field. Herein we take advantage of silicon nanopillars that exhibit optical resonances and field enhancement on their surfaces and demonstrate their potential in improving performance of biomolecular fluorescent assays. We use electron beam lithography and wafer scale processes to create silicon nanoscale pillars with dimensions that can be tuned to maximize fluorescence

enhancement in a particular spectral region. Performance of the nanopillar based fluorescent assay was quantified using two model bioaffinity systems (biotinstreptavidin and immunoglobulin G-antibody) as well as covalent binding of fluorescently tagged bovine serum albumin (BSA). The effects of pillar geometry and number of pillars in arrays were evaluated. Color specific and pillar diameter dependent enhancement of fluorescent signals is clearly demonstrated using green and red labels (FITC, DyLight 488, Alexa 568, and Alexa 596). The ratios of the on pillar to off pillar signals normalized by the nominal increase in surface area due to nanopillars were found to be 43, 75, and 292 for the IgG-antibody assay, streptavidin-biotin system, and covalently attached BSA, respectively. Applicability of the presented approaches to the detection of small numbers of molecules was evaluated using highly diluted labeled proteins and also control experiments without biospecific analytes. Our analysis indicates that detection of fewer than 10 tagged proteins is possible.

6.2 Introduction

Fluorescence spectroscopy and imaging techniques continue to be of critical importance to analytical chemistry, biochemisty, molecular biology, and nanobiotechnology. Fluorescence provides a platform for analysis of a large number of bacterial, viral, and fungal infections, autoimmune diseases, and cancer markers as well as the bioimaging of tissue samples.[1-8] Versatility, noninvasiveness, and single molecule capability are key advantages of fluorescence based assays and imaging.[9] Over the past decade, fluorescence methods have been successfully applied to the inherent low volumes and concentrations typical of single cell analysis.[10,11] Combined with a microfluidic

platform, fluorescent immunoassays have recently achieved single digit picogram/milliliter detection limits[12] significantly improving point-of-care analysis of traditionally difficult and high value samples.[7,8,10,12] Feasibility of on-chip optical detection,[13] lens components,[14] and analysis of complex bioanalytical systems{15] further support an optimistic outlook of the future of the field.

While limits of detection and sensitivity of fluorescence based techniques have already been greatly improved due to advances in confocal microscopy and brighter fluorophores, additional and substantial gains can be achieved by manipulating and controlling the local electromagnetic (EM) field in the vicinity of fluorophores.[15-21]

From a practical point of view, the idea of controlling the EM environment of fluorescence based biological assays is 2-fold: (i) maximize the amount of light collected from each fluorophore molecule and (ii) reduce unwanted background. Each of these functionalities can be implemented using several distinct fundamental principles and optical designs. For instance, noble metal nanostructures that exhibit localized plasmon resonance (LSPR) coupled to fluorophore can lead to highly enhanced optical fields[22] as well as changes in radiative decay rates.[23] These two phenomena, in turn, result in strongly enhanced fluorescence commonly referred to as surface enhanced fluorescence (SEF). Enhanced fluorescence can also be achieved by the use of interference effects in thin films,[17,18] gratings,[19] and optical cavities. Alternatively, nanoscale apertures, such as in zero mode waveguide (ZMW) structures[24,25] enable nanoscale confinement of the excitation volume and provide dramatic reduction of the background in crowded environments. While both plasmonic structures and ZMWs have been extensively

explored and successfully applied to biomolecular fluorescent analysis and imaging at the single molecule level, alternative optical designs may lead to additional advantages. Metal capped vertical SiO_2 nanopillars, for example, enable subwavelength confinement of the probing light analogous to ZMW while providing an extra advantage when a protrusion above the substrate surface is desired.[20] Another promising concept applicable to advanced fluorescence measurements is the use of semiconductor nanowires or nanopillars to combine deep subwavelength focusing with resonance optical enhancement.[26] Semiconductor nanopillars and nanowires have recently drawn increased attention due to their unique optical properties.[27-30] Wider availability of technological approaches enabling their fabrication, synthesis, and integration into devices has contributed to this trend. Although semiconductor structures with sizes close to 100 nm are generally too large for quantum confinement effects to take place, such structures can function as dielectric waveguides that exhibit optical resonances in the visible spectrum.[26,28-30]

We have recently shown that resonances in silicon nanopillars can lead to enhanced fluorescence of the fluorophores on or near their surfaces.[26] Herein we further explore the ability of high aspect ratio silicon nanopillars to enhance fluorescence of the flourophore molecules in their vicinity and demonstrate that they are a valuable platform for fluorescence based bioaffinity assays.

6.3 Experimental section

6.3.1 Fabrication

Using electron beam lithography (EBL) and wafer level deposition and etching processes previously developed and optimized,[26,27] we have created individual silicon nanopillars and arrays with precisely controlled geometries (Figure 6.1). Following the EBL writing of the circular patterns in a positive tone electron beam resist (300 nm of Zep 520A), the main fabrication steps included vacuum deposition of a 20 nm chromium layer (VE-240, Thermonics Laboratory, Inc.) and metal lift-off to form a mask for subsequent selective anisotropic reactive ion etching (RIE) of the silicon substrate outside the nanopillar regions. Optimization of this fabrication sequence primarily involved tuning the RIE to achieve the desired etching profile and depth. In particular, power, pressure, temperature, time, and plasma composition (argon, sulfur hexafluoride, and octafluorocyclobutane) were adjusted to obtain targeted etch profiles (close to vertical) and depth (0.5−2 μm). Different nanopillar heights were achieved by varying the etching times. In order to elucidate the role silicon plays as a material of the nanopillars, some chips were additionally oxidized in oxygen under atmospheric pressure at 1000 °C for 30 min to 2 h in analogy to procedures described previously.[31]

The other variable design parameters included nanopillar diameter, number of individual nanopillars, and spacing between them in the arrays. In order to elucidate effects of these parameters on the fluorescence enhancement and other figures of merit of the performed bioassays, we designed a test pattern with a total area of 1 mm × 1 mm that contained individual nanopillars and pillar arrays with diameters of 80, 90, 100, 110, and 120 nm varying along the horizontal axis and number of nanopillars in the array (1 × 1 to 10 × 10)

and gap of 3 × 3 arrays varying along the vertical axis (Figure 2a). Each array was separated from those adjacent by distances greater than 20 μm to avoid any possibility of optical coupling or crosstalk. Each of the processed wafers contained a 400 × 400 array of the described test patterns and could be split into multiple chips. In order to test the effect of different pillar height and different RIE recipes, the wafers were split into chips before the RIE step.

6.3.2 Reagents

Phosphate buffered saline (pH 7.4), (3-aminopropyl) trimethoxysilane (APTMS), glutaraldehyde (GA), antihuman immunoglobulin G (Fc specific) capture antibody (antihIgG Fc), IgG from human serum (hIgG Ag), anti-human IgG (Fab specific)-FITC reporter antibody (anti-hIgG Fab, 3.0 mg/ mL), (+)-biotin N-hydroxysuccinimide ester (Biotin-NHS), and bovine serum albumin (BSA) were purchased from SigmaAldrich Chemical Co (St. Louis, MO) at the highest available purity. BSA-Alexa 596 (BSA-A596, 5.0 mg/mL) StreptavidinAlexafluor-568 (St-A568, 1.0 mg/mL), and StreptavidinDyLight 488 (St-D488, 1.0 mg/mL) were purchased from Invitrogen. All proteins used were divided into aliquots (1:50 protein−PBS).

6.3.3 Surface modification.

Figure 6.2d−f shows three different types of surface modifications and respective biochemical systems relevant to fluorescence bioassays carried out in the presented study. Before chemical modification, the surface of silicon chips with nanopillars was thoroughly cleaned using the following two-step procedure.

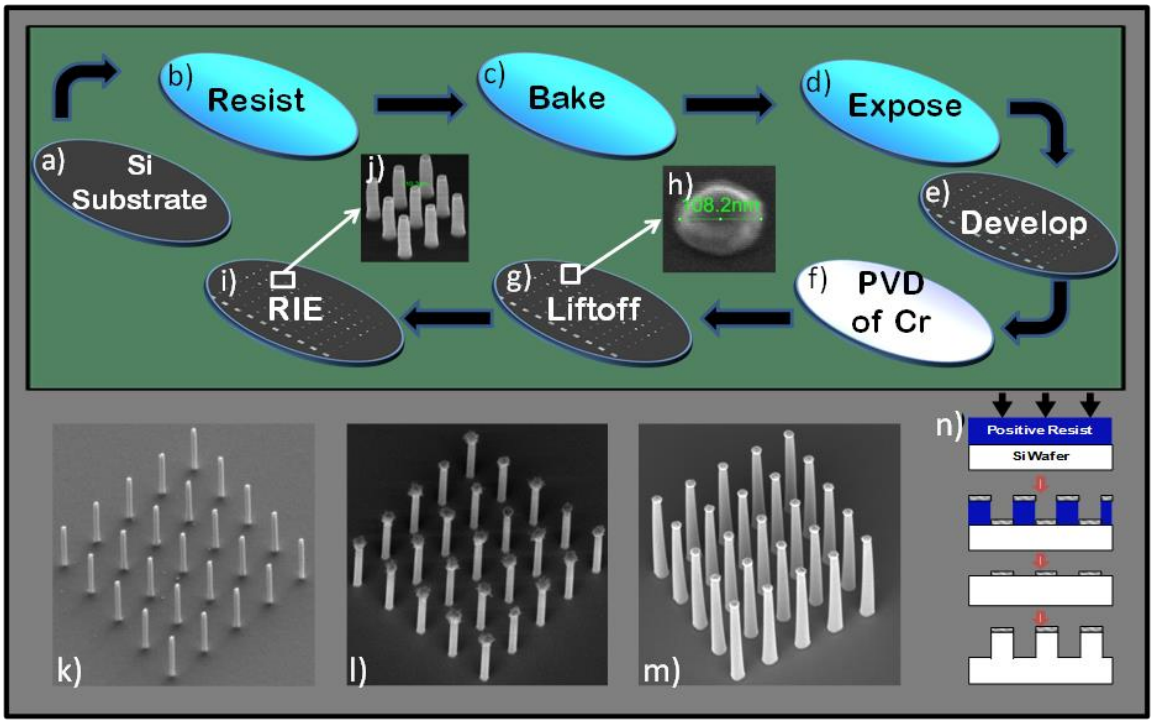

Figure 6.1. (a and b) Main processing steps of the fabrication sequence used in this work: (b) standard single side polished 4 in. silicon wafer used as a substrate. A 300 nm thick ZEP 520A positive tone resist applied using spin coating at 6000 rpm for 45 s, baked at 180 °C for 120 s, EBL exposure in the JEOL JBX-9300 FS/E EBL system, resist development in xylene, PVD of 20 nm chromium layer, chromium liftoff by sonication in an acetone bath, anisotropic RIE of silicon substrate in the areas without chromium mask. Selected SEM images of fabricated nanopillars: (c) 3 × 3 array of 110 nm diameter and 1 μm tall pillars, (d) SEM of a typical chromium dot pattern after liftoff, (e) 5 × 5 pillar array of 80 nm diameter and 1 μm tall pillars, (f) 5 × 5 array of 100 nm diameter 1 μm tall pillars, (g) 5 × 5 pillar array of 120 nm diameter and 2.6 μm tall pillars.

First, the chips were annealed in forming gas (10% H_2 in Ar) under atmospheric pressure at 800 °C for 15 min in a cold wall furnace (FirstNano) in order to volatilize fluoropolymer layer formed on the nanopillar sidewalls in octafluorocyclobutane plasma during the RIE and any other organic contamination. To restore the silanol-rich silicon surface the annealing step was followed by exposing the chips to oxygen plasma for 30 s (Ion Wave 10 Gas Plasma System, PVA TePla).

6.3.3.1 IgG-FITC

The chips with nanopillars were first treated with vapor phase APTMS under vacuum for 2 h. The APTMSmodified surface was then exposed to vapor phase glutaraldehyde (GA) for 2 h. The chips were then thoroughly rinsed in phosphate buffered saline (PBS) to remove any nonspecifically bound GA. Anti-hIgG was immobilized on the surface by dotting several droplets of the protein solution onto the surface for 1 h. Any potentially unbound GA was then blocked by immersing the nanopillars in a solution of bovine serum albumin (BSA, 0.5 mg mL^{-1} in PBS) and allowed to incubate overnight at 4 °C. Following incubation, the nanopillars were thoroughly rinsed with 0.05% Tween 20 in PBS. The hIgG Ag and anti-hIgG Fab were sequentially immobilized onto the nanopillars for 1 h in the same manner as anti-hIgG Fc, each step followed by thorough rinsing with PBS. After complete modification, the nanopillars were rinsed with deionized water before imaging to remove any remaining salt.

6.3.3.2 BSA-Alexa

Surface modification for the BSA-Alexa-596 binding platform was completed in a similar nature to the IgG-FITC assay up through modification with glutaraldehyde. Subsequently

30 μL of BSA-Alexa-596 (0.1 mg/mL in PBS) with three different ratios of fluorescently labeled−unlabeled proteins (all labeled, 1:100 and 1:1000) were dotted on the surface for 1 h, followed by thorough rinsing in a large volume of PBS.

6.3.3.3 BSA coverage and limits of detection

Assuming that a close packed BSA monolayer is characterized by average thickness of 5.7 nm and occupied area per molecule of 33 nm^2, we converted optical thicknesses of protein layers measured by ellipsometry into protein coverage. Knowing the surface area of the sample that corresponds to a pixel of interest, we then converted the BSA coverage derived from ellipsometry data into the total number of possibly observed BSA molecules. Although some of the amino groups on the labeled protein are occupied by the fluorophore, we assumed equal probability of binding of labeled and unlabeled BSA when calculating the number of labeled protein molecules on the nanopillar surface. When 1:100 and 1:1000 mixed solutions of labeled and unlabeled BSA were used, calculated numbers of protein molecules were divided by 100 and 1000, respectively.

6.3.3.4 Streptavidin

The chips were treated with vapor phase APTMS in the desiccator under vacuum for 2 h. Following the previously described procedures,[32] (+)-biotin N-hydroxysuccinimide ester (Biotin-NHS) was dissolved in dimethyl sulfoxide (DMSO) to a concentration of 15 mM and then diluted with PBS to a concentration of 1 mM. Approximately 30 μL of the solution was then dotted on the nanopillars for 1 h followed by thorough rinsing in a large volume of 0.05% Tween 20 in PBS.

6.3.4 Structural analysis

Scanning electron microscope (SEM) images were obtained with a Merlin (Carl Zeiss) microscope with a field emission gun operating at approximately 1.70 kV. The pillar heights were evaluated by optical profilometry (WYKO NT 9800 series optical profilometer) of a 10 μm × 10 μm test patterns adjacent to the nanopillars. Ellipsometry was carried at 70° incidence and 635 nm probing wavelength using a UVISEL spectroscopic ellipsometer (Horiba-Jobin Yvon) with the elliptical probing area of 1 mm × 1.5 mm. Ellipsometry data were fitted to a two layer optical model using DeltaPsi2 Software (Horiba Scientific). The model included a silicon substrate, a native oxide, and an organic layer. Optical properties of silicon and silicon dioxide were taken from the DeltaPsi2 material database. We assumed a constant refractive index n = 1.4 for the organic layer.

6.3.5 Optical microscopy and fluorescence data processing.

The fluorescence and dark field optical images were taken with a Nikon Eclipse LV150 microscope using the 100× objective. The microscope was equipped with a halogen lamp light source, a multicolor fluorescence cube (DAPI-FITC-TRITC), and a color CCD camera (DS-2M, Nikon, Inc.) controlled by NIS-Elements software. Fluorescence color (RGB) images with 16-bit color depth per channel were acquired by integrating a sequence of 16 8-bit color images. Fluorescence intensity was analyzed by evaluating line profiles drawn across centers of the pillars in the acquired images. The most intense peaks identified in the fluorescence intensity profiles acquired in each of the three trials were used to calculate the mean and standard deviation. Depending on the fluorophore used, the values from either the Green (G) or Red (R) channel were analyzed. These

values were collected from 5 × 5 pillar arrays across varying pillar diameters and extracted from the NISElements software (Nikon Instruments Inc.). All data have been background corrected by subtracting the intensity produced by a clean silicon surface. The same collection time and gain was used for both background and sample measurements. Subsequently data were normalized with respect to gain and collection time. The percent relative standard deviations (% RSD) values were determined by dividing the standard deviation by the mean peak intensity and multiplying by 100.

6.4 Results and discussion

6.4.1 Evaluation of pillar geometries

As illustrated in Figure 6.3, all pillars used in our analysis had cylindrical shapes with top to bottom diameter deviations within 5 nm from the reported target diameters. The increase in surface area from the pillar was calculated based on a flat 144,400 nm^2 area for all of the systems. The on pillar/off pillar ratio was used to normalize the intensity and determine enhancement above the nominal surface area increase. Within the experimental dimensions, it was determined only one pillar would contribute to an increase of surface area within the collection window. The on pillar/off pillar ratio of surface areas was calculated as follows. For a 90 nm diameter pillar with a 900 nm (~1 μm) height:

$$(144\ 400\ \text{nm} + (2\pi \times 45\ \text{nm} \times 900\ \text{nm}) - ((45\pi\ \text{nm}))^2/(144\ 400\ \text{nm})^2 = 2.7$$

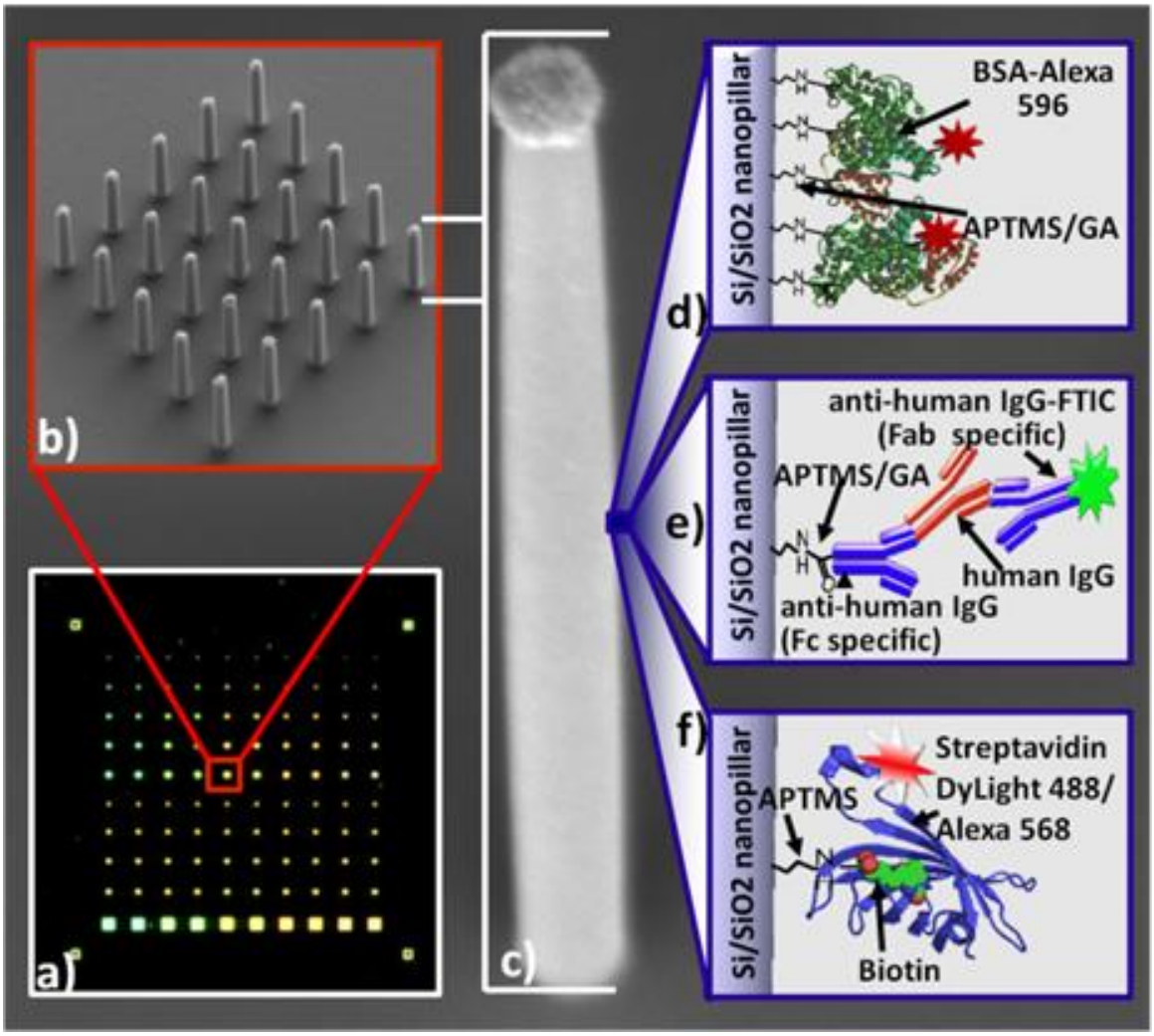

Figure 6.2. (a) Dark field optical microscopy image of the single test area populated with individual nanopillars and nanopillar arrays; (b) SEM image of a typical 5 × 5 array of nanopillars with 100 nm diameter and 1 μm height; (c) SEM image of an individual pillar with 120 nm diameter and 2 μm height viewed at an angle of 30°. Graphical illustrations of surface modifications and subsequent biomolecular interactions carried out on the nanopillar surfaces in the present study; (d) covalent attachment of fluorescently tagged BSA; (e) IgG immunofluorescent sandwich assay; (f) binding of fluorescently tagged streptavidin to surface immobilized biotin.

6.4.2 Control of protein aggregation

A critical aspect of developing a fluorescence bioassay that takes advantage of optical probing with highly localized, evanescent fields is a spatial control over the fluorescently labeled (reporter) molecules with the accuracy better than the decay length or span of enhanced optical fields. Indeed, enhanced fluorescence in the vicinity of plasmonic particles that exhibit LSPR can be very sensitive to changes in a spatial location of a fluorophore moiety as small as 1 nm.[33] Enhanced optical fields in the vicinity of nanopillars are characterized by much longer decay lengths, typically in the range of 10−100 nm.[26] Nonetheless, large protein aggregates or surface chemistries that rely on long molecular linkers can potentially separate reporter molecules too far from the nanopillar surface to achieve maximum possible fluorescence enhancement. Therefore, our attention was focused on surface modification procedures that provide controllable placement of reporter molecules as close as possible to the nanopillar surfaces. For this purpose we monitored an increase in the organic layer thickness after each treatment and reiterated chemical modifications and protein binding procedures until they yielded thicknesses consistent with expected nonaggregated layers. As a result of this refinement, vapor phase chemical modifications and additional more extensive rinsing steps described in Experimental Section were identified. Total increases in the organic layer thickness after treatment with APTMS and in the end of each assay that relied on these refined procedures are given in Table 6.1. In particular, the vapor phase treatment with ATPMS resulted in an average layer thickness of 2 nm with good uniformity (10% standard deviation). Taking into account that dimensions of the IgG molecule are 14.5 nm × 8.5 nm × 4 nm,[34] the average thickness of 8 nm measured after immobilization of the

AH-IgG (Fc specific) is consistent with close to a monolayer coverage of this protein. Likewise, the evaluated BSA-Alexa system had an averaged integrated thickness of 6 nm which correlates well with an estimated thickness of 5.7 nm for a BSA monolayer with random molecular packing. This estimate assumes that BSA molecules are 11.6 nm × 2.7 nm × 2.7 nm.[35] The average thicknesses of organic layers measured after binding of Alexa tagged and Dylight tagged streptavidin were 6 and 5 nm, respectively, with a standard deviation of 0.1 nm. These values are also consistent with a monolayer protein coverage since reported dimensions of the streptavidin protein are 4.5 nm × 4.5 nm × 5.8 nm.[36]

Among the evaluated samples, the thickest organic layers were present after completion of the sandwich immunoassay (Table 6.1). The final thickens of 12 nm is, therefore, the largest average distance that separated fluorophore molecules in our bioassays from the surface of native oxide on the silicon nanopillars. According to our calculations reported previously,[26] this distance corresponds to an approximately 30% decrease in the near field intensity compared to the maximum intensity directly on the surface of the silicon nanopillar.

6.4.3 Analysis of trends in enhanced fluorescence

In our quantitative analysis of the acquired fluorescence images, we sought to verify the two anticipated trends: (i) dependency of the fluorescence intensity on the pillar diameter and (ii) dependency of the optimum pillar diameter on the spectral position of the excitation and emission bands. Both trends can clearly be deciphered in the fluorescence images acquired after completing different bioassays (Figure 6.3).

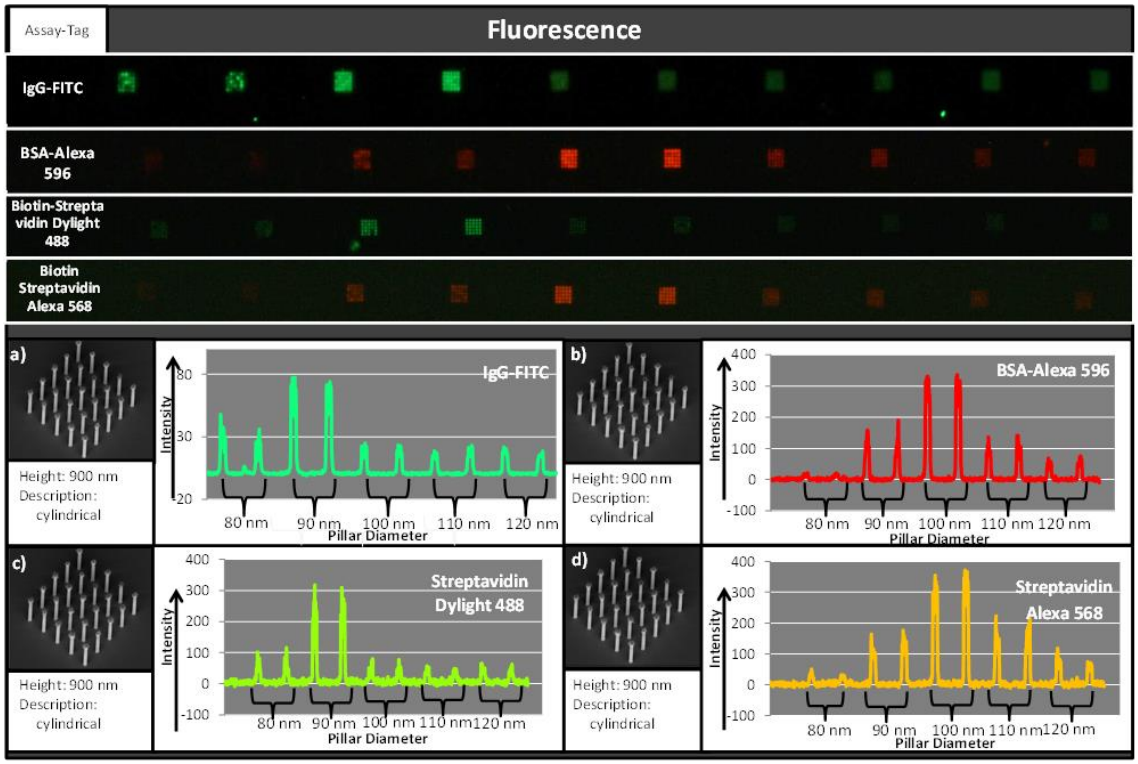

Figure 6.3. Representative fluorescent images of 5 × 5 arrays of 900 nm tall nanopillars with different diameters acquired at the final stage of four different assays. Fluorescence intensity profiles across pillars with different diameters for the following systems: (a) IgG-FTIC sandwich assay, (b) covalently attached BSA tagged with Alexa 596, (c) biotin-streptavidin tagged with Dylight 488, and (d) Biotin-Streptavidin tagged with Alexa 568 Fluorescent images of a system. (e) SEM image of a typical 5 × 5 array.

Table 6.1. Average Organic Layer Thicknesses and Their Standard Deviations Derived from Ellipsometric Measurements for Different Assays.

	APTMS	IgG-FITC full assay	AH-IgG (Fc specific) only	BSA-Alexa	Streptavidin-Alexa	Streptavidin-Dylight
average layer thickness (nm)	2	12	8	6	6	5
standard deviation (nm)	0.02	0.17	0.30	0.15	0.11	0.06

While exact predictions of the optimum pillar diameters for a particular combination of excitation and emission wavelengths can be very complex and are beyond our present study, the basic idea of dielectric cavity scalability dictates a constant ratio of the pillar diameter to the wavelength of the probing light. For the dyes with green and red emission we observe dramatic increases in fluorescence intensity in the vicinity of pillars with 90 and 100 nm diameters, respectively. The ratios of these diameters is 0.9, which matches very well the ratio of central wavelengths (483 nm/555 nm = 0.87) in the respective excitation bands of the triple band filter[37] used in our experiments. Strong nonmonotonic dependencies of the fluorescence intensity on the pillar diameter seen in Figure 6.3 a−d provide clear evidence that the optical field enhancement is of a resonance nature rather than a mere increase in the surface area due to the nanopillars and is largely responsible for the observed brighter fluorescence.

6.4.4 On pillar to off pillar intensity ratio.

In addition to the spectral and pillar diameter dependencies discussed above, we quantified the degree of achieved fluorescence enhancements as a function of pillar height and other parameters. It is important to note that, compared to smooth surfaces, high aspect ratio vertical nanostructures, such as silicon nanopillars used in present study, provide substantial additional surface area on the sample. It was shown previously that an increase in the surface area alone can lead to higher intensity of fluorescence and, in turn, improved performance of fluorescent bioassays.[31]

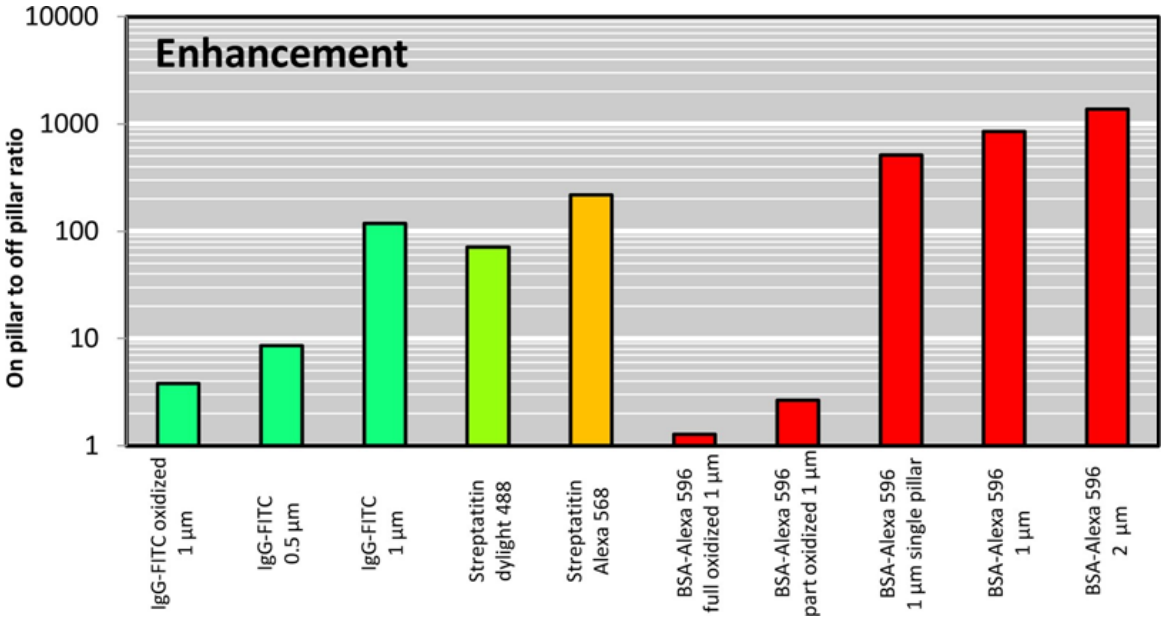

Figure 6.4. On pillar to off pillar ratio of fluorescence intensities across various systems used in the present study. Unless noted otherwise, all data shown here were collected from 5 × 5 arrays. Titles of the X-axis categories denote the type of bioassay, the pillar height, and optional silicon oxidation where appropriate.

In order to separate the effect of optical field enhancements due to resonances in silicon nanopillars[26,30,38] from a more generic effect due to increased quantity of the fluorophore, we calculated the on pillar to off pillar ratios for several systems and later normalized these ratios against the increase in surface area. Figure 6.4 shows results of this comparative analysis applied to a series of chips that had pillars of different heights and also included pillars that were partly or completely oxidized. In this analysis we aimed to evaluate factors other than the pillar diameter and, therefore, only the data collected from the pillars with the diameter that corresponded to the highest intensity are included in Figure 6.4. Note that analysis of intensities relative to the smooth substrates allowed us to compensate for differences between different assays due to differences in fluorophore brightness, labeling ratios, excitation efficiency, and spectral differences in the optical throughput. As can be seen in Figure 6.4, increased fluorescence intensities in the vicinity of nanopillars are characterized by several notable trends. First, silicon pillars with oxidized surfaces exhibited very weak enhancements while silicon pillars completely converted into silicon oxide exhibited almost no enhancement. Second, taller pillars resulted in consistently brighter fluorescence. In the case of the IgGFITC system, going from 0.5 to 1 μm tall pillars resulted in a nearly order of magnitude greater fluorescence enhancement which clearly cannot be attributed to the increased surface area alone. This trend, however, levels off in the case of taller pillars, and the difference between 1 and 2 μm tall pillars characterized in conjunction with the BSA-Alexa 596 systems is consistent with the increased surface area of the taller pillars.

Table 6.2. Summary of Intensity Enhancement Normalized by Surface Area Increase.

	enhancement		
	normalized by surface area		
IgG-FITC-oxidized	1	BSA-Alexa 596 full oxidized 1 um	0
IgG-FITC 0.5 urn	3	BSA-Alexa 596 part oxidized 1 um	1
IgG-FITC 1 um	43	BSA-Alexa 596 1 um single pillar	176
Streptatitin dylight 488	26	BSA-Alexa 596 1um	292
Streptatitin Alexa 568	75	BSA-Alexa 596 2 um	257

Finally, consistently stronger enhancements were observed with red dyes, which can be explained by the fact that silicon is a significantly more lossy (optically absorbing) material in the blue-green spectral region compared to the red. Below we provide additional details of our analysis of the enhanced fluorescence observed in various bioassays.

As shown in Table 6.2, the experimentally determined ratio of signal intensities for the IgG-FITC system was 118 giving a 43fold enhancement when the increase in the surface area due to a 90 nm diameter 1 μm tall pillar was taken into account. This is in stark contrast to the ratio for fully oxidized pillars with the same dimensions, which was only 1.4 when normalized by the surface area. The experimentally determined ratio of signal intensities for the streptavidin-Dylight 488 system was 71 giving a 26-fold enhancement after normalization by the surface area. The highest fluorescence enhancements were observed for the BSA-Alexa 596 system. The ratios for 1 and 2 μm tall arrays were 849 and 1366, respectively. These ratios corresponded to 292-and 257-fold enhancements after normalization by the surface area.

The ratio for Streptavidin Alexa 568 was 217 giving a 75-fold enhancement over a nominal surface area increase. The ratio for BSA-Alexa 596 1 μm single pillar was 512 giving a 176-fold enhancement when normalized by surface area. The ratio for BSA- Alexa 596 partially oxidized 1 μm array was 2.6 having no enhancement over the surface area increase. The ratio for the BSA-Alexa 596 fully oxidized 1 μm array was 1.3 have a quenching effect on the signal ratios of just over half.

Despite the fact that lateral sizes of individual pillars are well below the diffraction limit, they are resolved in the acquired fluorescence images (Figure 6.5). Individual pillars in

the 5 × 5 arrays are also well resolved (Figure 6.5b), which is consistent with the center to center distances comparable to the diffraction limit of the 100× objective used in our experiments. However, diffraction contributes to the apparent cross talk between adjacent pixels. Note that pixels in the acquired images correspond to sample area of 50 nm × 50 nm, which is smaller than the diffraction limit of 380 nm. This can explain somewhat lower enhancement values obtained for the individual BSA-Alexa 596 pillars in comparison to the 5 × 5 BSA-Alexa 596 arrays (Figure 6.4).

6.4.5 Approaching single molecule detection

The ability to collect strong fluorescence signals generated by biomolecules immobilized on the surface of a single nanopillar prompted us to assess applicability of this platform to single molecule experiments. For this purpose we carried assays in which labeled BSA was diluted with unlabeled BSA in ratios of 1:100 and 1:1000 and evaluated resulting fluorescence intensity generated in the areas with 5 × 5 arrays of 90 nm diameter 1 μm tall pillars (Figure 6.6).

On the basis of the estimated protein coverage and calculated surface area of the single pillar, we estimated that there are 8000 protein molecules immobilized on one pillar. In total, 1:100 and 1:1000 dilutions correspond to, respectively, 80 and 8 labeled protein molecules on the pillar surface. The samples with the largest numbers of labeled proteins gave an excellent signal-to-noise ratio (SNR = 90:1) and RSD of 1%. The sample that had 1 labeled protein per 100 BSA molecules gave, respectively, lower signal intensity with RSD of 8% and SNR of 13:1.

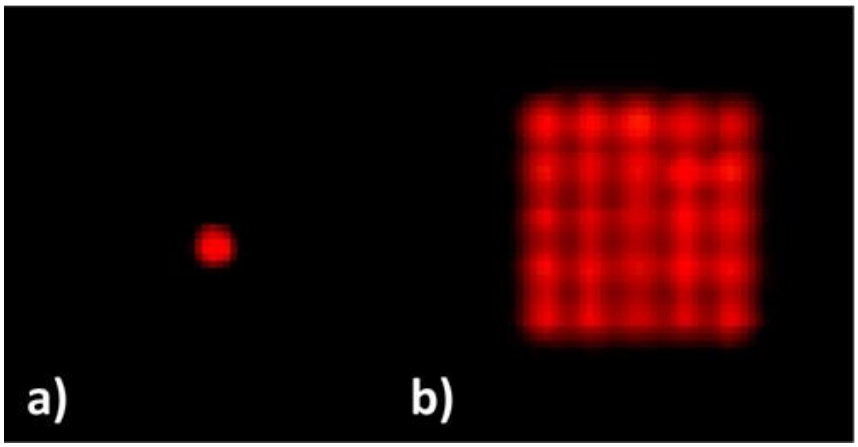

Figure 6.5. . (a) Example of a fluorescence image of a single 100 nm diameter 1 µm tall pillar with BSA-Alexa 596 and (b) fluorescence image showing similar pillars that are clearly resolved in a 5 × 5 array with a center to center distance of 640 nm.

Even the sample with the smallest number of labeled protein molecules gave values of RSD and SNR acceptable for many practical applications (RSD = 18% and SNR = 5.5). These results clearly show the potential of the developed approaches for detection of trace levels of analytes down to single molecules.

6.4.6 Blank immunoassay experiments.

Another important practical figure of merit of any immunoassay is specificity of the measured responses. In order to evaluate this figure of merit, we performed blank experiments, in which the sandwich assay with IgG-FITC reporter molecules was completed without exposing chips with pillars to the human IgG. Figure 7 shows a comparison of signal intensities observed in blank samples versus the full assay with the human IgG. Although the blank sample gives a significantly lower (6 times) signal intensity, the nonzero emission detected from the sample without the human IgG indicates a finite specificity of the implemented immunoassay. Further optimization of the incubation and rinsing protocols will likely reduce nonspecific binding of the reporter molecules in this system. The system without the IgG had an RSD of 15% over the sample set. The system with the IgG had an RSD of 6% over the sample set.

6.3 Conclusions

In the present study, we successfully demonstrated fluorescence bioassays using a newly developed on-chip platform based on silicon nanopillars which provide nanoscale focusing and resonance enhancement of the probing optical fields. Results obtained using various biological fluorescent systems indicate that enhancement of fluorescence signals associated with silicon nanopillars significantly exceed a surface area increase.

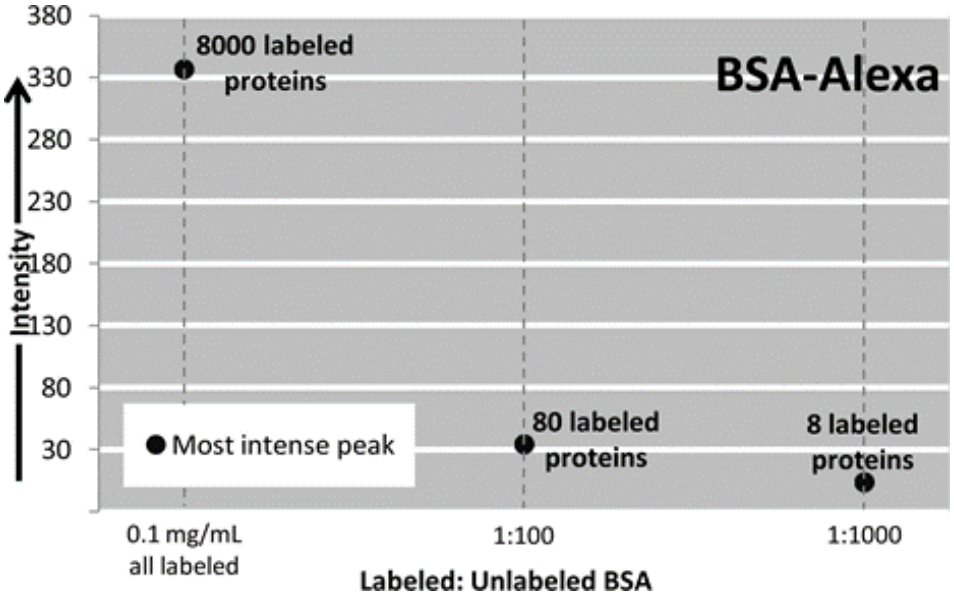

Figure 6.6. Fluorescence intensity in the BSA-Alexa 596 assay as a function of label dilution with an estimated number of molecules contributing to the signal.

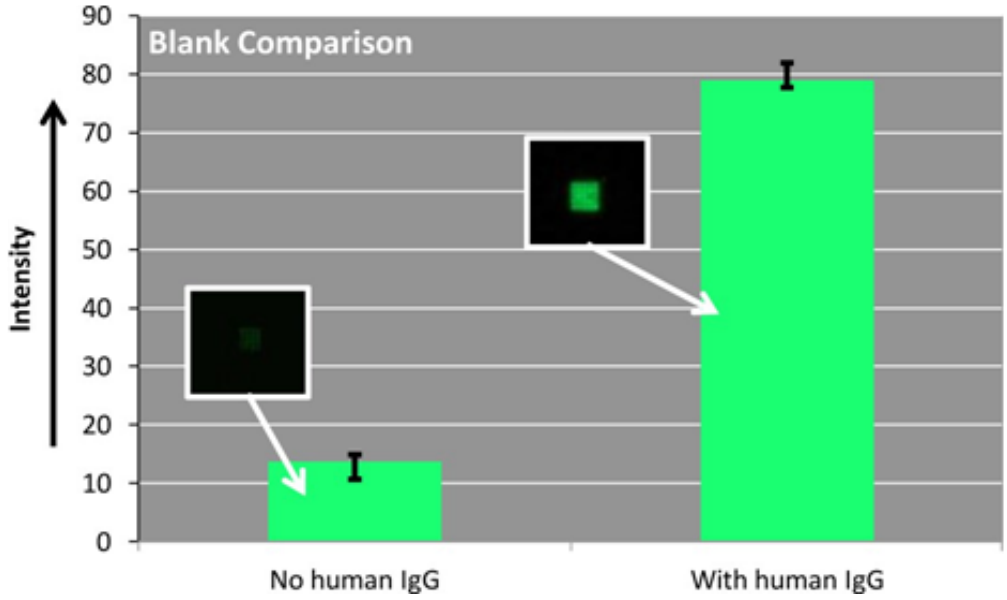

Figure 6.7. Intensity comparison of the mean of the most intense peak from the fluorescent profile of assay with and without the IgG visual example of emission.

We believe the demonstrated platform will be a valuable addition to the series of the previously developed systems for fluorescence analysis, such as LSPR based systems and ZMW. Compared to other concepts and designs that already found applications in fluorescence analysis, the most distinctive features of the system based on silicon nanopillars include their straightforward spectral tunability and pronounced out-of plane geometry. The latter can be particularly useful in designing methods that combine multiple, for instance, optical and electrochemical,[39] modes of analytical interrogation of biological samples and cells. Results of our feasibility experiments reported here complement these unique aspects of the demonstrated approaches with a series of quantitative figures of merit that include detectability of fewer than 10 protein molecules, lateral resolution down to the diffraction limit, and enhancement of fluorescence in excess of 10^3.

6.4 Author information

Corresponding Authors

*Phone: 865-974-8023. E-mail: msepaniak@utk.edu.

*Phone: 865-241-2636. E-mail: lavriknv@ornl.gov.

Department of Chemistry, University of Tennessee Knoxville, Knoxville, Tennessee 37996.

6.5 Acknowledgements

This research was conducted at the Center for Nanophase Materials Sciences, which is sponsored at Oak Ridge National Laboratory by the Scientific User Facilities Division,

Office of Basic Energy Sciences, U.S. Department of Energy. This material is based on work supported in part by the National Science Foundation under Grant CHE-1144947 with the University of Tennessee.

6.7 References

[1] Koivunen, M. E.; Krogsrud, R. L. LabMedicine 2006, 37, 490− 497.

[2] Kiptoo, M. K.; Mpoke, S. S.; Ng'Ang'A, Z. W. East African Med. J. 2004, 81, 222−225.

[3] Trouillon, R.; Passarelli, M. K.; Wang, J.; Kurczy, M. E.; Ewing, A. G. Anal. Chem. 2013, 85, 522−542.

[4] Walt, D. R. Anal. Chem. 2013, 85, 1258−1263.

[5] Duan, Y.; Miao, L.; Ye, H.; Yang, C.; Fu, B.; Schwartz, P.; Rayner, S.; Fortunato, E.; Luo, M.-H. Acta Biochim. Biophys. Sin. 2012, 44, 597−605.

[6] Kang, E.-S.; Min, J.-H.; Lee, K. H.; Kim, B. J. Ann. Lab. Med. 2012, 32, 331−338.

[7] Chin, C. D.; Laksanasopin, T.; Cheung, Y. K.; Steinmiller, D.; Linder, V.; Parsa, H.; Wang, J.; Moore, H.; Rouse, R.; Umviligihozo, G.; Karita, E.; Mwambarangwe, L.; Braunstein, S. L.; van de Wijgert, J.; Sahabo, R.; Justman, J. E.; El-Sadr, W.; Sia, S. K. Nat. Med. 2011, 17, 1015−1019.

[8] Zhang, F.; Turgeon, N.; Toulouse, M.; Duchaine, C.; Li, D. Diagn. Microbiol. Infect. Dis. 2012, 74, 263−266.

[9] Ozawa, T.; Yoshimura, H.; Kim, S. B. Anal. Chem. 2013, 85, 590− 609.

[10] Diercks, A. H.; Ozinsky, A.; Hansen, C. L.; Spotts, J. M.; David,

[11] J. R.; Aderem, A. Anal. Biochem. 2008, 2009, 30−35.

[12] Kai, J.; Puntambeker, A.; Santiago, N.; Lee, S. H.; Sehy, D. W.; Moore, V.; Han, J.; Ahn, C. H. Lab Chip 2012, 12, 4257−4262.

[13] Green, J. V.; Sun, D. W.; Hafezi-Moghadam, A.; Lashkari, K.; Murthy, S. K. Biomed. Microdevices 2011, 13, 573−583.

[14] Simpson, M. L.; Sayler, G. S.; Patterson, G.; Nivens, D. E.; Bolton, E. K.; Rochelle, J. M.; Arnott, J. C.; Applegate, B. M.; Ripp, S.; Guillorn, M. A. Sens. Actuators, B: Chem. 2001, 72, 134−140.

[15] Yang, H.; Gijs, M. A. M. Anal. Chem. 2013, 85, 2064−2071.

[16] Craighead, H. Nature 2006, 442, 387−393.

[17] Cretich, M.; di Carlo, G.; Longhi, R.; Gotti, C.; Spinella, N.; Coffa, S.; Galati, C.; Renna, L.; Chiari, M. Anal. Chem. 2009, 81, 5197−5203.

[18] Cretich, M.; Monroe, M. R.; Reddington, A.; Zhang, X. R.; Daaboul, G. G.; Damin, F.; Sola, L.; Unlu, M. S.; Chiari, M. Proteomics 2012, 12, 2963−2977.

[19] Choumane, H.; Ha, N.; Nelep, C.; Chardon, A.; Reymond, G. O.; Goutel, C.; Cerovic, G.; Vallet, F.; Weisbuch, C.; Benisty, H. Appl. Phys. Lett. 2005, 87, 031102.

[20] Hung, Y. J.; Smolyaninov, C. C., II; Davis; Wu, H. C. Opt. Express 2006, 14, 10825−10830.

[21] Xie, C.; Hanson, L.; Cui, Y.; Cui, B. X. Proc. Natl. Acad. Sci. U.S.A. 2011, 108, 3894−3899.

[22] Hao, Q.; Qiu, T.; Chu, P. K. Prog. Surf. Sci. 2012, 87, 23−45.

[23] Kinkhabwala, A.; Yu, Z. F.; Fan, S. H.; Avlasevich, Y.; Mullen,

[24] K.; Moerner, W. E. Nat. Photon. 2009, 3, 654−657.

[25] Lakowicz, J. R.; Shen, Y. B.; D'Auria, S.; Malicka, J.; Fang, J. Y.; Gryczynski, Z.; Gryczynski, I. Anal. Biochem. 2002, 301, 261−277.

[26] Foquet, M.; Samiee, K. T.; Kong, X.; Chauduri, B. P.; Lundquist, P. M.; Turner, S. W.; Freudenthal, J.; Roitman, D. B. J. Appl. Phys. 2008, 103, 034301.

[27] Zhu, P.; Craighead, H. G. Annu. Rev. Biophys. 2012, 41, 269− 293.

[28] Wells, S. M.; Merkulov, I. A.; Kravchenko, N. V., II; Lavrik; Sepaniak, M. J. ACS Nano 2012, 6, 2948−2959.

[29] Walker, B. N.; Stolee, J. A.; Pickel, D. L.; Retterer, S. T.; Vertes,

[30] J. Phys. Chem. C 2010, 114, 4835−4840.

[31] Cao, L. Y.; White, J. S.; Park, J. S.; Schuller, J. A.; Clemens, B.

[32] M.; Brongersma, M. L. Nat. Mater. 2009, 8, 643−647.

[33] Cao, L. Y.; Fan, P. Y.; Barnard, E. S.; Brown, A. M.; Brongersma,

[34] M. L. Nano Lett. 2010, 10, 2649−2654.

[35] Seo, K.; Wober, M.; Steinvurzel, P.; Schonbrun, E.; Dan, Y.; Ellenbogen, T.; Crozier, K. B. Nano Lett. 2011, 11, 1851−1856.

[36] Suzuki, Y.; Yokoyama, K. Biosens. Bioelectron. 2011, 26, 3696− 3699.

[37] Briand, E.; Humblot, V.; Landoulsi, J.; Petronis, S.; Pradier, C.-

[38] M.; Kasemo, B.; Svedhem, S. Langmuir 2010, 27, 678−685.

[39] Anger, P.; Bharadwaj, P.; Novotny, L. Phys. Rev. Lett. 2006, 96, 113002.

[40] Lynch, M.; Mosher, C.; Huff, J.; Nettikadan, S.; Johnson, J.; Henderson, E. Proteomics 2004, 4, 1695−1702.

[41] Bowen, W. R.; Gan, Q. Biotechnol. Bioeng. 1991, 38, 688−696. (36) Caswell, K. K.; Wilson, J. N.; Bunz, U. H. F.; Murphy, C. J. J. Am. Chem. Soc. 2003, 125, 13914−13915.

[42] Scordata, A.; and Schwartz, S. In Fluorescence Filter Combinations; Nikon Instruments, Inc., New York, 2010; Vol. 2011.

[43] Park, H.; Seo, K.; Crozier, K. B. Appl. Phys. Lett. 2012, 101, 193107.

[44] McKnight, T. E.; Melechko, A. V.; Fletcher, B. L.; Jones, S. W.; Hensley, D. K.; Peckys, D. B.; Griffin, G. D.; Simpson, M. L.; Ericson, M. N. J. Phys. Chem. B 2006, 110, 15317−15327.

CHAPTER 7:
NANOPILLAR-BASED ENHANCED-FLUORESCENCE DETECTION OF SURFACE-IMMOBILIZED BERYLLIUM.

A version of this chapter was originally published by Jennifer J. Charlton, Natalie C. Jones, Ryan A. Wallace, Robert W. Smithwick, James A. Bradshaw, Ivan I. Kravchenko, Nickolay V. Lavrik, and Michael J. Sepaniak.

Charlton, J.J., et al., *Nanopillar-based enhanced-fluorescence detection of surface-immobilized beryllium.* Analytical Chemistry, 2015.

All changes from the original manuscript are trivial in nature and result from reformatting to conform to standards for a dissertation as required by The University of Tennessee in Knoxville. Ivan I. Kravchenko contributed with electron beam lithography. Ryan Wallace contributed with the setup and operation of the multiplexing apparatus. The remaining coauthors contributed intellectual capital.

7.1 Abstract

The unique properties associated with beryllium metal ensures the continued use in many industries despite the documented health and environmental risks. While engineered safeguards and personal protective equipment can reduce risks associated with working with the metal it has been mandated by the EPA and OSHA that the workplace air and surfaces must be monitored for toxic levels. While many methods have been developed to monitor levels down to the low μg/m^3 the complexity and expense of these methods have driven the investigation into alternate methodologies. Herein, we use a combination of the previously developed fluorescence Be (II) ion detection reagent, 10-hydroxybenzo[h]quinoline (HBQ), with an optical field enhanced silicon nanopillar array, creating a new surface immobilized (si-HBQ) platform. The si-HBQ platform allows the positive control of the reagent for demonstrated reusability and a pillar diameter based

tunable enhancement. Furthermore, native silicon nanopillars are over-coated with thin layers of porous silicon oxide to develop an analytical platform capable a 0.0006 µg/L LOD using sub µL sample volumes. Additionally, we demonstrate a method to multiplex the introduction of the sample to the platform, with minimal 5.2% RSD at 0.1 µg/L, to accommodate the potentially large number of samples needed to maintain industrial compliance. The minimal sample and reagent volumes, lack of complex and highly specific instrumentation, as well as positive control, and reusability of traditionally consumable reagents creates a platform that is accessible and economically advantageous.

7.2 Introduction

Beryllium metal has a unique combination of strength, lightweight, low neutron absorption, transparency to X-rays, and dimensional stability over a wide temperature range. Approximately 84 metric tons of beryllium products were consumed in the United States market in 2005, with electrical components, aerospace and defense applications accounting for an estimated 80% of that total.[1-4] In contrast to the benefits of beryllium and its compounds, there are health hazards and risks associated with its use. According to the Environmental Protection Agency the main pathway beryllium enters the human body is inhalation. This exposure can lead to beryllium sensitization causing granulomas, inflammation and scarring of lung tissues associated with chronic beryllium disease.[5-7] Additionally, beryllium is listed as a human carcinogen on the National Toxicology Program's Report on Carcinogens based on evidence of an increased risk of developing lung cancer after beryllium exposure. It is estimated that the number of workers in the

United States currently exposed to beryllium as being between 54,000 and 134,000, with perhaps 3 to 5 times as many having been exposed at some time in the past.[1-3] Although there are well documented health risks associated with beryllium and beryllium compounds they continue to be used. While safeguards such as adequate ventilation and personal protective equipment can reduce risk associated with beryllium[2] it is important to monitor the levels of beryllium in the air and on surfaces in the workplace.

Many methods have been developed and tested to detect trace-level beryllium concentrations in occupational hygiene samples including graphite-furnace atomic-absorption spectroscopy, inductively coupled plasma-atomic emission spectroscopy, and inductively coupled plasma- mass spectrometry are some of the most widely used.[8-10] The complexity and expense of these methods have driven the investigation into alternate methodologies. The Occupational Safety and Health Administration has set air contaminant exposure general industry at a limit of 2 $\mu g/m^3$ for an 8-hour time weighted average.[11] The EPA beryllium inhalation reference concentration is 0.02 $\mu g/m^3$ for a 24-hour period.[3]

Recently, it has been found that 10-hydroxybenzo[h]quinoline (HBQ) and other derivatives, such as hydroxybenzo[h]quinoline sulfonate (HBQS)[9] and 2-(2'-hydroxyphenyl)-10-hydroxybenzo[h]quinoline (HPHBQ),[8] can be used as a fluorescence reagent for detection of the Be(II) ion. In the cases of HBQS and HPHBQ, modifications have been made to HBQ in order to increase solubility for analysis of beryllium in aqueous solutions[9] and for use in pre-column chelation.[8] At high pH both HBQ and HBQS chelate specifically with the beryllium ion in a 1:1 ratio to form a six-

membered ring. [8-10] The formation of this complex results in a shift in emission spectral characteristics from 575-590 nm to 475-496 nm.[8-10] Additionally, when HBQ complexes with the Be (II) ion, the intensity of the fluorescent signal increases by over 10 fold. The fluorescence intensity has also been shown to be linear in comparison with beryllium concentrations down to the low $\mu g/m^3$.[10] Currently HBQ and its derivatives are being used in solution. For the first time, we investigate a field enhanced, surface immobilized, spectral shifting coordination compound that can be used for fluorescence based elemental detection. Furthermore, we develop and optimized this platform and the associated novel methods of analysis delivering a fully developed pathway capable of quantification down to the ultra-trace levels for environmentally important Be analysis.

The use of a silicon nanopillar substrate[12, 13] was selected to enhance the fluorescence signal from complexed HBQ-Be while minimizing reagent consumption. Immobilizing HBQ allows for positive control of a traditionally consumable reagent. The use of nanoscale platforms further minimizes reagent consumption and sample volumes to the microliter aliquots. The vertical geometry of the pillar profusions from the flat silicon-wafer substrate as well as further roughened and porous surfaces increases the area and number of sites available to bind the Be (II) ion within the field of view of the analyzing optics. Most importantly, silicon pillars at and near 100 nm diameters have been shown to selectively enhance fluorescence through the manipulation of the electromagnetic (EM) near fields in the spectral region of interest. Acting similarly to a dielectric cavity or a waveguide, the optimum pillar diameters scale in proportion to desired wavelength.[12, 13] From a practical point of view, the idea of controlling the near field EM environment

of HBQ based fluorescence beryllium detection is appealing, as it allows the maximum amount of light to be collected from each fluorophore molecule. It also takes advantage of the hypochromic spectral shift associated with the complexed form of HBQ by tailoring a system that selectively enhances shorter wavelength emissions over those with less energy.

Using electron beam lithography (EBL) cleanroom fabrication techniques described previously,[12, 13] nano-scale pillar arrays can be patterned to optimize pillar dimensions for a surface immobilized HBQ (si-HBQ) platform for beryllium analysis. While this fabrication pathway permits exquisite control of pillar placement and dimensions, the cost and time demands associated with EBL precludes it as an option for the cost-effective production of a platform with intended use for high-throughput analysis of beryllium. The optimal pillar dimensions found by EBL were used to fabricate an alternate less-ordered nano-array system fabricated by using Pt dewetting (DW) described previously.[14, 15] The tradeoff is the precise dimensional control of individual pillars via EBL, versus control of an averaged pillar diameters using DW. The latter approach results in pillar arrays with size relative standard deviation around 14%.[14] However, the DW process allows for the rapid production of expansive stochastic pillar arrays drastically increasing production capacity. The fabricated pillars were evaluated with and without an overcoat of a layer of porous silicon oxide (PSO) deposited with room-temperature plasma enhance chemical vapor deposition (PECVD). Pillars with this PSO coating that has been previously shown[14] to further increase fluorescent brightness as well as add increased

hydrophobic functionality allowing for low area spotting and concentration[16] of aqueous samples.

7.3 Experimental

7.3.1 Fabrication

To evaluate pillar based intensities we created silicon nanopillar arrays with precisely controlled geometries using EBL and wafer level deposition and etching processes that were previously reported.[12, 13, 17] This process involved writing of the circular patterns in a positive tone electron beam resist (300 nm of Zep 520A), followed by vacuum deposition of a 20 nm chromium layer (VE-240, Thermonics Laboratory, Inc.) and metal lift-off in acetone to form a mask, and finally anisotropic reactive ion etching (RIE) of the silicon substrate not masked by chromium. These pillar arrays were 10 X 10 pillars with diameters of 80, 90, 100, 110, and 120 nm varying along a horizontal axis, and etched to create pillars the height of 1 ± 0.2 μm. Each array was separated from those adjacent by distances greater than 20 μm to avoid any possibility of optical coupling or crosstalk. While this method gives precise control over the spatial characteristics of the pillars arrays, cost and time constraints are limiting when creating a high throughput analysis platform. The expansive arrays of stochastic pillar arrays that were used as a platform for a high throughput analysis of the Be (II) ion were fabricated by the thermal DW of a Pt film process previously developed.[14,15] This method begins started with physical vapor deposition of a thin Pt film (Thermonics Laboratory, VE-240) on a p-type silicon wafer with 100 nm of thermally grown SiO_2. During the Pt deposition, the deposition rate and the average (mass-based) thickness of the deposited metal were monitored with a quartz-

crystal microbalance. The platinum film was then thermally annealed in a 10:1 mixture of argon and hydrogen at 735 Torr in a cold wall furnace (Easy Tube 3000, First Nano, Ronkonkoma, NY) equipped by a radiative heat source. During the anneal step the heat source was set to its maximum power (22 kW) for 8 s yielding an estimated maximum substrate temperature of 900 °C. The thermally induced metal-film dewetting created circular masking patterns. These platinum islands were subsequently used as a selective mask for RIE (Oxford PlasmaLab, Oxford Instruments, UK). In each process the RIE was tuned via power, pressure, temperature, time, and plasma composition (argon, sulfur hexafluoride, and octafluorocyclobutane) to achieve the desired etching profile of close to vertical and depth of approximately 1 μm. The structure of pillars were confirmed with scanning electron microscope (SEM) images obtained with a Merlin (Carl Zeiss) microscope with a field-emission gun operating at approximately 3 kV. The pillar heights were also evaluated by optical profilometry (WYKO NT 9800 series optical profilometer) of a 10 μm × 10 μm test patterns adjacent to the nanopillars. Both platforms were annealed in 10% H_2 in Ar under atmospheric pressure at 800°C for 15 min in a cold wall furnace (FirstNano) to remove any residual organics from the pillar arrays. To restore the silanol-rich silicon surface the annealing step was followed by exposing the chips to oxygen plasma for 30 s (Ion Wave 10 Gas Plasma System, PVA TePla).

The PSO coating was accomplished via a room temperature PECVD (PECVD, Oxford Instruments) [14,18,19] with chamber temperature at 27 °C and pressure at 600 mTorr. The capacitively coupled RF plasma source was set to a power of 150 W with gas flow rates of 75.0 sccm 5% SiH_4 in Ar and 600 sccm N_2O. Pillar arrays with the thicknesses of

5nm, 10 nm, and 25 nm PSO coating were prepared and subsequently evaluated against the pillar arrays and flat substrate without PSO.

7.3.2 Chemical surface modifications

To experimentally evaluate surface area increase associated with PSO, slat substrates deposited with 0, 5, 10, and 25 nm PSO were fluorescently labeled with fluorescein isothiocyanate (FTIC) for imaging.[20] Using a method described previously,[21] substrates were placed in a sealed vial with a solution of 10 % by volume 3-aminopropyltriethoxysilane (APTES) in anhydrous toluene. The pillar arrays were soaked in the APTES solution at room temperature for 1 h then rinsed sequentially with toluene, methanol, and 18 MΩ deionized water (Barnstead, E-Pure). Substrates were soaked in a 1 mM solution of FITC dye in ethanol for 45 min then triple rinsed in ethanol to remove excess dye.

The pillar arrays functionalized for Be detection (Figure 1a) were placed in a sealed vial with 0.1 M chloropropyltrimethoxysilane (CTMS) (Aldrich Chemistry) in hexane for 6 h followed by washing with ethanol, hexane, and acetone as describe previously.[20] This method has been shown to produce a thin homogenous CTMS layer (Figure 7.1b). After rinsing the arrays were placed in 0.5 M NaOH at 70 °C for 15 min, then placed in 3 M HCl at 70 °C for 15 minutes (Figure 1c). The chips were directly placed in a sealed vial of a 1 M solution of 10-hydroxybenzo[h]quinolone (HBQ) (Tokyo Chemical Industry, Co. LTD) in methylene chloride (Figure 1d).

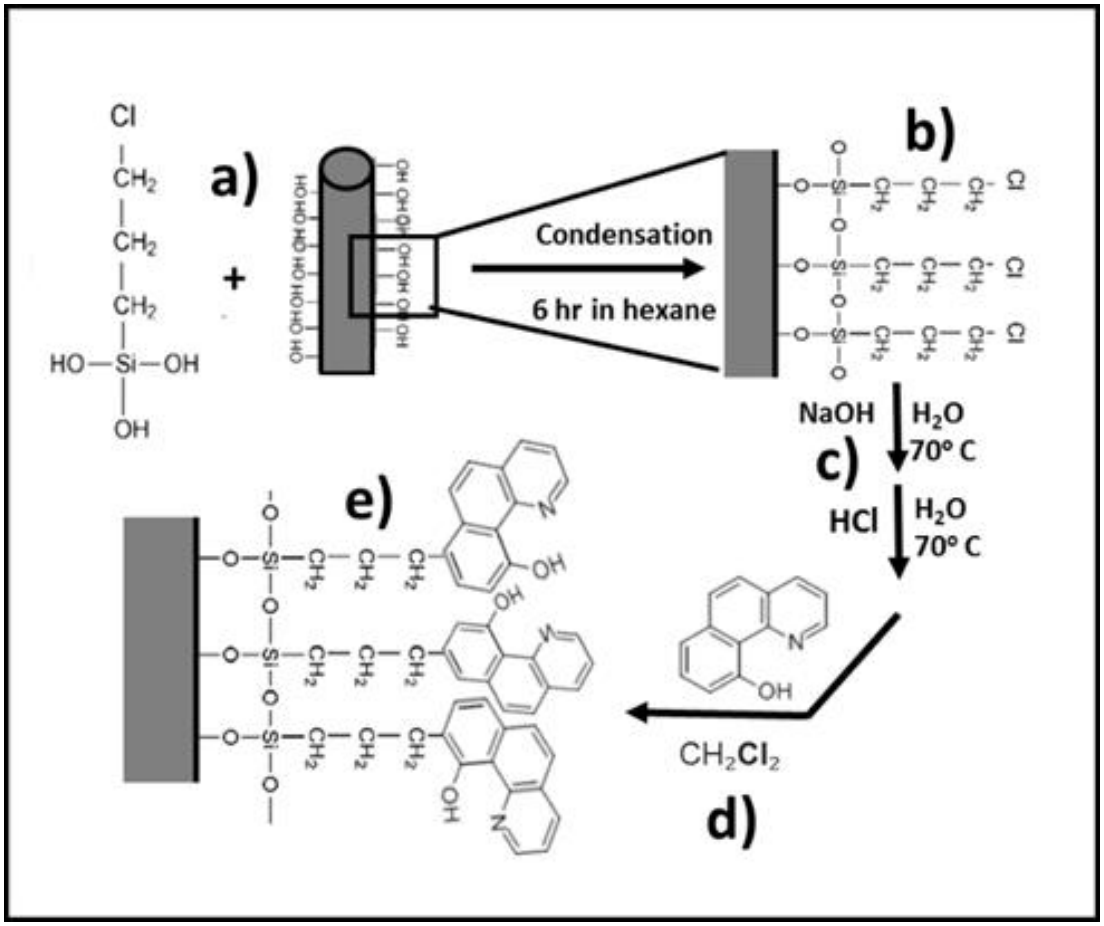

Figure 7.1. . The functionalization of pillar arrays for Be (II) ion detection begins with a) hydrolyzed CTMS and a silanol rich pillar substrate. When condensed for 6 hours in hexane creates a b) thin layer of CTMS of the pillar surface. Through c) a base-catalyzed substitution followed by an acid-catalyzed reduction the chloro-terminated alkyl chain is transformed to alkene terminated. When reacted with d) HBQ in methylene chloride for 12 hours, produces a e) surface immobilized HBQ.

After 12 hours, the chips were rinsed with ethanol and visually inspected with a 360 nm UV light for the faint red fluorescence signature associated with HBQ,[8-10, 22] without the presence of Be, indicating the surface immobilization of HBQ on the pillar substrate (Figure 7.1e), that we will refer to as the si-HBQ.

7.3.3 Reagents and solutions

***Caution** Beryllium Chloride is on the Hazardous Substance List because it is regulated by OSHA and cited by ACGIH, DOT, NIOSH, NTP, DEP, IARC, IRIS and EPA. This chemical is on the Special Health Hazard Substance as a CARCINOGEN.*

The standard (1 μg cm^{-3}) Be (II) ion solution was prepared from anhydrous beryllium chloride (Sigma-Aldrich) in 0.01 M HCl solution, as described previously.[9] Aliquots of this standard solution were used to make the sample solution in a 25 cm^3 volumetric flask, with 5 cm^3 0.01 M disodium EDTA solution, 3 cm^3 0.5 M NaOH, then diluted to volume with 18 MΩ distilled water. All EBL created si-HBQ studies used spotted with sample solutions with 10 ng cm^{-3} Be (II) concentration. Then rinsed with 0.5 M NaOH to remove any unbound analytes or contaminants. The stochastic si-HBQ platform calibration study was spotted with 0.1 μL of the sample solutions with concentrations of 0.001, 0.01, 0.1, and 1 μg/L.

7.3.4 Spotting

Initially the Be (II) ion was manually delivered using a National Scientific 10 μL pipet (Thermo Scientific, Suwanee, GA). A 0.10 μL of Be (II) ion samples were spotted on the si-HBQ substrate and allowed to evaporate at room temperature. Although the manual placement of the droplets worked adequately throughout the study, it is a very time and

labor intensive procedure. As shown previously,[16] the spotting of an aqueous solution on a hydrophobic surface may be multiplexed via electo-osmotic flow. The experimental setup was made of a 30 cm long standard coated fused silica capillary tube (TSP, o.d. = 365 μm, i.d. = 78 μm, Polymicro Technologies, Phoenix, AZ), fixed at both ends with a 22 G × 1 1/2 in. BD Precision Glide Needle (Becton, Dickinson and Company, Franklin Lakes, NJ). The capillary tube was syringe filled with Be (II) solution and placed in a reservoir of the same solution. The delivery needle of the capillary was affixed via aluminum plates and adjusted to prevent gravity flow. The positive electrode was placed into the reservoir, and the negative electrode was connected to the aluminum plates. A voltage of 2.5 kV was then applied across the electrodes to allow for flow from the positive to the negative. The droplets were allowed to grow and then contact spotted onto the si-HBQ substrate.

The Be (II) ion sample solution is a basic aqueous solution. Additional spotting was done to determine the hydrophobic/hydrophilic nature of the functionalized substrate. These where 1 μL spots of Be (II) ion sample solution and imaged at 90° from substrate surface with a 5.0 MP autofocus camera with LED Flash (LG Optimus F3). The contact angle was visually measured by a digitally overlaid protractor.

7.3.5 Optical microscopy and fluorescence data processing.

The fluorescence images were taken with a Nikon Eclipse LV150 microscope using the 10X objective. The microscope was equipped with a halogen-amp light source, a multicolor fluorescence cube (DAPI-FITC-TRITC), and a color CCD camera (DS-2M, Nikon, Inc.) controlled by NIS-Elements software. Fluorescence color (RGB) images with

16-bit color depth per channel were acquired by integrating a sequence of 16 8-bit color images. Fluorescence intensity of EBL created pillar arrays was analyzed by evaluating line profiles drawn across centers of the pillars in the acquired images. The most intense peaks identified in the fluorescence intensity profiles acquired in each of the three trials were used to calculate the mean and standard deviation. When evaluating the FITC and the Be (II) ion complexed version of the si-HBQ the values from the Green (G) channel was analyzed. When evaluating the uncomplexed si-HBQ substrate the Red (R) channel was analyzed. These values were collected from 10 × 10 pillar arrays across varying pillar diameters and extracted from the digital image with ImageJ software. All data have been background corrected by subtracting the intensity produced by a clean silicon surface. The same collection time and gain were used for both background and sample measurements. Subsequently data was normalized with respect to gain and collection time. The percent relative standard deviations (% RSD) values were determined by dividing the standard deviation by the mean peak intensity and multiplying by 100. The stochastic pillar arrays used herein for quantifying Be (II) via spotting were imaged as described above. The total fluorescence signal is derived using ImageJ software. The signal was integrated over a circular area with a diameter 100 nm greater than the largest spot (in this study we used 750 nm diameter). This is done by centering the area on each spot and integrating the intensity via ImageJ software. The value was normalized so that the highest concentration in the study was 1. The normalized values were plotted against the concentration and a logarithmic trend line and equation was derived by Microsoft Excel. Alternately, the normalized fluorescent yield was plotted against to log of the Be

(II) ion concentration creating a linear plot. Linear regression analysis was conducted with Microsoft Excel and the standard error, Significance F, Slope, were generated and used to calculate the LOD.

7.4 Results and discussion

7.4.1 The spectral characteristics of si-HBQ

The solution based excitation and emission of both Be (II) ion complexed and uncomplexed HBQ and its derivatives have been extensively studied,[8-10, 22] however the spectral characteristics of these surface immobilized versions have never been reported. We have used highly ordered EBL pillar arrays to investigate the fluorescent emission of both the Be (II) ion complexed and uncomplexed forms of si-HBQ using a common multipurpose fluorescence microscope, and digital-image analysis. The native median fluorescence of HBQ in ethanol arises from the excited state with intermolecular proton transfer occurring concurrently with fast interchange process between the keto-enol tautomers.[23] In the complexed structure the Be (II) ion replaces the hydroxyl proton, disturbing the four-level electron state proposed by Sytnik and Kasha,[23] and replacing it with a more common two level system for the blue-shifted chelated ligand emission. As with other substituted HBQ molecules[9] this is most probably the case for the si-HBQ. As shown in Figure 7.2a when excited between 400 and 418 nm the si-HBQ has a fluorescence emission in the red wavelengths analogous to the λ_{em} =575 nm, reported previously.[9] When the si-HBQ substrate is spotted with the Be (II) sample solution creating a si-HBQ-Be complex the emission shifts to a brightly fluorescence green. This result is analogous to results obtained in solution with a $\lambda_{em.}$= 478 nm, also

reported previously.[9] In addition to determining the spectra characteristics we used the EBL created si-HBQ pillar arrays to evaluate if the color specific and pillar diameter dependent enhancement of fluorescent signals is clearly demonstrated as in our previous work.[12,13] Figure 2b demonstrates a pillar based enhancement that is clearly diameter dependent, but not necessarily solely dependent on an increase in surface area. It has been clearly demonstrated that increased surface area alone can add to signal intensity.[24] Logic follows that the pillars with larger diameters have a larger surface area thus a potential for additional fluorescence material to be collected within the field of view. We found that the pillars with the greatest surface area do not exhibit the largest pillar based enhancement. While semiconductor structures with diameters of approximately 100 nm (Figure 2c) are generally too large for quantum confinement effects, such structures can function as dielectric waveguides that can exhibit optical resonances in the visible spectrum.[13, 25, 26]

.We have recently shown that resonances in silicon nanopillars can lead to enhanced fluorescence of the fluorophores on or near their surfaces.[12,13] As shown in Figure 2 & b, the optimal pillar diameter to enhance the green emission of the si-HBQ-Be complex over the red emission of the uncomplexed si-HBQ falls in the pillars with the smallest diameters with in our study. Following established FDTD simulations[13] and experimental trends[12] reported previously.

7.4.2 pH dependence for complexation

Reported previously,[9, 22] at pH levels of 12 and higher HBQ and its substituted compounds, complex with the Be (II) ion int a 1:1 ratio.

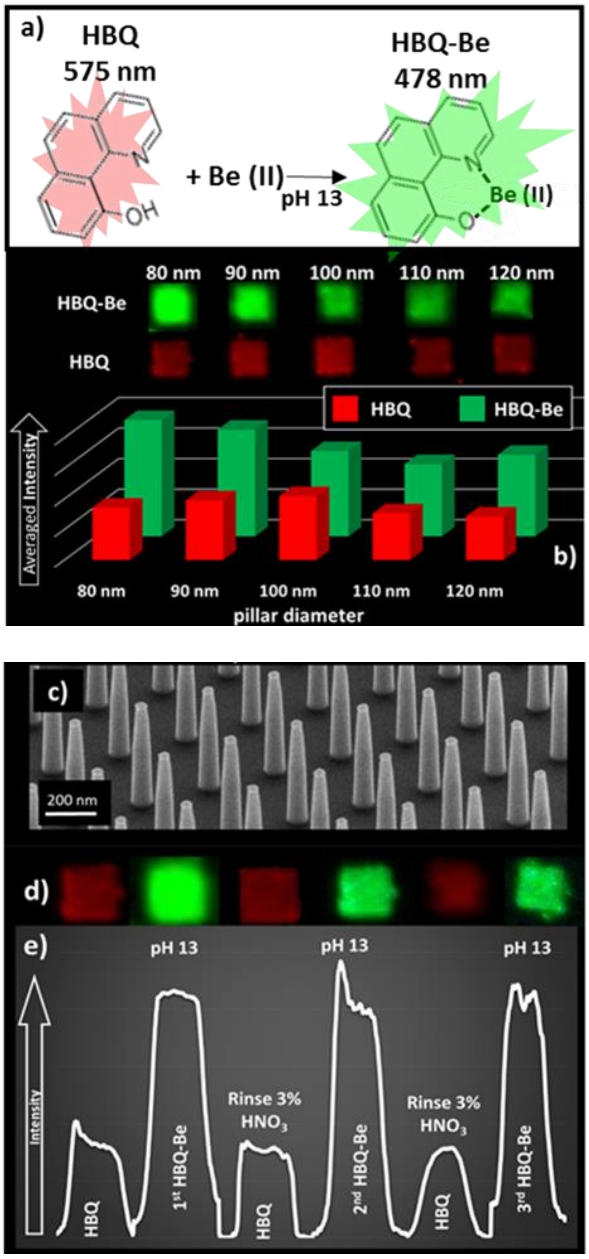

Figure 7.2. Evaluation of the si-HBQ substrate including, a) b)fluorescence images and averaged intensity across of 10 x 10 pillar arrays with varying pillar diameters of both si-HBQ unexposed (top) and exposed (bottom) to the Be(II) ion, c) SEM image of example 10 x 10 pillar array system fabricated with EBL lithography, d) fluorescence images and e) raw intensity profile of 10 x 10 pillar array showing pH dependency and reusability of si-HBQ system.

Under these conditions room temperature complexation is nearly instantaneous, and the complexed molecule and fluorescence intensity is stable over 24 hours. While these systems are stable at high pH, the acid dissociation constant of the preferred HL- molecule K_{a1} = ([H+][HL-])/[H_2L] is reported[9] to be $10^{-2.88}$, and the fluorescence of the Be (II) complexed ligand at pH 4 is not detectable over the background of the uncomplexed ligand.[9] As shown in Figure 2d & e, the adjustment from highly basic conditions to an acid rinse allows the stable complexed si-HBQ-Be to dissociate so that the Be (II) ion can be rinsed away. The ability to rinse the uncomplexed ion off of the platform while keeping positive control of the fluorescent si-HBQ ligand, allows the platform to be reused for additional Be (II) ion analyses. While we concede the exposure to changing conditions and handling damage to fragile high-aspect-ratio nanopillars arrays can cause degradation of the fluorescence emission signal, the system is robust enough for limited reuse.

Figure 2e shows very minimal signal degradation using the same substrate for three subsequent si-HBQ complexations with acidic rinses in between. Keeping positive control of the complexing ligand is a unique characteristic of si-HBQ substrate over solution-based HBQ and similar compounds that have been used for based fluorescence detection of Be (II) ions. Given the large number of potential samples required for monitoring, limiting reagent consumption by a factor of 3 or more turns into large potential reagent and waste savings.

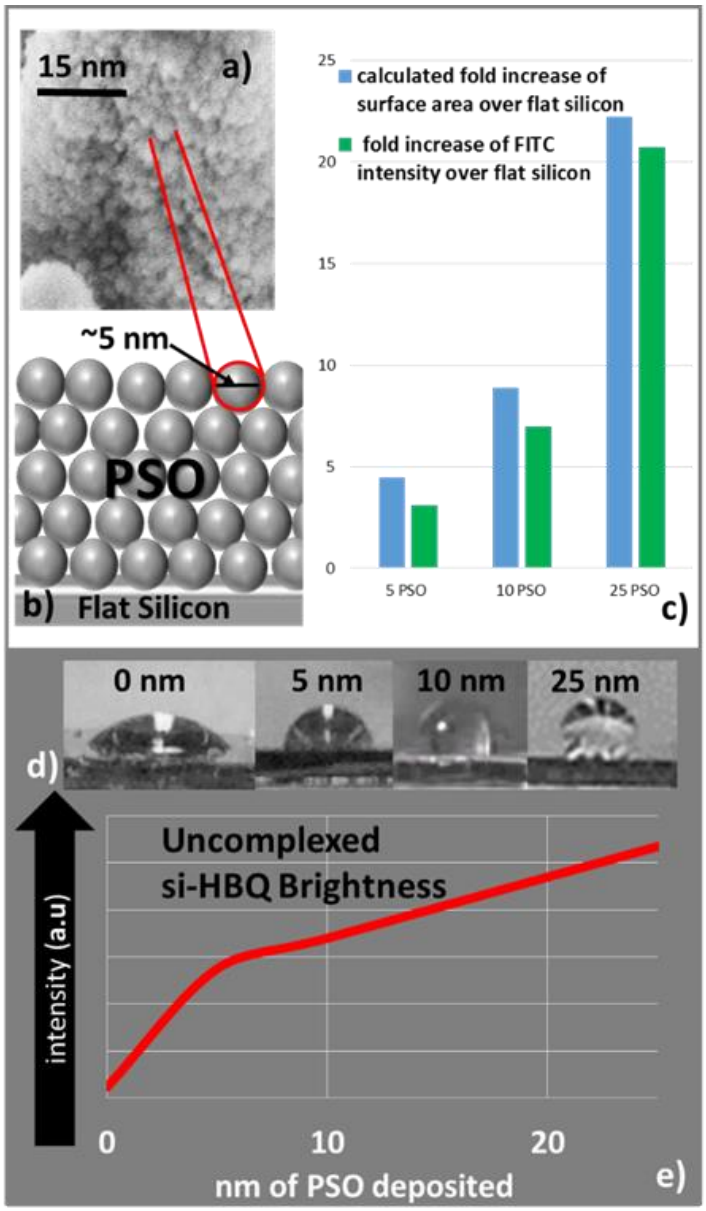

Figure 7.3. PSO evaluation including, a) SEM of PSO showing approximately 5 nm spherical formations, b) illustration of spherically approximated PSO on flat silicon surface in hexagonal close packed arrays used to approximate increase in surface area, c) results of the calculated fold increase in surface area and corresponding fold increase of FITC intensity on a flat silicon substrate deposited with 5, 10, and 25 nm PSO, d) hydrophobic nature of stochastic pillar arrays with 0, 5, 10, and 25 nm PSO layers and treated as shown in Figure 1 to create a si-HBQ system e) chart indicating the relative brightness of uncomplexed si-HBQ substrate, with 0, 5, 10, and 25 nm PSO layers.

7.4.3 *Creating a usable analytical platform*.

Using the precise control of pillar geometries afforded by the ELB fabrication described herein, would create a system whereby the enhancement of the complexed si-HBQ-Be could be evaluated and optimized. The EBL approach requires expensive equipment and is a slow serial process, creating practical limits as to the size and quantity of fabricated arrays.[14] Therefore, pillar arrays created via the EBL fabrication method as a platform is unfeasible due to the time and monetary demands of a high throughput analytical method. In order to meet these high demands we created a platform that may compromise some of the optimized enhancement for quickly fabricated vast pillar array substrates. While many methods of the bottom up approaches have the ability to quickly cover large areas creating etch masks suitable for subsequent fabrication of tightly spaced pillar arrays.[27, 28] We have recently fabricated and analyzed the morphology, wicking rates, hydrophobicity, fluorescence brightness and the selective transport of compounds associated with stochastic dewetted platinum pillar arrays.[14] Familiarity with the processing method as well as the ability to easily tune averaged pillar diameters based on Pt thickness drove us to choose stochastic dewetted pillar arrays as an analytical platform suitable for real life applications. In addition to dewetted silicon pillar arrays, PSO surface coatings were also investigated,[14] and it was shown that with increasing thicknesses of PSO the signal from a fluorescence dye increased, making a high brightness substrate. It was proposed previously,[14] that this increased brightness is a property of the increased surface area as well as the optical effects associated with silicon and silicon oxide.

An approximation of the increase in surface area associated with varying thickness of PSO was made with the assumption that PSO is made of individual spheres of approximately 5 nm in diameter (Figure 7.3a). The tight packing density of the layer is approximated to be close to that of perfect spheres arranged in a close pack array (Figure 3b) with the packing density of 0.7405.[29] We use this simplified model only for very thin layers of PSO

As described in the SI, associated with this manuscript, we calculated the increase in surface area associated with PSO over flat silicon. The results for 5, 10, and 25 nm layers of PSO are fold increases of 4.4, 8.9, and 22.2 respectively (Figure 7.3c). When the calculated results were compared against an increase in intensity of FITC found experimentally, the results were similar. We propose that the observed slight deviations were most likely from some of the approximated sphere surfaces being inaccessible to the dye. However, given these minimal deviations, we concluded the increased surface area associated with thin layers of PSO can be reasonably calculated using the proposed derivation. In addition to the increased binding sites afforded by the PSO, these layers provide the pillar arrays with a secondary level roughness that is traditionally associated with enhanced superhydrophobicity.[30]

The ability to create a hydrophobic surface is important in methods that include spotting as a method of sample introduction. The hydrophobic surface contains the sample within a spatially limited area essentially concentrating the sample on the system.[14, 16] In Figure 3d, the hydrophobicity of the si-HBQ system is shown to increase with the increase of PSO thickness. The minimum PSO thickness that truly displays a hydrophobic surface

with a contact angle grater that 90^0 is 10 nm. Finally, while increasing the surface binding sites is important one must remain cognizant of the added background associated with the uncomplexed si-HBQ. Figure 3e, shows that the intensity of the fluorescence due to the si-HBQ increases with the increased binding sites as expected, with a large increase in intensity associated with the addition of 5 nm over no PSO. This dramatic increase may be partially be attributed to the reflective properties of PSO in addition to the increased surface area. The slope of the change from 5 to 25 nm remains constant, indicating that increased fluorescence intensity of PSO on flat silicon follows surface area increase.

7.4.3 Evaluating the method

Given the results from the surface area increase, hydrophobicity experiments, combined with minimizing the uncomplexed background we chose an analytical platform comprised of stochastic pillar system that approximated the smaller diameter of the EBL pillar systems we evaluated, deposited with 10 nm of PSO, and treated as described in Figure 1 (shown in Figure 4b). The evaluation of the method included spotting of 0.10 µL of sample and allowing the spot to fully dry spot then evaluating the fluorescence within 2 to 3 hours. However samples reevaluated up to 48 hours after spotting had no noticeable degradation of the intensity. The low volume was used to assist in minimizing the spatial spread of the spot to confine each spot to an area amenable to imaging by a confocal fluorescence microscope with a 10x objective. Dried spots with increasing concentrations of 0.001, 0.01, 0.1, 1, and 10 µg/L (Figure 4b) were spotted on the same substrate and imaged subsequently without changing any setting on the imaging microscope.

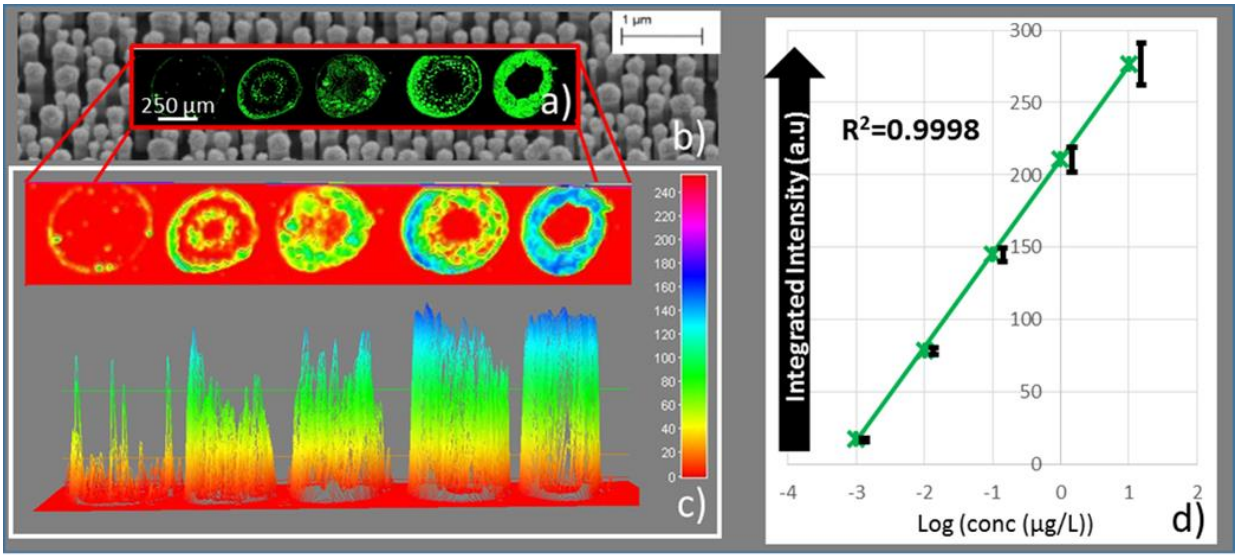

Figure 7.4. Quantitation of the Be(II) ion using the si-HBQ substrate including a) fluorescence images of dried spots of 0.1 µL of 0.001, 0.01, 0.1, 1, and 10 µg/L of Be(II) on si-HBQ substrate, b) SEM image of functionalized platform c) corresponding horizontal and vertical intensity map of dried spots d) plot displaying linear dependence of intensity to the log of the concentration of the Be(II) ion, with the standard deviation of each averaged point displayed to the right of the spot.

Upon first visual evaluation of the spots it was noted that the fluorescence was not congruent throughout the spot as it was in previous spotting work recently published within our group.[14, 31] However, given the high binding constant of HBQ with the Be (II) ion it is unlikely that a single Be (II) ion moves after it is bound to a si-HBQ ligand, and the speckled appearance of the spots is from the lack of Be (II) ion to fully fill the entire evaluated area. Calculations, based on the number of CTMS per square nm, [32] (fully described derivation in SI) show that the number of potential binding sites outnumber the number of Be (II) ions in a 10 µg/L spot by many orders of magnitude. Should the number of Be (II) ions outnumber the potential binding sites the unbound Be (II) could be rinsed form the analysis area or platform. To more fully understand the spatial intensity inside the spot an intensity heat map was generated (Figure 7.4c). The larger amount of high intensity compensates for the smaller density of signal over the area of the spot. Analogous to other surface immobilized type assays,[33] when the averaged integrated intensity of each spot is charted against the log of the concentration of the Be (II) ion a linear dependency can be drawn. After running regression analysis the coefficient of determination is very near 1 at R^2= 0.9998 and low significance F value, indicating that the experimental data fits closely to the linear statistical model and a meaningful correlation can be drawn between the integrated intensity and the concentration. Finally based on the residual standard deviation of the linear regression and slope of the regression line the LOD is 0.0006 µg/L. While the standard error based on the residuals for the model is quite small, looking at the standard deviation of the integrated values at each data point informative on the full range of the method. As the concentration

increases so does the raw standard deviation, however the % RSD is 5.4, 2.9, 3.3, 4.0, and 5.2 % for 0.001, 0.01, 0.1, 1, and 10 µg/L, respectively, are similar over the range, trending upward at the top and the bottom of the evaluated range.

7.4.4 Multiplexing the method

The large number of samples associated with the EPA and OSHA regulations make the analysis of the Be (II) ion prime for multiplexing. Herein capillaries are used for electroosmotic delivery of samples and have previously shown to be scalable up to a *96-capillary array.*[34, 35] *In a prototype system described previously,*[16] *approximately* 1 µL of a 0.1 *µg/L* Be (II) solution passed through the capillary system to form droplets at the end of the syringe needles. Subsequently these droplets were allowed to evaporate on si-HBQ surface. Three spots and a blank (figure 7.5) were then analyzed for integrated fluorescence intensity as previously described. The results associated with multiplexing the sample introduction added a small increase to the % RSD of a 0.1 µg/L sample, taking it from 3.3 to 5.2 %, and the associated signal: noise ratio was 50:1. In addition to these results, the prototype exhibited the ability to concentrate multiple samples in a small area, which could be scaled up and automated (as shown in Figure 7.5) such that a large number of samples could be concentrated onto the surface.

7.5 Conclusions

Herein, we have introduced a method for Be (II) ion detection that is ideal to use as a high throughput screening method. The novel platform created by immobilizing a previously developed HBQ fluorescent reagent on a silicon nanopillar system allows for fast analysis of many samples at high pg/L concentrations using sub-µL sample volumes.

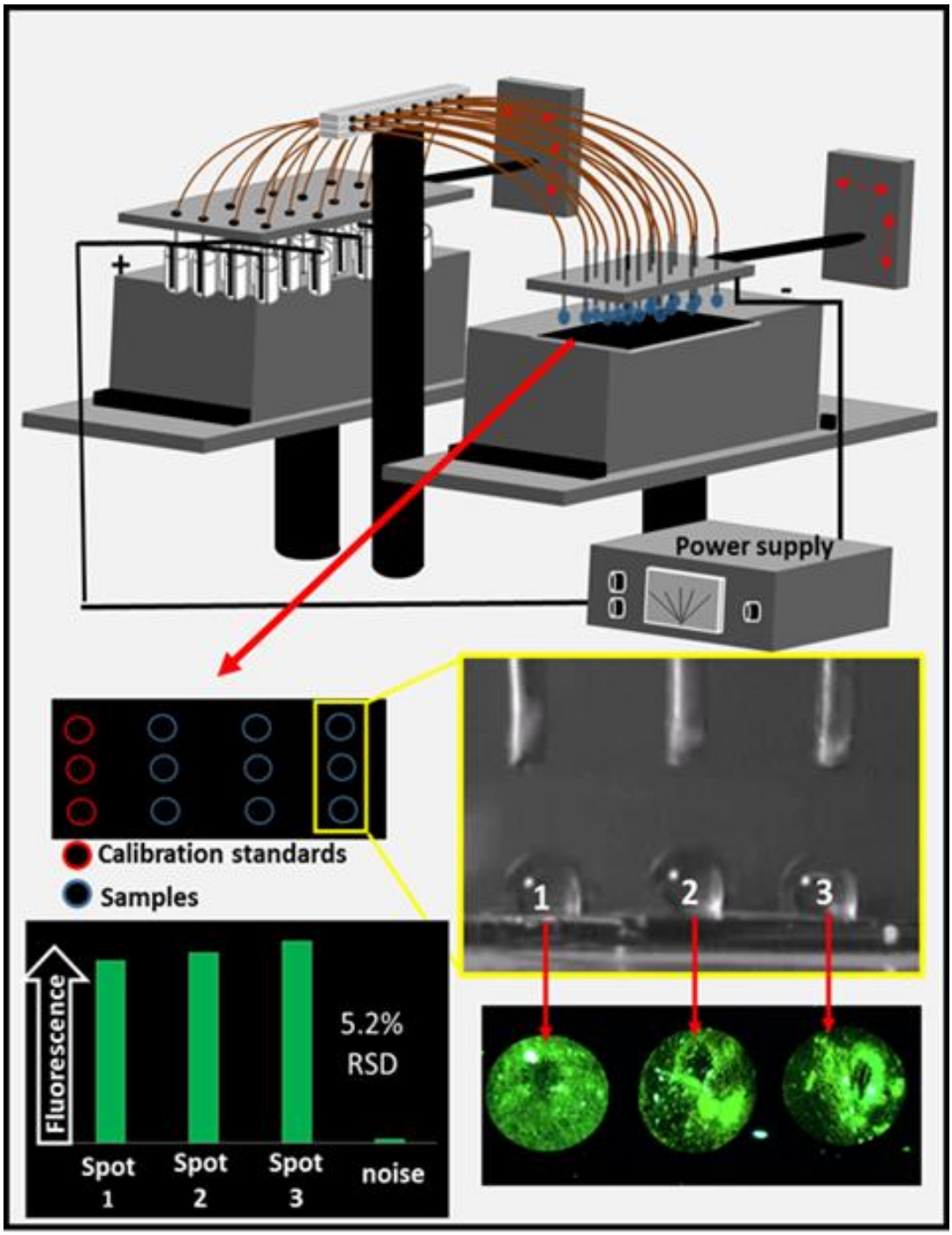

Figure 7.5. Multiplexing the method through capillaries used for electroosmotic delivery of sample with a low relative standard deviation and low background noise.

The minimal sample and reagent volumes, lack of complex and highly specific instrumentation, as well as positive control and reusability of traditionally consumable reagents creates a platform that is accessible and economically advantageous for industries where Be (II) ion detection and monitoring is required.

7.6 Author information

Corresponding author :

* Michael J. Sepaniak

Department of Chemistry

University of Tennessee

Knoxville, Tennessee 37996

Tel: 865-974-8023

Email: msepaniak@utk.edu

7.7 Acknowledgement

Substrate design, patterning and fabrication were conducted at the Center for Nanophase Materials Sciences, which is sponsored at Oak Ridge National Laboratory by the Scientific User Facilities Division, Office of Basic Energy Sciences, U.S. Department of Energy. This material is based on work supported in part by The National Science Foundation under Grant CHE-1144947 with the University of Tennessee. This work was supported in part by the Y-12 National Security Complex Plant Directed Research and Development fund.

7.8 Supporting information

Calculations referenced in text on surface area increase of thin layers of porous silicon oxide and the number of potential surface immobilized-, 10-hydroxybenzo[h]quinoline binding sites compared to quantity of Be (II) ion.

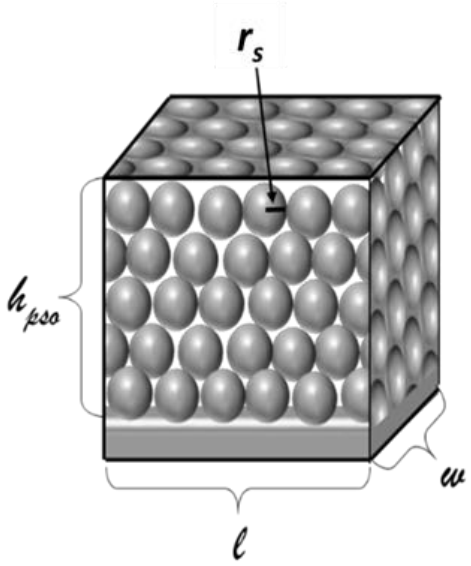

Figure 7.6. Hexagonal close pack array of spheres used to approximate PSO surface areas.

7.8.1 Calculated surface area increase of thin layers of porous silicon oxide (PSO)

The increase in surface area associated with thin layers of PSO is calculated as followed:

$$V_{PSO=}(l * w * h_{pso}) \qquad \textbf{Eq. 1}$$

where *l* is the length, *w* is the width, and h_{pso} is the thickness of the deposited PSO layer. Since the PSO layer is not solid the volume physically occupied by PSO Spheres is calculated by:

$$V_{Spheres=}V_{PSO} * Packing\ density \qquad \textbf{Eq. 2}$$

$V_{Spheres}$, is the volume occupied by the PSO spheres. The tight packing density of the layer is approximated to be close to that of perfect spheres arranged in a close pack array packing density (Figure 7.6) with a packing density of 0.7405.[36] The number of spheres (N_{Sheres}) was determined by dividing the total occupied volume by the volume for a single sphere:

$$N_{Spheres} = \frac{V_{Spheres}}{\left(\frac{4}{3}\right) * \pi * {r_s}^3} \qquad \textbf{Eq. 3}$$

where r_s is the radius of a single sphere by visual estimate is 2.5 nm. For the final calculation to determine surface area the area of a single sphere is found by:

$$A_{ssphere} = 4 * \pi * {r_s}^2 \qquad \textbf{Eq. 4}$$

where $A_{ssphere}$ is the surface area associated to a single PSO sphere. The final steps include finding the surface area associated with the entire layer of PSO, finding the substrate area, and comparing the two, as followed:

$$A_{spheres} = A_{ssphere} * N_{Spheres} \qquad \textbf{Eq. 5}$$

$$A_{substrate} = l * w \qquad \textbf{Eq. 6}$$

$$increased\ area = \frac{A_{spheres}}{A_{substrate}} \qquad \textbf{Eq. 7}$$

Where $A_{spheres}$ is the entire surface area of PSO layer, $A_{substrate}$ is the surface of the flat silicon.

7.8.2 Number of potential surface immobilized-, 10-hydroxybenzo[h]quinoline (si-HBQ) binding sites compared to quantity of Be (II) ion

Due to the nanoscale morphology of the substrate and the associated concern with overloading of the pillar array substrate we calculated the Number of Be (II) ions compared to potentially available binding sites.

Using the highest concentration we evaluated in this study a 0.1 µL drop with 10 µg/L has approximately 70 billion Be (II) ions are present. We calculated the number of potential binding sites for the area of the spotted sample using the average radius of the experimental spots (250 micron), the average pitch (~200 nm presented previously[14]), height (~1200 nm), and diameter (~100 nm) of the pillars in the arrays, the added surface area afforded by the PSO (8.9 fold increase) presented in this work, the area per chloropropyltrimethoxysilane CTMS (2.7 nm^2, presented previously[32]) approximated by an amino terminated molecules with similar conformation and calculate as followed:

$$area\ of\ spot = \pi * r^2 \qquad \textbf{Eq. 8}$$

$$area\ per\ pillar = \pi * (\frac{Pitch}{2})^2 \qquad \textbf{Eq. 9}$$

$$number\ of\ pillars = (area\ of\ spot)/(area\ of\ pillar) \qquad \textbf{Eq. 10}$$

$$total\ functionalized\ area = \qquad \textbf{Eq. 11}$$

$$PSO\ increase\ (area\ of\ spot + (number\ of\ pillars\ \left(2 * \pi * \left(\frac{diameter}{2}\right) * height\right))$$

$$number\ of\ chloroterminated\ binding\ sites = \frac{(total\ functionalized\ area)}{(area\ per\ CTMS)} \qquad \textbf{Eq. 12}$$

We assume that an HBQ does not bind to each chloro-terminated binding site and we use an approximation that one HBQ will bind to the surface out of each one hundred potential HBQ binding sites. Using this modest approximation the number of calculated si-HBQ sites is $3.4 * 10^{13}$, several orders of magnitude higher than the $6.9 * 10^{10}$ Be (II) ions in the highest concentration spot.

7.9 References

[1] Wambach, P.F. and J.C. Laul, *Beryllium health effects, exposure limits and regulatory requirements.* Journal of Chemical Health and Safety, 2008. **15**(4): p. 5-12.

[2] Kolanz, M.E., *Introduction to beryllium: uses, regulatory history, and disease.* Applied occupational and environmental hygiene, 2001. **16**(5): p. 559-567.

[3] ATSDR, I., *Toxicological profile for beryllium.* Atlanta, Agency for Toxic Substances and Disease Registry, 2002.

[4] Brisson, M.J., et al., *Trace-level beryllium analysis in the laboratory and in the field: state of the art, challenges and opportunities.* Journal of Environmental Monitoring, 2006. **8**(6): p. 605-611.

[5] Robert M. Bruce, L.I., Annie Jarabek, *TOXICOLOGICAL REVIEW OF BERYLLIUM AND COMPOUNDS (CAS No.7440-41-7)* U.S.E.P. Agency, Editor. 1998: Washington, DC.

[6] Sanderson, W.T., et al., *Lung cancer case-control study of beryllium workers.* American journal of industrial medicine, 2001. **39**(2): p. 133-144.

[7] Schuler, C.R., et al., *Process-related risk of beryllium sensitization and disease in a copper–beryllium alloy facility.* American journal of industrial medicine, 2005. **47**(3): p. 195-205.

[8] Matsumiya, H. and H. Hoshino, *Selective determination of beryllium (II) ion at picomole per decimeter cubed levels by kinetic differentiation mode reversed-phase high-performance liquid chromatography with fluorometric detection using 2-(2'-hydroxyphenyl)-10-hydroxybenzo [h] quinoline as precolumn chelating reagent.* Analytical chemistry, 2003. **75**(3): p. 413-419.

[9] Matsumiya, H., H. Hoshino, and T. Yotsuyanagi, *A novel fluorescence reagent, 10-hydroxybenzo [h] quinoline-7-sulfonate, for selective determination of beryllium (II) ion at pg cm− 3 levels.* Analyst, 2001. **126**(11): p. 2082-2086.

[10] Minogue, E.M., et al., *Development of a new fluorescence method for the detection of beryllium on surfaces.* J. ASTM Int, 2005. **2**(9): p. 10.

[11] Eller, P.M. and M.E. Cassinelli, *NIOSH manual of analytical methods*. Vol. 94. 1994: DIANE Publishing.

[12] Kandziolka, M., et al., *Silicon Nanopillars As a Platform for Enhanced Fluorescence Analysis.* Analytical Chemistry, 2013. **85**(19): p. 9031-9038.

[13] Wells, S.M., et al., *Silicon Nanopillars for Field-Enhanced Surface Spectroscopy.* ACS Nano, 2012. **6**(4): p. 2948-2959.

[14] Charlton, J.J., et al., *Wicking Nanopillar Arrays with Dual Roughness for Selective Transport and Fluorescence Measurements.* ACS Applied Materials & Interfaces, 2014. **6**(20): p. 17894-17901.

[15] Rebecca, L.A., et al., *Lithography-free approach to highly efficient, scalable SERS substrates based on disordered clusters of disc-on-pillar structures.* Nanotechnology, 2013. **24**(50): p. 505302.

[16] Wallace, R.A., et al., *Superhydrophobic Analyte Concentration Utilizing Colloid-Pillar Array SERS Substrates.* Analytical Chemistry, 2014. **86**(23): p. 11819-11825.

[17] Walker, B.N., et al., *Tailored Silicon Nanopost Arrays for Resonant Nanophotonic Ion Production.* The Journal of Physical Chemistry C, 2010. **114**(11): p. 4835-4840.

[18] Ceiler, M., P. Kohl, and S. Bidstrup, *Plasma-Enhanced Chemical Vapor Deposition of Silicon Dioxide Deposited at Low Temperatures.* Journal of the Electrochemical Society, 1995. **142**(6): p. 2067-2071.

[19] Borrás, A., A. Barranco, and A.R. González-Elipe, *Design and control of porosity in oxide thin films grown by PECVD.* Journal of Materials Science, 2006. **41**(16): p. 5220-5226.

[20] Sato, M., et al., *Effect of oxide thickness on the degradation of organic silane monolayers on silicon wafer surface during XPS measurement.* Surface and interface analysis, 2006. **38**(4): p. 838-841.

[21] Howarter, J.A. and J.P. Youngblood, *Optimization of Silica Silanization by 3-Aminopropyltriethoxysilane.* Langmuir, 2006. **22**(26): p. 11142-11147.

[22] Zheng, Y., et al., *Analysis of beryllium to biomolecule binding using a metal specific fluorescent probe and competitive assay.* Talanta, 2011. **85**(1): p. 638-643.

[23] Sytnik, A. and M. Kasha, *Excited-state intramolecular proton transfer as a fluorescence probe for protein binding-site static polarity.* Proceedings of the National Academy of Sciences, 1994. **91**(18): p. 8627-8630.

[24] Suzuki, Y. and K. Yokoyama, *Construction of a more sensitive fluorescence sensing material for the detection of vascular endothelial growth factor, a biomarker for angiogenesis, prepared by combining a fluorescent peptide and a nanopillar substrate.* Biosensors and Bioelectronics, 2011. **26**(8): p. 3696-3699.

[25] Cao, L., et al., *Tuning the Color of Silicon Nanostructures.* Nano Letters, 2010. **10**(7): p. 2649-2654.

[26] Cao, L., et al., *Engineering light absorption in semiconductor nanowire devices.* Nat Mater, 2009. **8**(8): p. 643-647.

[27] Huang, Z., H. Fang, and J. Zhu, *Fabrication of Silicon Nanowire Arrays with Controlled Diameter, Length, and Density.* Advanced Materials, 2007. **19**(5): p. 744-748.

[28] Hsu, C.-M., et al., *Wafer-scale silicon nanopillars and nanocones by Langmuir–Blodgett assembly and etching.* Applied Physics Letters, 2008. **93**(13): p. -.

[29] Sanders, J.V., *Close-packed structures of spheres of two different sizes I. Observations on natural opal.* Philosophical Magazine A, 1980. **42**(6): p. 705-720.

[30] Callies, M., et al., *Microfabricated textured surfaces for super-hydrophobicity investigations.* Microelectronic Engineering, 2005. **78–79**(0): p. 100-105.

[31] Kirchner, T.B., et al., *Highly Ordered Silicon Pillar Arrays As Platforms for Planar Chromatography.* Analytical Chemistry, 2013. **85**(24): p. 11802-11808.

[32] Jung, H.-S., D.-S. Moon, and J.-K. Lee, *Quantitative Analysis and Efficient Surface Modification of Silica Nanoparticles.* Journal of Nanomaterials, 2012. **2012**: p. 8.

[33] Pierangeli, S.S. and E.N. Harris, *A protocol for determination of anticardiolipin antibodies by ELISA.* Nat. Protocols, 2008. **3**(5): p. 840-848.

[34] Tan, H. and E.S. Yeung, *Automation and Integration of Multiplexed On-Line Sample Preparation with Capillary Electrophoresis for High-Throughput DNA Sequencing.* Analytical Chemistry, 1998. **70**(19): p. 4044-4053.

[35] Gao, Q. and E.S. Yeung, *High-Throughput Detection of Unknown Mutations by Using Multiplexed Capillary Electrophoresis with Poly(vinylpyrrolidone) Solution.* Analytical Chemistry, 2000. **72**(11): p. 2499-2506.

[36] Sanders, J.V., *Close-packed structures of spheres of two different sizes I. Observations on natural opal.* Philosophical Magazine A, 1980. **42**(6): p. 705-720.

CHAPTER 8:
CONCLUSION

8.1 Concluding remarks

As stated previously throughout this work, the analysis of a vast number of samples in a limited time frame is often paramount for human health and safely as well as environmental monitoring. This need for the rapid analysis of a massive number of samples fast drives the development of novel high throughput methods and platforms for the analysis of vastly differing materials. While the materials have differing chemical and spectral identities the methodology used to increase throughput is often the same. And three broad areas of research in the field of increased throughput can be summed up as:[1] 1) methods and detection 2) sample handling and robotics 3) Process flow and information management. In this work we aim to address parts of all three of these categories.

The first area of research we use customized robotics to combine SPE with ICP-MS to deliver a viable, robust, automated method for actinide pre-concentration, detection and analysis technique tailored to use when rapid high-throughput sample processing is essential. The merits of the methods include high recovery, minimized sample preparation and dilution, direct loading on the SPE platform, a one-step elution process, high-throughput with decreased technician dependence, and concurrent analysis of the major actinides while maintaining an accessible platform.

Secondly we worked to develop an expansive platform of stochastic nanoscale pillar arrays with a straightforward processing method. The method includes Pt dewetting, dry etching, and PECVD of PSO and was developed to create nanopillar arrays with relative ease, cost considerations, and environmental soundness. Advantages of the implemented arrays include easily tunable inter- and intra-wafer average pillar diameters,

dual level tunable roughness, rapid solvent wicking, super-hydrophobicity, chemically selective transport, as well as the ability to promote high florescence brightness. These features, make the fabricated nanopillar arrays, especially attractive for analytical methods and offer a pathway for the large scale production of substrates for use in separations of select compounds with florescence signal detection.

Finally we use previously explored nanopillar based field enhancements and their effects of the intensity of the fluorescence of selected compounds. First we successfully demonstrated fluorescence bioassays using a newly developed on-chip platform based on silicon nanopillars which provide nanoscale focusing and resonance enhancement of the probing optical fields. Results obtained using various biological fluorescent systems indicate that enhancement of fluorescence signals associated with silicon nanopillars significantly exceed a surface area increase. We believe the demonstrated platform will be a valuable addition to the series of the previously developed systems for fluorescence analysis, such as LSPR based systems and ZMW. Compared to other concepts and designs that already found applications in fluorescence analysis, the most distinctive features of the system based on silicon nanopillars include their straightforward spectral tunability and pronounced out-of plane geometry. The latter can be particularly useful in designing methods that combine multiple, for instance, optical and electrochemical,[2] modes of analytical interrogation of biological samples and cells. Results of our feasibility experiments reported here complement these unique aspects of the demonstrated approaches with a series of quantitative figures of merit that include detectability of fewer than 10 protein molecules, lateral resolution down to the diffraction limit, and

enhancement of fluorescence in excess of 10^3. Secondly we introduced a method for Be (II) ion detection that is ideal to use as a high throughput screening method. The novel platform created by immobilizing a previously developed HBQ fluorescent reagent on a silicon nanopillar system allows for fast analysis of many samples at high pg/L concentrations using sub-µL sample volumes. The minimal sample and reagent volumes, lack of complex and highly specific instrumentation, as well as positive control and reusability of traditionally consumable reagents creates a platform that is accessible and economically advantageous for industries where Be (II) ion detection and monitoring is required.

The methods and platforms developed in this work range from advancing a well know separation through robotics to creating an entirely new platform for analysis. Both work to expand the knowledge and capacity of high-throughput analytical chemical analysis.

8.2 References

[1] Hertzberg, R.P. and A.J. Pope, *High-throughput screening: new technology for the 21st century.* Current opinion in chemical biology, 2000. **4**(4): p. 445-451.

[2] Anger, P.; Bharadwaj, P.; Novotny, L. Phys. Rev. Lett. 2006, 96, 113002

VITA

Jennifer Charlton was born in Orange, C A. In July of 1976. She was raised in Jacksonville, Fl. where her interest in pursuing science as a career originated at Stanton College Preparatory School. She completed her Associates of Arts at Florida State College in Jacksonville followed by her Bachelors of Science in Chemistry at the University of North Florida. As part of her Bachelor's work she conducted research as part of the sensors group on the development and optimization of the multivariate analysis of phosphate and arsenate via vanadomolybdate reagent, under Stuart Chalk. She pursued her Doctorate of Philosophy in Analytical Chemistry at The University of Tennessee in Knoxville (UTK), under Michael J. Sepaniak. During her time at The University of Tennessee in Knoxville she was been fully funded by Y-12 National Security Complex through DOE, NNSA, and Y-12 PDRD. Her work focused on the development of novel detection platforms and instrumentation with high sensitivity and specificity of materials associated with the production and maintenance of transuranic metals. One of her achievements include winning the Judson Hall Robertson Fellowship for achievements in analytical chemistry from the University of Tennessee. Her collaborations include Y-12 Analytical Chemistry Organization Technical Development, Oak Ridge National Lab the Center for Nanophase Material Science, The University of Texas in Austin, The University of North Arizona, as well as Oak Ridge High School and the L&M STEM School in Knoxville, Tennessee. She will graduate in the summer of 2015, with the hopes of a staff scientist at a DOE/DOD site continuing work in instrumentation and platform development.